

Important Notice

This copy may be used only for the purposes of research and private study, and any use of the copy for a purpose other than research or private study may require the authorization of the copyright owner of the work in question. Responsibility regarding questions of copyright that may arise in the use of this copy is assumed by the recipient.

UNIVERSITY OF CALGARY

Designing Explicit Wavefield Extrapolators
For Depth Migration and Migration Velocity Analysis

by

Saleh M. Al-Saleh

A THESIS

SUBMITTED TO THE FACULTY OF GRADUATE STUDIES
IN PARTIAL FULFILMENT OF THE REQUIREMENTS FOR THE
DEGREE OF
DOCTOR OF PHILOSOPHY

Department of Geology and Geophysics

CALGARY, ALBERTA

August, 2006

© Saleh M. Al-Saleh 2006

UNIVERSITY OF CALGARY
FACULTY OF GRADUATE STUDIES

The undersigned certify that they have read, and recommend to the Faculty of Graduate Studies for acceptance, a thesis entitled "Designing Explicit Wavefield Extrapolators For Depth Migration and Migration Velocity Analysis" submitted by Saleh M. Al-Saleh in partial fulfilment of the requirements of the degree of Doctor of Philosophy.

Supervisor, Dr. Gary F. Margrave
Department of Geology and Geophysics

Co-Supervisor, Dr. John C. Bancroft
Department of Geology and Geophysics

Dr. Don C. Lawton
Department of Geology and Geophysics

Dr. Larry R. Lines
Department of Geology and Geophysics

Dr. David W. Hobill
Department of Physics

Dr. Peter W. Cary
Sensor Geophysical Ltd

Date

Abstract

Recursive explicit wavefield extrapolation methods are a powerful tool for imaging complex geological subsurface structures. These methods, however, have three major problems: (1) they require short, stable operators to be computationally efficient, (2) they assume that extrapolation proceeds from a flat surface, and (3) they are very sensitive to velocity models. In this thesis, some improvements to existing methods are proposed, and new algorithms are developed where appropriate.

A new technique for designing practically stable wavefield extrapolators is shown. This approach is then used to optimize the forward operator and conjugate inverse (FOCI) algorithm. Downward-continuation can be efficiently implemented directly from topography by building wavefield extrapolators that can handle lateral velocity and topography variations.

Three domains for migration velocity analysis (MVA) are derived in the same context and reformulated as mathematical hypotheses. Different aspects of these domains are combined into a unified domain that offers more prestack information than the three individual domains.

Acknowledgements

I would like to extend my gratitude to my supervisor, Dr. Gary F. Margrave, for his patient guidance and generous help throughout my entire PhD study. Dr. Margrave, with his vast knowledge of seismic imaging, has shown me how to use mathematics as a tool to express geophysical concepts more clearly and precisely. He also helped to communicate effectively with other disciplines such as mathematics and physics. I also thank my co-supervisor, Dr. John C. Bancroft, for his beneficial comments and help throughout my PhD study. I am also thankful to Dr. Hugh D. Geiger for many useful discussions, comments, and providing the Marmousi dataset. Special thanks go my mentor at Saudi Aramco, Dr. Panos Kelamis, for his help throughout my study. In addition, I would like to thank Dr. Lou Fishman, Dr. Ed Krebes, Dr. Rob Stewart, Dr. Larry Lines, Dr. Don Lawton, and Dr. Fred Cook for teaching beneficial courses that helped me throughout my study. I also would like to thank Dr. Rolf Maier for proofreading this thesis. Special thanks go to Kevin Hall, Dr. Chuck Ursenbach, Abdullah Al-Shuhail, Chad Hogan, Faranak Mahmoudian, Dave Henley, Henry Bland, Dr. Helen Isaac, and Louise Forgues for their help. Special thanks go to Dr. Peter Cary and Dr. David W. Hobill for accepting to be in my committee. Also, I would like to thank the staff, students and sponsors of CREWES and POTSI projects. I am also grateful to Saudi Aramco for sponsoring my study.

Finally, I would like to sincerely thank my parents and my wife for their patience, support, and encouragement.

Dedication

This work is dedicated to my parents, wife, and kids

Table of Contents

Approval Page.....	ii
Abstract.....	iii
Acknowledgements.....	iv
Dedication.....	v
Table of Contents.....	vi
List of Figures.....	x
Glossary of terms.....	xvi
List of symbols.....	xxiii
CHAPTER 1: INTRODUCTION.....	1
1-1 THE SEISMIC EXPERIMENT.....	1
1-2 THE KIRCHHOFF METHODS.....	3
1-3 DOWNWARD-CONTINUATION METHODS.....	6
1-4 WHY EXPLICIT WAVEFIELD EXTRAPOLATION?.....	7
1-5 CHALLENGES FOR EXPLICIT WAVEFIELD EXTRAPOLATION METHODS.....	9
1-7 CURRENT SOLUTIONS TO CHALLENGES FACING WAVEFIELD EXTRAPOLATION METHODS.....	10
1-8 THESIS MAIN CONTRIBUTIONS.....	12
1-9 STRUCTURE OF THE THESIS.....	12
CHAPTER 2: THEORY OF EXPLICIT WAVEFIELD EXTRAPOLATION METHODS.....	15
2-1 THE PHASE-SHIFT EXTRAPOLATION.....	16
2-2 SHOT PROFILE MIGRATION.....	22
2-3 THE PHASE-SHIFT PLUS INTERPOLATION (PSPI) AND THE GENERALIZED PHASE-SHIFT PLUS INTERPOLATION (GPSPI) ALGORITHMS.....	28
2-4 SPACE-FREQUENCY DOMAIN WAVEFIELD EXTRAPOLATION.....	31
2-5 THE STABILITY PROBLEM OF EXPLICIT WAVEFIELD EXTRAPOLATORS.....	32
2-5.1 Numerical instability.....	32

2-5.2 Inherent instability	39
2-6 CHAPTER SUMMARY	39
CHAPTER 3: COMPARISONS OF THE HALE, SOUBARAS, WLSQ, AND FOCI WAVEFIELD EXTRAPOLATORS	
3-1 HALE'S EXTRAPOLATOR	41
3-1.1 Stabilizing Hale's extrapolator	44
3-2 THEORY OF THE SOUBARAS EXTRAPOLATOR	47
3-3 THE WLSQ EXTRAPOLATOR	51
3-4 THE FOCI EXTRAPOLATOR	56
3-4.1 Dual operator tables for increased instability	58
3-4.2 Spatial resampling	61
3-5 A COMPARISON OF THE VARIOUS EXTRAPOLATORS	67
3-5.1 Amplitude and phase spectra	67
3-5.2 Impulse responses of the Hale, Soubaras, WLSQ and FOCI extrapolators	71
3-5.3 Prestack depth migration with the various extrapolators	74
3-6 CHAPTER SUMMARY	75
CHAPTER 4: USING A TRANSITION BAND IN THE WEIGHTED LEAST- SQUARES DESIGN OF WAVEFIELD EXTRAPOLATORS AND FOCI ENHANCEMENT	
4-1 LEAST-SQUARES-BASED METHODS FOR DESIGNING WAVEFIELD EXTRAPOLATORS	79
4-1.1 Unweighted least-squares	81
4-1.2 Weighted least-squares using a transition function	81
4-1.3 Weighted least-squares using a transition band	82
4-2 A COMPARISON BETWEEN THE WLSQ AND WLSTB EXTRAPOLATORS	85
4-2.1 Impulse response results using the WLSQ and WLSTB extrapolators	87
4-2.2 Prestack depth migration results using the WLSQ and WLSTB extrapolators	89
4-3 USING THE WLSTB APPROACH TO ENHANCE THE FOCI ALGORITHM	89
4-3.1 Amplitude and phase spectra comparisons	92
4-3.2 Impulse response examples	97
4-3.3 Images of the Marmousi dataset using the FOCI and the optimized FOCI algorithms	100
4-4 CHAPTER SUMMARY	107

CHAPTER 5: EXPLICIT WAVEFIELD EXTRAPOLATION FROM TOPOGRAPHY.....	108
5-1 THE ZERO-VELOCITY LAYER APPROACH.....	109
5-1.1 Defining the geometry.....	109
5-1.2 Time-shifting the data to a flat datum.....	110
5-1.3 Special extrapolation between the topography and datum.....	111
5-1.4 Application of the zero-velocity approach using the Aruma dataset.....	114
5-2 SOURCE-RECEIVER MIGRATION FROM TOPOGRAPHY WITH A LATERALLY VARIABLE DEPTH STEP.....	122
5-3 SHOT PROFILE MIGRATION FROM TOPOGRAPHY WITH A VARIABLE DEPTH STEP.....	127
5-4 CHAPTER SUMMARY.....	131
CHAPTER 6: REFORMULATING THE RCA, DFA, AND CFP MVA DOMAINS INTO MATHEMATICAL HYPOTHESES.....	132
6-1 RCA APPROACH.....	133
6-1.1 The process of generating the common image gathers.....	134
6-2.2 The RCA hypothesis.....	136
6-2 DFA APPROACH.....	139
6-2.1 The DFA imaging hypothesis.....	139
6-2.2 The process of creating a depth focusing panel.....	141
6-3 CFP APPROACH.....	145
6-4 CHAPTER SUMMARY.....	152
CHAPTER 7: THE COMMON IMAGE CUBE ANALYSIS (CICA) FOR MIGRATION VELOCITY ANALYSIS.....	154
7-1 THE COMMON IMAGE CUBE ANALYSIS APPROACH (CICA).....	154
7-1.1 The CICA imaging hypothesis.....	155
7-1.2 The CICA imaging hypothesis in words.....	156
7-1.3 The RCA, DFA, CFP, and CICA approaches.....	157
7-2 CONSTANT VELOCITY EXAMPLES.....	158
7-3 INVERSION AND VELOCITY MODEL UPDATING.....	164
7-4 CHAPTER SUMMARY.....	166
CHAPTER 8: DISCUSSION AND CONCLUSIONS.....	167

8-1 EXPLICIT WAVEFIELD EXTRAPOLATION METHODS	167
8-2 HALE, SOUBARAS, WLSQ, AND FOCI WAVEFIELD EXTRAPOLATORS....	168
8-3 THE WLSTB APPROACH AND THE OPTIMIZED FOCI ALGORITHM	169
8-4 DOWNWARD-CONTINUATION FROM TOPOGRAPHY.....	171
8-5 THE RCA, DFA, AND CFP DOMAINS FOR MVA.....	171
8-6 THE CICA APPROACH.....	172
APPENDIX A: THE FOURIER TRANSFORM OF THE WAVEFIELD EXTRAPOLATOR.....	174
APPENDIX B: REAL AND IMAGINARY PARTS OF THE WAVEFIELD EXTRAPOLATOR.....	176
APPENDIX C: SOUBARAS'S EXTRAPOLATOR	178
REFERENCES	181

List of Figures

Figure 1-1. Schematic for a common shot gather for a flat reflector.....	2
Figure 1-2. A schematic diagram showing how migration transforms the recorded data from the data space to the image space, where x and y are the transverse coordinates, M is a transformation operator or mapping operator, \mathbb{R}^5 and \mathbb{R}^3 refer to real numbers in 3 and 5 dimensions, respectively.....	3
Figure 1-3. Comparison of downward-continuation migration versus Kirchhoff migration (Ren et al., 2005). Note the improved imaging of steeply-dipping events, leading to more details being visible in the depth slice of the migrated volume obtained using downward-continuation migration (the circles show some comparison areas).	5
Figure 1-4 Nonstationary convolution when the velocity varies laterally. The different grey levels refer to operators calculated with different velocities.	8
Figure 1-5 Stationary convolution where the wavefield at each output point is computed using the same operator.....	8
Figure 2-1. The (a) amplitude and (b) phase spectra of the exact spectrum, where $\Delta x=10$ m, $\Delta z=10$ m, $f=50$ Hz, and $V=2000$ m/s. The dashed lines indicate the evanescent boundaries.	33
Figure 2-2. The (a) amplitude and (b) phase of the exact spectrum for $f=0-80$ Hz, where $\Delta x=10$ m, $\Delta z=10$ m, and $V=2000$ m/s.	35
Figure 2-3. The (a) amplitude of a 31-point operator in the space-frequency domain obtained using a boxcar window, (b) amplitude of the actual spectrum, and (c) phase of the actual spectrum using the same parameters as Figure 2-1.....	36
Figure 2-4. The (a) amplitude of the actual spectrum of a 31-point operator obtained by windowing the ideal operator with a Hanning window using the same parameters as Figure 2-1, and (b) the amplitude is raised to a power of 50 or $\left \hat{W} \right ^{50}$. The dashed lines indicate the evanescent boundaries. Note that amplitude is less than unity for most propagation angles.	38
Figure 3-1. Amplitudes of the exact and actual spectra using $\omega \Delta x / V = \pi / 2$, $\Delta x = \Delta z = 10$ m, and $N = 31$. The dashed lines define the evanescent boundaries. .	45

Figure 3-2. Amplitudes of the actual spectrum for different frequencies with a constant $\mathbf{M}=5$. The frequency range is 10-100 Hz in increments of 10 Hz, $V=2000$ m/s, $\Delta x=10$ m, $\Delta z=10$ m, and $N=19$	46
Figure 3-3. Amplitudes of the actual spectrum for different frequencies after varying the value of \mathbf{M} . The frequency range is 10-100 Hz in increments of 10 Hz, $V=2000$ m/s, $\Delta x=10$ m, $\Delta z=10$ m, the range of \mathbf{M} is 1-8, and $N=19$	46
Figure 3-4. Comparisons of the exact and actual spectra, where (a) shows the real parts of the spectra, (b) shows the imaginary parts of the spectra, and (c) shows the amplitudes of the spectra, using $\alpha = 75^\circ$, $\Delta x=10$, $\Delta z=10$ m, and $N=31$	50
Figure 3-5. (a) Amplitudes and (b) phases of the exact and desired spectra, where $\alpha = 75^\circ$, $\Delta x=10$, $\Delta z=10$ m, $f=50$ Hz, and $\varepsilon=0.0001$	54
Figure 3-6. (a) Amplitudes and (b) phases of the exact spectrum and actual spectrum of WLSQ, where $N=31$, $\alpha = 75^\circ$, $\Delta x=10$, $\Delta z=10$ m, $f=50$ Hz, and $\varepsilon=0.0001$	55
Figure 3-7. The (a) amplitudes and (b) phases of the exact and FOCI spectra, where $\eta=1$, $n_{for}=21$, $n_{inv}=31$, and $f=40$ Hz.	59
Figure 3-8. The (a) amplitudes and (b) phases of the exact and FOCI spectra, where $\eta=0.01$, $n_{for}=21$, $n_{inv}=31$, and $f=40$ Hz.	60
Figure 3-9. In red are the wavenumbers of the spectrum of a 7 point filter. Note that the shaded area bounded by the solid lines contains only one wavenumber which means poor control.....	63
Figure 3-10. After spatial resampling of the j^{th} partition, the wavenumbers of a 7 point operator falls inside the wavelike region where k_{N_j} is the new Nyquist wavenumber, compare with Figure (3-9).....	63
Figure 3-11. Spectra of two operators, designed with and without spatial resampling, compared with the exact spectrum, where (a) and (b) show their amplitudes, and (c) and (d) show their phases. The parameters are: $\Delta x=10$ m, $\Delta z=10$ m, $f=40$ Hz., $V=2000$ m/s, $n_{op}=51$ points, and $\Delta x_j=70$ m.	66
Figure 3-12. The amplitudes spectra of Hale , Soubaras, WLSQ, and FOCI extrapolators in the wavenumber domain compared with the amplitude of the exact spectrum, where (a) shows a zoomed part of the amplitudes of the various extrapolators, and (b) shows the maximum amplitudes after applying the extrapolators 500 times in a homogenous medium.....	69

Figure 3-13. Phase errors the Hale, Soubaras, WLSQ, and FOCI extrapolators in the wavenumber domain.....	70
Figure 3-14. Impulse responses of the (a) phase-shift, (b) Hale, (c) Soubaras, (d) WLSQ and (e) FOCI extrapolators for $V=4000$ m/s, $\Delta x=10$ m, $\Delta z=10$ m, and a 31-point operator. The FOCI result was obtained using the spatial resampling technique.....	73
Figure 3-15. Prestack depth migration results from the Marmousi dataset, where (a) shows the reflectivity, and (b), (c), and (d) show the results with the Soubaras, WLSQ, and FOCI extrapolators, respectively (the dashed box contains the target).....	77
Figure 3-16. Zoomed parts of the shallow central sections of Figures 3-15a, 3-15b, 3-15c, and 3-15d.....	78
Figure 4-1. Amplitudes of the desired spectra in (a) the WLSQ, and (b) the WLSTB approaches. The dotted lines indicate the evanescent boundaries. The parameters are $\Delta x=10$ m, $\Delta z=10$ m, $f=50$ Hz, and $V=2000$ m/s.....	84
Figure 4-2. Amplitudes of the exact spectrum, WLSQ spectrum, and WLSTB spectrum, where $\Delta z=2$ m, $\Delta x=10$ m, $f=50$ Hz, $V=2000$ m/s, and $\alpha=70^\circ$...	86
Figure 4-3. Phases of the exact spectrum, WLSQ spectrum, and WLSTB spectrum, where $\Delta z=2$ m, $\Delta x=10$ m, $f=50$ Hz, $V=2000$ m/s, and $\alpha=70^\circ$	86
Figure 4-4. Impulse responses of the (a) phase-shift extrapolator, (b) WLSQ extrapolator, and (c) WLSTB extrapolator.....	88
Figure 4-5. A detailed comparison of the shallow central part of the Marmousi dataset, where (a) is the WLSQ result, and (b) is the WLSTB result. The arrows show some comparison areas.....	90
Figure 4-6. (a) Amplitudes and (b) phases of the exact, old forward, and optimized forward operators in the wavenumber domain. The parameters employed are $\Delta x=10$ m, $\Delta z=10$ m, and $f=40$ Hz, and the length spatial length of the forward operator is 21 points.....	94
Figure 4-7. (a) Amplitudes and (b) phases of the exact, old FOCI, and optimized FOCI operators in the wavenumber domain. The parameters employed are $\Delta x=10$ m, $\Delta z=10$ m, $f=40$ Hz, $\eta=1$, and the length of the FOCI operator is 51 points.....	95

Figure 4-8. (a) Amplitudes and (b) phases of the exact, old post-design operator, and optimized post-design operator in the wavenumber domain. The parameters are $\Delta x = 10$ m, $\Delta z = 10$ m, $f = 40$ Hz, and the operator length is 15 points.....	96
Figure 4-9. Impulse responses of (a) the phase-shift, (b) FOCI, and (c) the optimized FOCI algorithms using $\Delta x = 10$ m, $\Delta z = 10$ m, $V = 4000$ m/s, and an operator length of 15 points.	98
Figure 4-10. Impulse responses of the optimized FOCI algorithm implemented (a) without and (b) with spatial resampling, where an operator length of 11 points was used.	99
Figure 4-11. PSDM images of the Marmousi dataset, where (a) shows the result of the old FOCI algorithm, and (b) shows the result of the optimized algorithm. The box contains the target area, and the arrows show some comparison areas. The operator length is 15 points.	102
Figure 4-12. Close-up views of the shallow central sections of Figures 3-15a, 4-11a, and 4-11b.	103
Figure 4-13. PSDM image obtained with the optimized FOCI algorithm with a 9-point operator.	104
Figure 4-14. Comparisons of FOCI before and after the optimization at zoomed sections with various operator lengths, where (a) was obtained with the old FOCI with an operator length of 51 points, (b) was obtained with the optimized FOCI using an operator length of 51 points, (c) was obtained with the optimized FOCI using an operator length of 25 points, and (d) was obtained with the optimized FOCI using an operator length of 9 points.....	105
Figure 4-15. Runtimes versus operator lengths.	106
Figure 5-2. Elevation profile of the Aruma dataset.	116
Figure 5-3. The reflectivity of the Aruma dataset.....	116
Figure 5-4. The velocity model of the Aruma dataset.	117
Figure 5-5. The zero-offset time section of the Aruma dataset.	117
Figure 5-6. The modeled source wavefield, (a) before applying the source time-shift, and (b) after applying it, where the dashed line indicates the zero time line.....	118
Figure 5-7. Shot profile at a lateral position of 5000 m (a) before applying the static shifts, and (b) after applying them. The reference velocity is $V_o = 1000$ m/s.	119

Figure 5-8. The same shot profile as in Figure 5-6 but extrapolated to a depth of 500 m.	120
Figure 5-9. Single imaged shot profile that was shown in Figures 5-6 and 5-7.	120
Figure 5-10. The PSDM image of the Aruma dataset using the zero-velocity approach, where the dashed line indicates the lateral position of the shot profile that was shown in Figures 5-6 - 5-8.	121
Figure 5-11. Source-receiver extrapolation can be performed by sorting the data into a matrix for each frequency, where the rows represent the receivers, the columns represent the shots, S is the number of shots, and R is the number of receivers..	125
Figure 5-12. The PSDM image of the Aruma dataset using source-receiver migration with the laterally variable depth step approach.	126
Figure 5-13. Shot gather at a lateral position= 5000 m (a) as recorded from topography, and (b) after downward-continuation to a depth level of 500 m.	129
Figure 5-14. Imaged shot gather that was shown in Figure 5-13.	130
Figure 5-15. The PSDM image using the shot profile migration with a laterally variable depth approach.	130
Figure 6-1. Using $V_m \approx V$ for constant velocity migration generates a flat event in (a) the common image gather, where (b) is the PSDM image formed by stacking the common image gathers over offset. In this example, $V = 2000$ m/s and the reflector dip is 30 degrees.	135
Figure 6-2. Using $V_m \neq V$ for constant velocity migration generates a non-flat event in (a) the common image gather, where (b) is the PSDM image formed by stacking the common image gathers over x_s . In this example, $V = 2000$ m/s and $V_m = 2600$ m/s.	138
Figure 6-3. At each depth level, (a) the depth focusing gather is formed by cross-correlating the upgoing and downgoing wavefields, and (b) the depth focusing panel is formed by summing over x_s at each depth level. This is the same model that was used in Figure 6-1, where $V_m \approx V$. The dashed line indicates the zero-lag cross-correlation.	143
Figure 6-4. The depth focusing panel obtained with $V_m \neq V$. The dashed lines indicate the zero and focusing lags.	144

Figure 6-5. Examples of CFP gathers obtained with $V_m \approx V$, where (a) shows a CFP gather from the upgoing wavefield and (b) shows a CFP gather from the downgoing wavefield. The extrapolation depth equals the reflector point at the same lateral position shown in Figure 6-1a. 150

Figure 6-6. A DTS panel, $G_{df}(x_s, x_o, z_i = z_r, \tau; V_m)$, where $z_r=585$ m, $x_0=1000$ m, and $S=100$ for the same lateral position shown in Figure 6-1a. 151

Figure 7-1. A PSDM image obtained using $V_m \approx V$, where $V = 2000$ m/s. The dashed line shows a lateral position or analysis location that will be used in the next figures..... 159

Figure 7-2. The common image cube (CIC), where (a) is obtained with $V_m \approx V$, and (b) is obtained with $V_m > V$. The arrows indicate the zero-lag common image gathers (section 6-1), which are only slices of these cubes. The thick border indicates the location of $G_{df}(x_s, x_o, z, \tau = 0; V_m)$ 160

Figure 7-3. Slices of (a) the cube in Figure 7-2a and (b) the cube in Figure 7-2b at different lags. The thick border indicates the location of $G_{df}(x_s, x_o, z, \tau = \tau_f; V_m)$ 161

Figure 7-4. Composites of the upgoing and downgoing wavefields for three cases: (a) 10% velocity error, (b) 20% velocity error, and (c) 30% velocity error. The true traveltimes calculated using $V = 2000$ m/s is shown for comparison. 163

Glossary of terms

This glossary of technical terms provides context and meaning to many expressions and words used in this thesis.

Actual spectrum: the Fourier transform of a space-frequency compactly supported operator over the spatial coordinates.

Analysis location: a lateral position at which migration velocity analysis (MVA) is carried out.

Background velocity model: the velocity model used for migration that may or may not approximate the true velocity field.

Boxcar window: a function that is zero until the start of the segment, one during the segment, and zero after the segment.

Claerbout's imaging principle: a reflector exists at a point in the subsurface when the upgoing and downgoing wavefields are coincident in time and space.

Common focus point (CFP): a domain for migration velocity analysis (MVA) that is based on the principle of equal traveltimes.

Common image cube (CIC): formed, for an analysis location, by cross-correlating the upgoing and downgoing wavefields, and retaining all the cross-correlation lags at each depth level.

Common image cube analysis (CICA): a domain for migration velocity analysis (MVA) that is based on analyzing the common image cube (CIC).

Common image gather: a gather of imaged traces formed, for an analysis location, x_0 , by cross-correlating the upgoing and downgoing wavefields, and only retaining the zero-lag information at each depth level.

Compactly supported operator: a finite-length operator.

Cross-correlation imaging condition: the upgoing wavefield is multiplied by the conjugate of the downgoing wavefield.

Data space: the space of recorded seismic data.

Datum: a flat, horizontal, or regular surface.

Deconvolution imaging condition: the upgoing wavefield is divided by the downgoing wavefield.

Depth focusing analysis (DFA): a domain for migration velocity analysis (MVA) that is based on analyzing the depth focusing panel.

Depth focusing gather: formed, for a particular depth level and a specific analysis location, by cross-correlating the upgoing and downgoing wavefields, and retaining all the cross-correlation lags.

Depth focusing panel: formed, for an analysis location, by stacking the depth focusing gather over offset at each depth level.

Desired spectrum: the spectrum to be approximated in an optimization scheme such as the least-squares or the Remez exchange algorithm.

Differential time-shift (DTS): see depth focusing gather.

Downward-continuation: stepping, pushing, or marching the data into the subsurface.

Downgoing wavefield: a simulated wavefield obtained by simulating an impulse at the source location.

Depth-specific delay function: the traveltime difference between two particular events in the upgoing and downgoing wavefields.

Elevation profile: the elevation of sources and receivers with respect to a particular datum.

Elevation statics: any distortion of the reflection events of data recorded from an irregular surface.

Event surface: a particular reflection event in the common image cube (CIC).

Exact spectrum: the phase-shift operator in the wavenumber-frequency domain, or the ideal wavefield extrapolator in the wavenumber-frequency domain.

Explicit methods: the wavefield at an output position can be computed independently from the wavefield at neighbouring output points.

Explicit wavefield extrapolation: explicit space-frequency recursive downward-continuation.

Evanescent region: the region where the transverse wavenumber, k_x , is greater than the ratio ω/V .

Focusing depth: in DFA, the depth at which the maximum energy build-up occurs in the depth focusing panel. In CICA, however, it is the depth at which the flattest part of the event surface can be identified.

Focusing lag: the lag at which the flattest of the event surface can be found in the common image cube (CIC).

Focusing term: a component of the phase-shift operator that focuses the data.

FOCI extrapolator: the result of convolving an operator with the conjugate of its least-squares bandlimited inverse.

Generalized phase-shift plus interpolation algorithm: the limiting form of the phase-shift plus interpolation algorithm.

Gibbs phenomenon: the overshoot (or "ringing") that occurs when discontinuous functions, or functions with discontinuous slopes, are approximated with any number of coefficients.

Hale extrapolator: the inverse Fourier transform over the spatial coordinates of a spectrum formed by the superposition of cosine basis functions.

Ideal wavefield extrapolator: the inverse Fourier transform of the exact spectrum over the transverse wavenumber, which results into an infinitely long operator in the space-frequency domain.

Image space: where a reflectivity picture (image) of the subsurface can be obtained.

Image depth: depth at which reflection events appear in the imaging process using a background velocity model.

Imaging condition: the process by which reflectivity information is extracted from the extrapolated data.

Implicit methods: the wavefield at a specific output point is dependent upon the wavefield at neighbouring output points, where usually, all output points are computed simultaneously.

Kirchhoff migration methods: a combination of Green's theorem with the scalar-wave equation to develop an expression to calculate any image point from a weighted summation (integration) through the data.

Mathematical stability of an operator: the amplitude of the actual spectrum does not exceed unity in the wavelike region.

Migration: mapping from the data space to the image space that involves two steps: wavefield extrapolation and imaging condition.

Migration velocity analysis (MVA): the use of seismic imaging algorithms to build and update background velocity models.

Non-recursive algorithm: in which the wavefield at any depth level can be computed directly from the surface.

Nonstationary convolution: uses a different operator for each output point.

Offset: the surface separation, or the lateral distance, between two points such as source and receiver, or source and some analysis location.

Phase-shift operator: see the exact spectrum.

Phase-shift plus interpolation (PSPI) algorithm: in the presence of lateral velocity variations, the extrapolation is approximated by performing a set of constant velocity phase-shift extrapolations using a suitable set of reference velocities, then the reference wavefields, the output of the phase-shift extrapolations, are interpolated to obtain the result.

Practical stability: the amplitude of the actual spectrum deviates so slightly from unity where this deviation can be tolerated in a recursive scheme.

Pre-selected depth: an initial estimate of the reflector depth.

Principle of equal traveltimes: the background velocity model is acceptable if the traveltimes of two particular reflection events in the common focus point (CFP) gathers of the upgoing and downgoing wavefields are equal.

Recursive algorithm: the wavefield at each depth level is computed from the wavefield at the previous depth level.

Reflector depth: the true reflector depth.

Residual curvature analysis (RCA): a domain for migration velocity analysis (MVA) that analyzes the curvatures of reflection events on the common image gathers.

Shot profile: the data collected in a seismic experiment.

Seismic experiment: consists of seismic source or sources, and many receivers distributed on the surface. The seismic source sends sound waves that propagate through the various rock types and reflect at boundaries separating different rock types. As these reflected waves return to the surface, they get recorded by the receivers.

Slope of a spectrum: the first derivative of a spectrum with respect to the transverse wavenumber.

Soubaras extrapolator: based on using the Remez exchange algorithm and the L_∞ norm.

Spatial resampling: during the extrapolation process, the data are spatially resampled into partitions, where each partition is extrapolated separately. Then the extrapolated partitions are resampled back to the original spatial sample size.

Spectrum: data in the wavenumber-frequency domain.

Stationary convolution: the same operator is used to compute the wavefield at each output point.

Thin-lens term: a component of the phase-shift operator that applies time-shifts to the data.

Tomography: transforms the recorded seismic data into a velocity model of the subsurface.

Transition band: the band of wavenumbers of a transition region, in which the spectrum, or its slope, is discontinuous.

Transition region: the region that connects the wavelike and evanescent regions, which may consist of one sample or many samples.

Upgoing wavefield: the recorded seismic data.

Wavelike region: the region where the transverse wavenumber, k_x , is less than the ratio ω/V .

WLSQ extrapolator: based on a weighted least-squares approach that uses a model-based function as the desired transform.

WLSTB extrapolator: designed using a weighted least-squares approach that uses a special weight function to remove the transition band from the optimization.

Zero-offset section: the stacking of the zero-offset (source-receiver offset = 0) trace from each shot profile.

Zero velocity approach: the upgoing and downgoing wavefields are time-shifted in opposite directions, with respect to a datum, and then a special wavefield extrapolator is used for downward-continuation between the datum and recording surface.

List of symbols

B	Space-frequency basis function that is used in the Hale's method.
$diag$	Diagonal of a matrix.
d^+	The downgoing wavefield in the space-time domain.
D^+	The downgoing wavefield in the space-frequency domain.
E	The error measure.
F	The discrete Fourier transformation over the spatial coordinate.
f	Temporal frequency.
G	Green function in the space-frequency domain.
G_{ci}	Common image gather in the space-depth domain.
G_{df}	Depth focusing gathers.
h	Elevation profile.
H	Conjugate transpose.
i	$= \sqrt{-1}$
I	The PSDM image.

k	$k = \frac{\omega}{V}$
k_α	$k_\alpha = k \sin \alpha$, where α is the maximum propagation angle of interest.
k_N	Nyquist wavenumber.
k_x	Transverse wavenumber in 2D.
\bar{k}_x	Normalized transverse wavenumber used in Hale's method.
Δk_x	Transverse wavenumber sample interval.
k_z	The dispersion relation.
L_d	One-way operator for downgoing waves.
L_u	One-way operator for upgoing waves.
M	Number of basis functions used in Hale's method.
n_{for}	Length of the forward operator in FOCI.
n_{inv}	Length of the inverse operator in FOCI.
\mathbb{R}	Real numbers.
\mathbf{R}	Reflectivity.
R	Number of receivers.
S	Number of sources.
τ	Cross-correlation lag.

τ_f	Focusing lag used in DFA, CFP, and CICA methods.
t	Time coordinate.
t_d	The travelttime of an event in the downgoing wavefield.
t_u	The travelttime of an event in the upgoing wavefield.
u^-	The upgoing wavefield in the space-time domain.
U^-	The upgoing wavefield in the space-frequency domain.
x	The transverse coordinate.
x_0	A spatial lateral position; an analysis location.
x_r	Receivers coordinate.
x_s	Sources coordinate.
Δx	Space sample interval.
V	Constant Velocity constant.
$V(x)$	Velocity as a function of the transverse coordinate.

$V(z)$	Velocity as a function of the depth coordinate.
$V(x, z)$	Velocity as a function of the transverse and depth coordinates.
V_n	Velocity function for a depth interval n
ω	Angular frequency, $\omega = 2\pi f$.
W	Operator operating on a wavefield.
W	Ideal space-frequency wavefield extrapolator that is infinitely long.
\hat{W}	Exact spectrum, or the ideal wavefield extrapolator in the wavenumber-frequency domain.
\hat{W}_D	Desired spectrum.
\tilde{W}	Space-frequency compactly supported wavefield.
\tilde{W}_{for}	Space-frequency compactly supported forward operator.
\tilde{W}_{inv}	Space-frequency compactly supported inverse operator.

\tilde{W}_{win}	Space-frequency compactly supported post-design operator.
\hat{W}	Actual spectrum, or the compactly supported extrapolator in the wavenumber-frequency domain.
W_s	The thin-lens term of the exact spectrum.
\tilde{W}_f	A compactly supported approximation to the inverse Fourier transformation over the transverse wavenumber of the focusing term of the exact spectrum.
\hat{W}_B	The actual spectrum of the WLSTB extrapolator.
\hat{W}_F	The actual spectrum of the WLSQ extrapolator.
z	The depth coordinate.
z_d	Depth of the datum.
z_e	Depth of a reflection event.
z_f	Focusing depth.
z_i	Pre-selected depth.
z_r	Reflector depth.
\bar{z}	Mean depth.

Δz	Depth step.
Λ	Weight function.
ψ	Pressure wavefield in the space-frequency domain.
$\hat{\psi}$	Pressure wavefield in the wavenumber-frequency domain.
Ψ	Pressure wavefield in the space-time domain.
η	Parameter that controls the evanescent filtering in FOCI.
*	Complex conjugate.
\wedge	Indicates the wavenumber-frequency domain.
Θ	The kernel that is used in downward-continuation from topography.
Ω	Spatial window function.
\bullet	Convolution operation.
∇^2	The Laplacian.
\approx	Approximately equal.
$\underline{\quad}$	An underscore indicates a vector.
$\underline{\underline{\quad}}$	A double underscore indicates a matrix.
λ	Wavelength.

$\ \cdot \ $	The L_1 norm.
$\ \cdot \ $	The L_∞ norm.
$\langle \cdot \rangle$	Mean value.

CHAPTER 1: INTRODUCTION

1-1 THE SEISMIC EXPERIMENT

A simple seismic experiment consists of a source and many receivers (Figure 1-1). The seismic source, at the surface of the earth, sends sound waves that propagate through the various rock layers in the subsurface. At layer boundaries that separate structural discontinuities, the incident propagating waves, reflect, diffract, refract, transmit, or convert to other waves. The receivers on the surface of the Earth record these reflected waves as they return to the surface. The ratio of the incident wave amplitude to the reflected wave is commonly called the reflection coefficient or the reflectivity.

Seismic surveys can be considered as ensembles of experiments with a nonzero distance (offset) between sources and their respective receivers (Bleistein et al., 2001). This experiment is repeated for numerous source and receiver locations distributed over the surface, where each experiment is called a shot profile. The purpose of repeating this experiment is to obtain repeated echoes from each reflector element (image point) in the subsurface. Each receiver in a shot profile records the amplitudes of the reflected energy as a digital time series known as a seismogram. The collection of these seismograms, will be referred to as the data space,

$$\text{data space} \equiv \text{recorded data}(x_s, y_s, x_r, y_r, t), \quad (1.1)$$

where x_s and y_s define the lateral positions of the sources, x_r and y_r define the lateral positions of the receivers, and t is the travelttime of waves traveling from the source

down to the reflector and then back to the receivers. The data space defined in equation (1.1) is five dimensional.

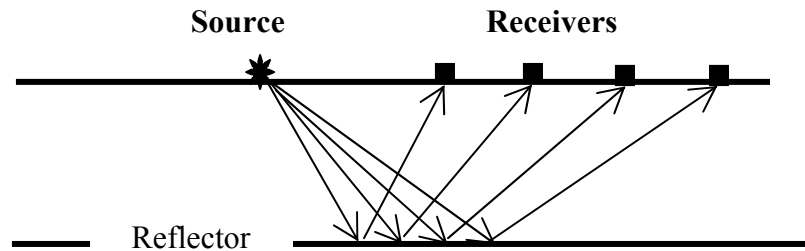


Figure 1-1. Schematic for a common shot gather for a flat reflector.

Migration can be defined as the “map” from data space to image space. The image is the reflectivity picture. The map is the function that moves us from one picture to the other (Figure 1-2). Migration algorithms (also called seismic imaging algorithms) can be divided into two major categories: integral methods or ray-based methods (e.g. Kirchhoff methods), and downward-continuation methods (Biondi, 2004; Margrave et al., 2006).

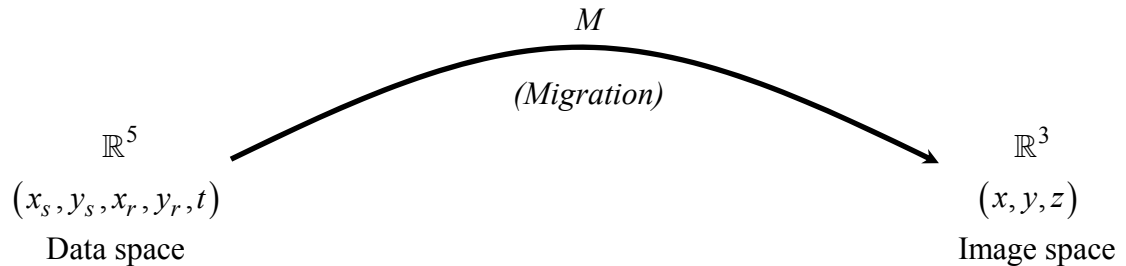


Figure 1-2. A schematic diagram showing how migration transforms the recorded data from the data space to the image space, where x and y are the transverse coordinates, M is a transformation operator or mapping operator, \mathbb{R}^5 and \mathbb{R}^3 refer to real numbers in 3 and 5 dimensions, respectively.

1-2 THE KIRCHHOFF METHODS

As described in Schneider (1978) and Docherty (1991), the Kirchhoff methods combine Green's theorem with the scalar-wave equation to develop an expression to calculate any image point from a weighted summation (integration) through the data (Margrave, 1998). The integration takes place over a traveltime surface that is defined by tracing rays using Snell's law from the image point to source and receiver locations. Thus, Kirchhoff methods are a combination of both wave theory and ray theory. They are called non-recursive methods because the wavefield at any depth level can be computed directly from the surface.

Kirchhoff migration has proven to be a robust migration method because it is computationally efficient and can handle irregular acquisition geometries (Bancroft, 2004). Further, it can be target-oriented, that is, the image at a specific depth level, or

levels, can be obtained without needing to image the entire volume. A major weakness of this method is its reliance on ray theory, that is, it assumes that seismic energy propagates along at most a few raypaths (usually one) between any two points (Gray et al., 2001). Strong lateral velocity variations, however, induce multipathing, i.e. the appearance of multiple raypaths connecting source and receiver locations with the image points (Stolk and Symes, 2004). Furthermore, even in almost homogeneous media, ray theory is only a high frequency approximation and significant energy propagates along a bundle of rays surrounding the Snell ray. Thus, in complex geology, images generated using Kirchhoff methods are less accurate than those generated using downward-continuation methods (Figure 1-3), which force multipathing between the surface points and the reflector points (Margrave, 1998; Gray et al., 2001; Margrave et al., 2006).

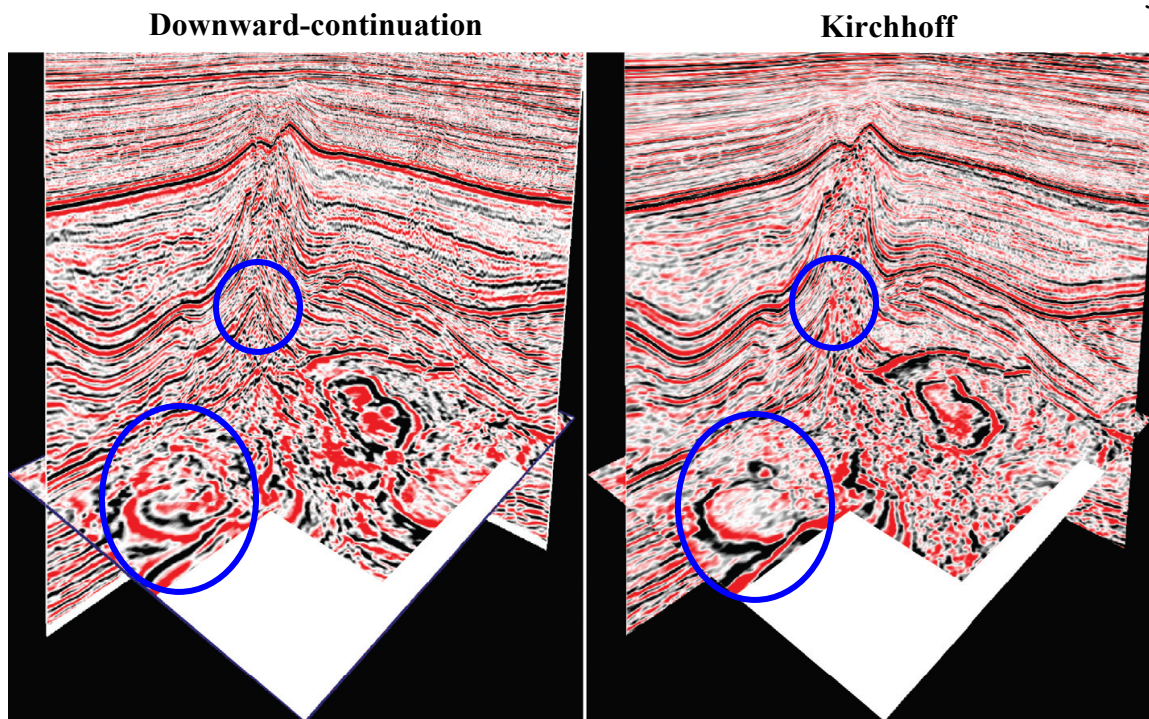


Figure 1-3. Comparison of downward-continuation migration versus Kirchhoff migration (Ren et al., 2005). Note the improved imaging of steeply-dipping events, leading to more details being visible in the depth slice of the migrated volume obtained using downward-continuation migration (the circles show some comparison areas).

1-3 DOWNWARD-CONTINUATION METHODS

Downward-continuation can be defined as the process in which the surface-recorded data are stepped ‘pushed’ down into the subsurface. In downward-continuation methods, an image of the subsurface is constructed by downward-continuing the data through small depth steps and invoking the imaging conditions at each depth level (Berkhout, 1981).

The imaging condition can be defined as the process by which the reflectivity information is extracted from the extrapolated data, where extrapolation here means the same thing as downward-continuation (section 2-2). These methods are recursive because the wavefield at each depth level is computed from the wavefield at the previous depth level. Downward-continuation methods can be applied in the wavenumber-frequency domain, the space-frequency, or the mixed-domain (wavenumber-frequency and space-frequency).

The phase-shift algorithm (Gazdag, 1978) is an example of a wavenumber-frequency method (section 2-1). On the other hand, the phase-shift-plus-interpolation (PSPI) algorithm (Gazdag and Sguazzero, 1984) (section 2-3), the split-step Fourier algorithm (Stoffa et al., 1990), the extended split-step algorithm (Kessinger, 1992), the Fourier finite-difference (FFD) algorithm (Ristow and Rühl, 1994), the extended local Born-Fourier algorithm (Huang et al., 1999), the generalized phase-shift-plus-interpolation (GPSPI) algorithm (Margrave and Ferguson, 1999), and the nonstationary phase shift (NSPS) algorithm (Margrave and Ferguson, 1999; Ferguson and Margrave, 2002) are all examples of downward-continuation methods that employ mixed-domain computations.

The space-frequency domain algorithms operate in the frequency domain to gain computational speed, and they can be either implicit or explicit. In explicit methods, the wavefield at an output position can be computed independently from the wavefield at neighbouring points. In implicit methods, however, the wavefield at a specific output point is dependent upon the wavefield at neighbouring output points, where usually, all output points are computed simultaneously. Thus, explicit methods are more flexible than implicit methods (Biondi, 2004). Explicit methods are computationally more efficient than implicit methods, but the latter are always numerically stable while the former are not. Hereafter, explicit space-frequency recursive downward-continuation will be referred to as “explicit wavefield extrapolation”.

1-4 WHY EXPLICIT WAVEFIELD EXTRAPOLATION?

In complex geology, explicit wavefield extrapolation is a powerful tool to obtain an accurate image of the subsurface (Holberg, 1988; Hale, 1991). To compute the wavefield at each output point, a different extrapolator can be used. Each extrapolator is calculated using the velocity at the output point. Thus explicit wavefield extrapolation methods carry out a nonstationary convolution in the space-frequency domain when there are lateral velocity variations (Figure 1-4), and stationary convolution otherwise (Figure 1-5). The wavefield extrapolators allow these methods to handle strong lateral velocity variations.

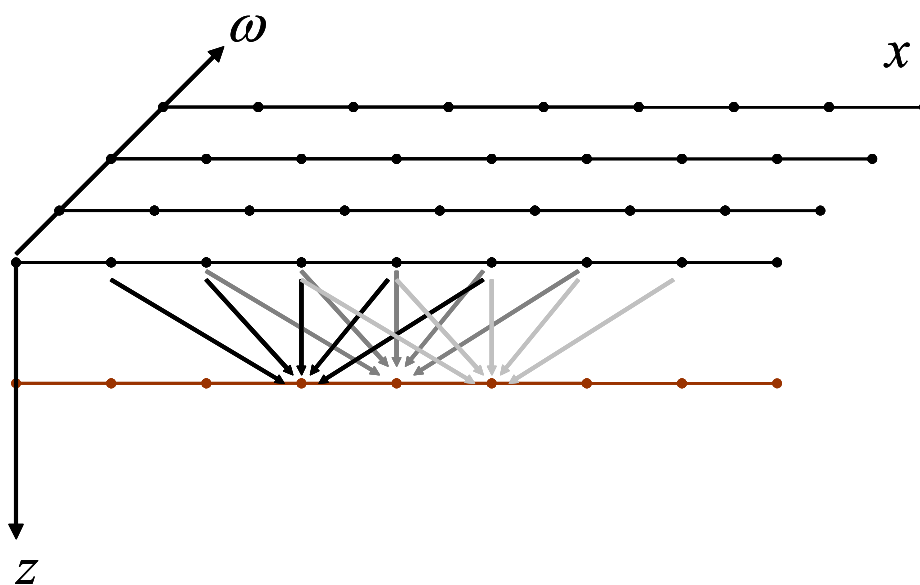


Figure 1-4 Nonstationary convolution when the velocity varies laterally. The different grey levels refer to operators calculated with different velocities.

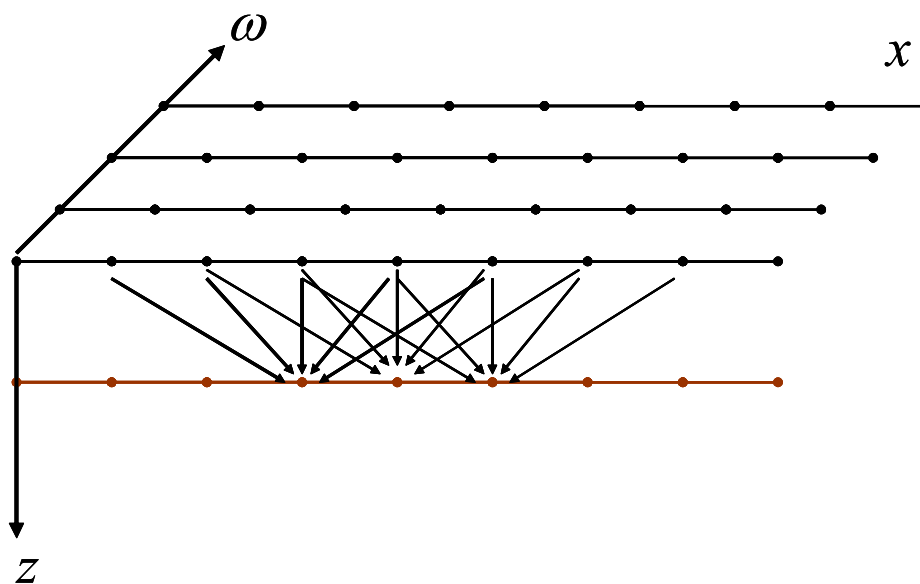


Figure 1-5 Stationary convolution where the wavefield at each output point is computed using the same operator.

1-5 CHALLENGES FOR EXPLICIT WAVEFIELD EXTRAPOLATION

METHODS

Wavefield extrapolation methods require an extrapolator (operator) that is numerically stable (section 2-5), and compactly supported, to make use of these methods. This desired extrapolator must also approximate the ideal space-frequency extrapolator, which is infinitely long. Unfortunately, designing such an extrapolator is not a straightforward problem because truncating the ideal extrapolator, in the space-frequency domain, induces numerical instability (section 2-5.1). Since explicit wavefield extrapolation is a recursive scheme, unstable operators will amplify the wavefield each time they are used. Further, operators designed with simple window functions such as a Hanning window have been known to either decay or amplify the wavefield each time they are applied (section 2-5.1).

The other shortcoming of these methods is that they assume extrapolation proceeds from a flat surface, whereas most land surveys are acquired on irregular surfaces. Moreover, these methods are very sensitive to velocity models (Berkhout, 1982; Yilmaz and Chambers, 1984; Claerbout, 1985; Al-Yahya, 1989; Deregowski, 1990; Liu and Bleistein, 1994; Varela et al., 1998). Using inaccurate velocity models generates low quality images.

1-7 CURRENT SOLUTIONS TO CHALLENGES FACING WAVEFIELD

EXTRAPOLATION METHODS

There are different methods that deal with the stability problem of explicit wavefield extrapolators. The objective of these methods is to design wavefield extrapolators that remain practically stable¹ in a recursive scheme (section 2-5). Some extrapolation methods use Taylor series expansion, least-squares, Chebyshev approximation, or a combination of these. For example, Holberg (1988) uses non-linear least-squares to design a wavefield extrapolator. Hale (1991) uses novel weighted basis functions to approximate the exact phase shift operator (section 3-1). Soubaras (1996) uses the Remez exchange algorithm to design wavefield extrapolators that have equiripple behaviour (section 3-2). Thorbecke et al. (2004) use a weighted least-squares approach with a transition function to design the extrapolator (section 3-3). Margrave et al. (2006) use Wiener filtering to design practically stable extrapolators (section 3-4.1), dual operator tables for evanescent filtering (section 3-4.2), and spatial downsampling of the lower frequencies to increase operator accuracy and decrease run times (section 3-4.3). All these approaches provide means for addressing the stability problem of wavefield extrapolators.

There are different approaches to downward-continue data recorded from irregular surfaces. One of the oldest approaches is the use of wave-equation datuming (section 5-1) prior to migration so that wavefield extrapolation methods can start from a flat surface.

¹ Practically stable here means that the extrapolator has a controlled instability (Margrave et al., 2006).

This, however, can be computationally expensive. The zero-velocity approach, which is less expensive than wave equation datuming, can also be used to deal with this problem (Beasley and Lynn, 1992).

The biggest challenge of explicit wavefield extrapolation methods in particular and all migration methods in general, is building an accurate velocity model of the subsurface. This task becomes even harder when complicated subsurface geological structures are present. There are some methods that are based on migration algorithms, which can be used for velocity analysis.

Using migration algorithms for estimating velocities is known as migration velocity analysis (MVA). It consists of two parts: the domain in which MVA is carried out, and the inversion scheme that is used to relate measurements in the MVA domain to velocity updates. Some domains include the residual moveout analysis (RCA, Al-Yahya, 1989) (section 6-1), the depth focusing analysis (DFA, Yilmaz and Chambers, 1984; Faye and Jeannot, 1986) (section 6-2), or the common focus point method (CFP, Berkhout, 1997.a; Berkhout, 1997.b; Thorbecke, 1997) (section 6-3). The inversion scheme can be either derived based on simplifying assumptions of the subsurface (see e.g. Al-Yahya, 1989), or be based on tomography (see e.g. Cox, 2001) (section 7-3).

1-8 THESIS MAIN CONTRIBUTIONS

The main contributions of this thesis can be summarized as follows:

- The comparison of different methods for designing wavefield extrapolators, and the analysis of the strengths and weaknesses of each method.
- The development of a new approach for designing practically stable wavefield extrapolators.
- The use of this approach to improve and optimize an existing method.
- The development of efficient approaches to downward-continue data directly from an irregular surface.
- The mathematical formulation of major concepts of MVA domains.
- The combination of different aspects of MVA domains into a unified one.

1-9 STRUCTURE OF THE THESIS

This thesis addresses three topics: the stability of explicit wavefield extrapolators, downward-continuation from irregular surfaces, and domains for MVA. Each topic begins with a literature review followed by ways to improve it.

Chapter 2 begins with a review of the theory of phase-shift extrapolation (section 2-1) followed by a review of the theory of shot profile migration (section 2-2). The phase-shift plus interpolation (PSPI) and generalized phase-shift plus interpolation (GPSPI) algorithms are reviewed and derived in section 2-3. From the theory of GPSPI, the theory of explicit wavefield extrapolation is derived (section 2-4). Later in that chapter, the stability problem of wavefield extrapolators is addressed (section 2-5).

Chapter 3 starts with a brief review of four explicit wavefield extrapolation methods. These methods are: Hale's (section 3-1), Soubaras's (section 3-2), WLSQ (section 3-3), and FOCI (section 3-4), followed by analyses of the accuracy and stability of these extrapolators by comparing their amplitude and phase spectra, impulse responses, and images of the Marmousi dataset (section 3-5).

In Chapter 4, the weighted least-squares using a transition band (WLSTB) method for designing wavefield extrapolators is presented (section 4-1.3). The similarities and differences between this method and the weighted least-squares (WLSQ, Thorbecke et al., 2004) approach are shown in section 4-2. Later in this chapter, the WLSTB is used to optimize the FOCI algorithm (section 4-3).

Downward-continuation from irregular surfaces is reviewed in Chapter 5. The theory of the zero-velocity approach is reviewed in section 5-1. Other approaches to downward-continue data from topography are developed in sections 5-2 and 5-3.

In Chapter 6 three industry-standard domains for MVA are reviewed. These domains are: residual curvature analysis (RCA) (section 6-1), depth focusing analysis (DFA) (section 6-2), and common focus point (CFP) (section 6-3). These domains are first derived in the same context, and then reformulated as mathematical hypotheses.

In Chapter 7, different aspects of the RCA, DFA, and CFP approaches are combined into a unified domain called common image cube analysis (CICA), where the CICA is stated as a mathematical hypothesis in section 7-1.

CHAPTER 2: THEORY OF EXPLICIT WAVEFIELD EXTRAPOLATION METHODS

The phase-shift algorithm (Gazdag, 1978) (section 2-1) operates in the wavenumber-frequency domain and can only handle vertical velocity variations. It has been extended to handle lateral velocity variations by Gazdag and Sguazzero (1984), resulting in an algorithm called the phase-shift plus interpolation (PSPI) (section 2-3). It is similar to the phase-shift algorithm, but instead of downward-continuing the wavefield with one constant velocity or ‘reference velocity’ per depth step, the wavefield is downward-continued with different reference velocities per depth step, and the final wavefield is obtained by interpolating these wavefields in the space-frequency domain.

Margrave and Ferguson (1999) extended the PSPI algorithm to its logical limits by introducing the generalized phase-shift plus interpolation (GPSPI) algorithm (section 2-3). The GPSPI algorithm operates in both the wavenumber-frequency and space-frequency domains, and honours the velocity of each output point. The generalized screen propagators (GSP1 and GSP2) of Le Rousseau and de Hoop (2001) are both approximations of the GPSPI algorithm (Margrave et al., 2002). The GPSPI algorithm is a very powerful tool for imaging complex geological subsurface structures, but it is computationally very expensive.

Explicit wavefield extrapolation methods operate in the space-frequency domain (section 2-4), and are also phase-shift-based algorithms. In fact, they are the space-frequency

equivalent of the GPSPI algorithm if the nonstationary convolution operators are infinitely long. Once the nonstationary convolution operators have a finite-length or ‘compact support’, they become an approximation to the GPSPI algorithm. The space-frequency methods are computationally more efficient than the GPSPI because they use shorter operators.

It is useful to review some basics of the phase-shift-based algorithms and to put them in the same context. Further, this review will help to understand the theory of explicit wavefield extrapolation methods. This chapter starts with a review of the phase-shift algorithm, followed by the theory of shot profile migration. Following that, a review of the PSPI and GPSPI algorithms is presented. Then, the theory of explicit wavefield extrapolation is presented. Finally, the numerical instability of wavefield extrapolators is addressed.

2-1 THE PHASE-SHIFT EXTRAPOLATION

The phase-shift algorithm (Gazdag, 1978) is only accurate for cases where velocity only varies with depth. The scalar wave equation governs the propagation, and Fourier transforms are used to decompose seismic wavefields into plane waves that are phase-shifted from the surface to new depths (Ferguson, 1999). The Fourier transform of the recorded pressure wavefield, $\Psi(x_T, z = 0, t)$, over the temporal coordinate can be expressed as

$$\psi(x_T, z = 0, \omega) = \int_{-\infty}^{\infty} \Psi(x_T, z = 0, t) \exp(-i\omega t) dt, \quad (2.1)$$

where t is the time coordinate, z is the depth coordinate, and ω is the angular frequency defined as

$$\omega = 2\pi f, \quad (2.2)$$

where f is the temporal frequency. The transverse spatial coordinates are referred to as $x_T = x$ for two dimensions (2D), and $x_T = (x, y)$ for three dimensions (3D).

Consider the following problem, given these two boundary conditions:

$$a(x_T, \omega) = \psi(x_T, z = 0, \omega) \quad (2.3)$$

and

$$b(x_T, \omega) = \left[\frac{\partial \psi}{\partial z}(x_T, z, \omega) \right]_{z=0}, \quad (2.4)$$

estimate the wavefield at some depth z , $\psi(x_T, z, \omega)$. To solve this problem, let's start with the constant-velocity Helmholtz equation

$$\nabla^2 \psi(x_T, z, \omega) + \frac{\omega^2}{V^2} \psi(x_T, z, \omega) = 0, \quad (2.5)$$

where ∇^2 is the Laplacian with respect to x_T and z , and V is the velocity (constant).

Taking the Fourier transforms over the spatial coordinates of equation (2.5) gives

$$\frac{\partial^2}{\partial z^2} \hat{\psi} + k_z^2 \hat{\psi} = 0, \quad (2.6)$$

where

$$k_z^2 = k^2 - k_T^2, \quad (2.7)$$

$$k = \frac{\omega}{V}, \quad (2.8)$$

and

$$\hat{\psi}(k_T, z, \omega) = \int_{\mathbb{R}^{n-1}} \psi(x_T, z, \omega) \exp(ik_T \cdot x_T) dx_T. \quad (2.9)$$

\mathbb{R}^{n-1} refers to the real numbers in $n-1$ dimensions, $k_T \cdot x_T = k_x x + k_y y$ in 3D and

$k_T \cdot x_T = k_x x$ in the 2D case, $n=3$ in 3D and $n=2$ in the 2D case, and “ $\hat{\cdot}$ ” denotes the

Fourier transform over the spatial coordinates. For a homogeneous medium, the total wavefield can be decoupled into upgoing and downgoing waves. So equation (2.6) can be written as

$$L_d L_u \hat{\psi} = 0, \quad (2.10)$$

where L_d is the one-way operator for downgoing waves (the subscript “ d ” indicates downgoing waves)

$$L_d = \left(\frac{\partial}{\partial z} + ik_{z_d} \right), \quad (2.11)$$

and L_u is the one-way operator for upgoing waves (the subscript “ u ” indicates upgoing waves)

$$L_u = \left(\frac{\partial}{\partial z} - ik_{z_u} \right). \quad (2.12)$$

The dispersion relation, k_{z_d} , for downgoing waves can be defined as

$$k_{z_d} = \begin{cases} \sqrt{k^2 - k_T^2}; & |k| > |k_T| \\ -i\sqrt{k_T^2 - k^2}; & |k| < |k_T| \end{cases}, \quad (2.13)$$

and the dispersion relation for upgoing waves can be defined as

$$k_{z_u} = \begin{cases} \sqrt{k^2 - k_T^2}; & |k| > |k_T| \\ i\sqrt{k_T^2 - k^2}; & |k| < |k_T| \end{cases}, \quad (2.14)$$

where $\sqrt{\quad}$ is chosen to be a positive square root, and the sign choices for the square roots in equations (2.13) and (2.14) will be apparent soon. The region where $|k_T| < |k|$ is called the wavelike region or the propagating waves region, and $|k_T| > |k|$ is called the evanescent region or the evanescent waves, which are exponentially growing or decaying with depth. For the homogeneous case, the total wavefield, $\hat{\psi}$, can be decomposed into downgoing waves, $\hat{\psi}_d$, and upgoing waves, $\hat{\psi}_u$, as in

$$\hat{\psi} = \hat{\psi}_d + \hat{\psi}_u, \quad (2.15)$$

and equation (2.10) can be rewritten as

$$L_d L_u (\hat{\psi}_d + \hat{\psi}_u) = L_u L_d \hat{\psi}_d + L_d L_u \hat{\psi}_u = 0, \quad (2.16)$$

where the operators L_d and L_u only commute for the homogeneous case. Equation (2.6) can be satisfied by letting

$$L_d \hat{\psi}_d = 0 \quad (2.17)$$

and

$$L_u \hat{\psi}_u = 0, \quad (2.18)$$

where equations (2.17) and (2.18) are one-way wave equations whose solutions can be found in these forms

$$\hat{\psi}_d = \hat{D}(k_T, \omega) \exp(-ik_{z_d} z) \quad (2.19)$$

and

$$\hat{\psi}_u = \hat{U}(k_T, \omega) \exp(ik_{z_u} z), \quad (2.20)$$

where \hat{D} and \hat{U} are arbitrary functions to be determined from the boundary conditions.

The total wavefield can then be written as

$$\hat{\psi}(k_T, z, \omega) = \hat{D}(k_T, \omega) \exp(-ik_{z_d} z) + \hat{U}(k_T, \omega) \exp(ik_{z_u} z). \quad (2.21)$$

Equation (2.21) shows that the total wavefield is separated into an upgoing (up traveling) wave, $\hat{U}(k_T, \omega)$, and a downgoing wave (down traveling) wave, $\hat{D}(k_T, \omega)$, based on the sign of z . When there are lateral velocity variations, but no vertical variations, $\hat{U}(k_T, \omega)$ and $\hat{D}(k_T, \omega)$ are decoupled, that is, they propagate independently of each other (Fishman and McCoy, 1985).

The two boundary conditions, defined in equations (2.3) and (2.4), are needed to determine the arbitrary functions of equation (2.21). Evaluating equation (2.21) at $z = 0$, and using the first boundary condition, (equation (2.3)), give

$$\hat{a}(k_T, \omega) = \hat{U}(k_T, \omega) + \hat{D}(k_T, \omega), \quad (2.22)$$

where $\hat{a}(k_T, \omega)$ is the spatial Fourier transformation of $a(x_T, \omega)$. The complete determination of $\hat{U}(k_T, \omega)$ and $\hat{D}(k_T, \omega)$ requires the second boundary condition (equation (2.4)). In exploration seismology, however, $\partial\psi/\partial z$ is not recorded. As a result, it is usually assumed that only upgoing waves are recorded. According to this assumption, the downgoing wavefield, $\hat{D}(k_T, \omega)$ in equation (2.21), is zero, i.e., reflections, multiple reflections, and head waves and mode conversions are not generated

(Holberg, 1988). This also means that the wavefield, to be downward-continued, is strictly an upgoing wave

$$\psi(x_T, z, \omega) = \frac{1}{(2\pi)^{n-1}} \int_{\mathbb{R}^{n-1}} \hat{\psi}(k_T, 0, \omega) \hat{W}(k_T, z, \omega) \exp(-ik_T \cdot x_T) dk_T, \quad (2.23)$$

where

$$\hat{W}(k_T, k, z) = \exp(ik_z z), \quad (2.24)$$

and

$$k_z = k_{z_u}. \quad (2.25)$$

Note that choosing the sign convention in equation (2.14) ensures the decaying of the evanescent waves when $|k| < |k_T|$. Equation (2.23) is called the phase-shift extrapolation (Gazdag, 1978). The symbol, \hat{W} , is known as the phase-shift operator, the wavefield extrapolator in the Fourier domain, or the symbol of the wavefield extrapolation operator. In this derivation, the velocity was assumed constant in all coordinates.

Phase-shift extrapolation can handle vertical velocity variations by dividing the subsurface into depth intervals with differing velocities. That is, continuous velocity variation in depth is accommodated in the limit of infinitesimally small depth intervals (Ferguson, 1999), where the velocity remains constant in each interval. The wavefield is then phase-shifted one depth interval at a time, where the transmission coefficient correction at the boundary interface is neglected because including it in the derivation adds clutter to the equations without improving the results significantly (Claerbout, 1985).

2-2 SHOT PROFILE MIGRATION

Migration consists of two steps: wavefield extrapolation and imaging condition. From the previous section, the phase-shift algorithm can be used to accomplish the first step, provided that the velocity only varies with depth. In the second step, an image of the subsurface can be obtained by invoking the imaging condition, which will be described shortly.

There are two widely-used downward-continuation algorithms for imaging recorded seismic data. These algorithms are shot-profile and source-receiver migrations (Claerbout, 1971; Claerbout, 1985). In this section, the shot profile migration is described, while source-receiver migration will be described in section 5-2.

Let's first assume that a 2D background velocity model, $V(z)$, that approximates the true velocity field is available to define the extrapolation operators. Note that the velocity model has only vertical velocity variations. In a 2D setting, the Fourier transform of the recorded wavefield, $\Psi(x_s, x, z = 0, t)$, over the temporal coordinate, can be described as

$$\psi(x_s, x, z = 0, \omega) = \int_{-\infty}^{\infty} \Psi(x_s, x, z = 0, t) \exp(-i\omega t) dt, \quad (2.26)$$

where $x_T = x$, x_s is the source coordinate, and s is an integer source index ranging from 1 to S , the number of sources. In shot profile migration, two wavefields are considered: the upgoing and downgoing wavefields, which will be described shortly. Downward-continuing the recorded upgoing wavefield to $z = N\Delta z$, where Δz is a depth step and

$N > 0$ is an integer number such that $N\Delta z$ gives the maximum depth of interest, can be described as

$$U^-(x_s, x, N\Delta z, \omega) = \left[\prod_{n=1}^N \mathbf{W}_{n\Delta z} \right] U_o^-(x_s, x, N\Delta z, \omega), \quad (2.27)$$

where U_o^- can be defined as

$$U_o^- \equiv \psi(x_s, x, z = 0, \omega), \quad (2.28)$$

where $\Delta z \leq \lambda_{\min} / 2$, $\lambda_{\min} = V_{\min} / \omega_{\max}$, $V_{\min} = \min(V(z))$, and ω_{\max} is the maximum frequency.

The superscript “-” in equation (2.28) explicitly indicates a backward extrapolation.

Also, n is an integer such that $n\Delta z$ gives a particular depth. The cascade of operators

$\mathbf{W}_{n\Delta z}$ can be described by

$$\prod_{n=1}^N \mathbf{W}_{n\Delta z} = \mathbf{W}_{N\Delta z} \circ \mathbf{W}_{(N-1)\Delta z} \circ \dots \circ \mathbf{W}_{\Delta z}. \quad (2.29)$$

In this expression, $\mathbf{W}_{n\Delta z}$ indicates an operator operating on a wavefield, and \circ denotes operator composition. In a one-way wavefield extrapolation, the n^{th} operator depends only upon the mean value of $V(z)$ in the interval $z \in [(n-1)\Delta z, n\Delta z]$.

Applying the first operator² to the recorded or upgoing wavefield can be described by

² The first operator here means the operator that extrapolates the data from the recording surface at $z = 0$ to the first extrapolation depth level.

$$\begin{aligned} (\mathbf{W}_{1\Delta z} U_o^-)(x_s, x, \Delta z, \omega) = \\ \frac{1}{2\pi} \int_{\mathbb{R}} \hat{\psi}(x_s, k_x, z=0, \omega) \hat{W}(k_x, k_{n=1}, \Delta z) \exp(-ik_x x) dk_x, \end{aligned} \quad (2.30)$$

where

$$\hat{\psi}(x_s, k_x, z, \omega) = \int_{\mathbb{R}} \psi(x_s, x, z=0, \omega) \exp(ik_x x) dx, \quad (2.31)$$

$$\hat{W}(k_x, k_n, \Delta z) = \exp(ik_{z_n} \Delta z), \quad (2.32)$$

$$k_{z_n} = \begin{cases} \sqrt{k_n^2 - k_x^2}; & |k_n| \geq |k_x| \\ i\sqrt{k_x^2 - k_n^2}; & |k_n| < |k_x| \end{cases}, \quad (2.33)$$

and

$$k_n = \frac{\omega}{V_n}. \quad (2.34)$$

In equation (2.34), V_n is some appropriate average of $V(z)$ over the interval

$$z \in [(n-1)\Delta z, n\Delta z], \quad (2.35)$$

that is, the phase-shift operator in equation (2.32) is calculated using the velocity of the depth interval n .

The downgoing wavefield is not a recorded wavefield, but can be obtained by simulating an impulse at the source location, x_s . The source function can be described as an impulse at zero time, and a delta function in space (Claerbout, 1971). The 2D Green function can be used to model the downgoing wavefield to the first depth level according to

$$D_{n=1}^+ \equiv G(x_s, x, \Delta z, V_{n=1}, \omega), \quad (2.36)$$

where G symbolizes the 2D Green function, which can be approximated using (Geiger, 2001)

$$G(x_s, x, \Delta z, V_{n=1}, \omega) \simeq \frac{\sqrt{2\pi V_{n=1} r}}{4\pi r \sqrt{-i\omega}} \exp(i\omega r / V_{n=1}), \quad (2.37)$$

where $r = \sqrt{(x_s - x)^2 + \Delta z^2}$. The superscript “+” in the equation (2.36) explicitly

indicates a forward modeling. Forward modeling the downgoing wavefield to the second depth level, $2\Delta z$, can be described as

$$\left(\mathbf{W}_{2\Delta z}^* D_{n=1}^+ \right) (x_s, x, 2\Delta z, \omega) = \frac{1}{2\pi} \int_{\mathbb{R}} \hat{G}(x_s, k_x, \Delta z, V_{n=1}, \omega) \hat{W}(k_x, k_{n=2}, \Delta z) \exp(-ik_x x) dk_x, \quad (2.38)$$

where

$$\hat{G}(x_s, k_x, \Delta z, V_{n=1}, \omega) = \int_{\mathbb{R}} G(x_s, x, \Delta z, V_{n=1}, \omega) \exp(ik_x x) dx. \quad (2.39)$$

Also, forward modeling the downgoing wavefield to the maximum depth of interest,

$N\Delta z$, can be described as

$$D^+(x_s, x, N\Delta z, \omega) = \left[\prod_{n=2}^N \mathbf{W}_{n\Delta z}^* \right] D_{n=1}^+ (x_s, x, N\Delta z, \omega), \quad (2.40)$$

where “*” means the complex conjugate.

So downward-continuing the upgoing wavefield and forward-modeling the downgoing wavefield, to a depth level $z = N\Delta z$, can be accomplished by applying a cascade of operators (equations (2.27) and (2.40)) to them. Then, the extrapolated upgoing and downgoing wavefields can be used to generate an approximate reflectivity map of the subsurface, which will be shown next.

The principle of reflector mapping was first introduced by Claerbout in 1971. According to Claerbout's imaging principle, a reflector exists at a point where the upgoing and the downgoing wavefields coincide in time and space. An estimate of the reflectivity \mathbf{R} , for frequency ω , can be given as

$$\mathbf{R}(x_s, x, z, \omega) \approx \frac{U^-(x_s, x, z, \omega)}{D^+(x_s, x, z, \omega)}. \quad (2.41)$$

Summing over all frequencies in equation (2.41) approximates the true-amplitude reflectivity,

$$\mathbf{R}(x_s, x, z) \approx \sum_{\omega} \frac{U^-(x_s, x, z, \omega)}{D^+(x_s, x, z, \omega)}, \quad (2.42)$$

but under ideal conditions (e.g. no noise) (Claerbout, 1971). Equation (2.42) is called the deconvolution imaging condition. To avoid dividing by small values of the downgoing wavefield in equation (2.42) and to account for noise, Claerbout (1971) suggested multiplying the upgoing and downgoing wavefields in equation (2.42) by the conjugate of the downgoing wavefield according to

$$\mathbf{R}(x_s, x, z) \approx \sum_{\omega} \frac{U^-(x_s, x, z, \omega)}{D^+(x_s, x, z, \omega)} \frac{D^+(x_s, x, z, \omega)^*}{D^+(x_s, x, z, \omega)^*}. \quad (2.43)$$

Since the denominator in equation (2.43) is now real, it can only affect the amplitudes of the final image but not the phase (position of the reflector), so it can be omitted with a consequent amplitude error. This yields to the crosscorrelation imaging condition

$$\mathbf{R}(x_s, x, z) \approx \sum_{\omega} U^-(x_s, x, z, \omega) D^+(x_s, x, z, \omega)^*. \quad (2.44)$$

Valenciano and Biondi (2003) added a stability factor to the deconvolution imaging condition to avoid dividing by small values of the downgoing wavefield

$$\mathbf{R}(x_s, x, z) \approx \sum_{\omega} \frac{U^-(x_s, x, z, \omega) D^+(x_s, x, z, \omega)^*}{D^+(x_s, x, z, \omega) D^+(x_s, x, z, \omega)^* + \varepsilon^2(x_s, x, z, \omega)}, \quad (2.45)$$

where

$$\varepsilon^2(x_s, x, z, \omega) = \mu \langle D^+(x_s, x, z, \omega) D^+(x_s, x, z, \omega)^* \rangle, \quad (2.46)$$

μ is a weighting factor that is less than one, and $\langle \rangle$ indicates taking the mean. An average reflectivity as seen over the available incidence angles at any point in (x, z) can be obtained by (de Bruin et al., 1990)

$$I(x, z) = \sum_{x_s} \mathbf{R}(x_s, x, z), \quad (2.47)$$

where the contribution of each shot (located at x_s) is added to form the final image. This type of migration is commonly known as prestack depth migration. Hereafter, the final image, obtained using this type of migration, will be referred to as prestack depth migration (PSDM) image.

There is another type of migration, called poststack migration, in which the stacking operator is applied before applying the migration operator. The migration and stacking operators do not commute; as a result, the prestack and poststack migration results are not equivalent. In fact, the relationships between them are quite complicated and beyond the scope of this discussion (see e.g. Yilmaz (1987) for a good discussion).

2-3 THE PHASE-SHIFT PLUS INTERPOLATION (PSPI) AND THE GENERALIZED PHASE-SHIFT PLUS INTERPOLATION (GPSPI) ALGORITHMS

In the derivation of the phase-shift algorithm, it was assumed that the phase-shift extrapolator does not depend on the transverse coordinates, x_T . Gazdag and Squazzerro (1984) extended the phase-shift algorithm to build an approximate extrapolation when the velocity varies in the transverse coordinates. This can be accomplished by performing a set of constant velocity phase-shift extrapolations using a suitable set of reference velocities (Margrave and Ferguson, 1999). The number of reference velocities is chosen such that they sample the fluctuation and the extremes of $V(x)$ for a particular depth interval. The resultant algorithm is called a phase-shift plus interpolation (PSPI).

Each wavefield that results from the phase-shift extrapolation with a reference velocity is called a reference wavefield. For example, a reference wavefield, $\psi_j(x, \Delta z, \omega)$, extrapolated from the surface at $z = 0$ to a depth $z = \Delta z$ can be described as

$$\psi_j(x, \Delta z, \omega) = \frac{1}{2\pi} \int_{\mathbb{R}} \hat{\psi}(k_x, 0, \omega) \hat{W}(k_x, k_j, \Delta z) \exp(-ik_x x) dk_x, \quad (2.48)$$

where $V_j = V(x_j)$ is a reference velocity, x_j is a specific lateral position, and $j > 0$ is an integer. The phase-shift operator, $\hat{W}(k_x, k_j, \Delta z)$, can be defined as

$$\hat{W}(k_x, k_j, z) = \exp(ik_{z_j} \Delta z), \quad (2.49)$$

where

$$k_{z_j} = \begin{cases} \sqrt{k_j^2 - k_x^2}; & |k_j| > |k_x| \\ i\sqrt{k_x^2 - k_j^2}; & |k_j| < |k_x| \end{cases}, \quad (2.50)$$

and

$$k_j = \frac{\omega}{V_j}. \quad (2.51)$$

In PSPI, the fundamental assumption is that the desired extrapolation is equivalent to a reference wavefield wherever the actual velocity equals the reference velocity (Margrave and Ferguson, 1999), that is

$$\psi(x_j, \Delta z, \omega) = \psi_j(x_j, \Delta z, \omega), \text{ if } V(x_j) = V_j. \quad (2.52)$$

Reference wavefields are generated using the reference velocities, and the extrapolated wavefield through $V(x)$, $\psi(x, \Delta z, \omega)$, can be approximated using

$$\psi(x, \Delta z, \omega) \approx LI(\psi_j(x, \Delta z, \omega), \psi_{j+1}(x, \Delta z, \omega)), \quad V_j < V(x) < V_{j+1}, \quad (2.53)$$

where LI indicates an interpolation process, V_{j+1} is another reference velocity, and ψ_{j+1} is a reference wavefield generated using V_{j+1} . The accuracy of the final result depends on the number of reference velocities and the interpolation scheme.

When the reference wavefield is generated for every distinct velocity, the PSPI algorithm converges to

$$\psi(x, \Delta z, \omega) = \frac{1}{2\pi} \int_{\mathbb{R}} \hat{\psi}(k_x, 0, \omega) \hat{W}(k_x, k(x), \Delta z) \exp(-ik_x x) dk_x, \quad (2.54)$$

where

$$\hat{W}(k_x, k(x), \Delta z) = \exp(ik_z(x)\Delta z), \quad (2.55)$$

$$k_z(x) = \begin{cases} \sqrt{k^2(x) - k_x^2}, & |k(x)| > |k_x| \\ i\sqrt{k_x^2 - k^2(x)}, & |k(x)| < |k_x| \end{cases}, \quad (2.56)$$

and

$$k(x) = \frac{\omega}{V(x)}. \quad (2.57)$$

Equation (2.54) is the limiting form of PSPI because it honours the velocity of each output point. Equation (2.54) is known as the generalized phase-shift plus interpolation method (GPSPI, Margrave and Ferguson, 1999). Note that the symbol \hat{W} is now a function of the transverse coordinate, x . The inverse Fourier integral over the transverse wavenumbers in equation (2.54) is not as straightforward as it was in equation (2.23) — that is, it needs much more computational effort. Margrave and Ferguson (1999) refer to equation (2.54) as a Fourier-integral operator that explicitly gives the extrapolated wavefield in terms of a phase-shift operator applied to the Fourier transform of the input wavefield. Equation (2.54) is referred to by Fishman and McCoy (1985) as a high-frequency approximation on the symbol of the exact Fourier-integral operator solution. In this case, it is the exact symbol that has been expanded, rather than taking the asymptotic expansion of the wavefield, as in the ray-based methods (Margrave et al., 2006). Fishman (2005) also refers to equation (2.54) as the locally homogenous approximation. Further, equation (2.54) reduces to the phase-shift algorithm when the velocity is constant.

2-4 SPACE-FREQUENCY DOMAIN WAVEFIELD EXTRAPOLATION

The GPSPI algorithm can be equivalently expressed in the space-frequency domain by explicitly inserting the Fourier transform of the input wavefield as in

$$\psi(x, \Delta z, \omega) =$$

$$\frac{1}{2\pi} \int_{\mathbb{R}} \left[\int_{\mathbb{R}} \psi(x', 0, \omega) \exp(ik_x x') dx' \right] \hat{W}(k_x, k(x), \Delta z) \exp(-ik_x x) dk_x, \quad (2.58)$$

where x' describes the transverse coordinate at input, and x describes the transverse coordinate at output. Rearranging the integrals in (2.58) results in

$$\psi(x, \Delta z, \omega) = \frac{1}{2\pi} \int_{\mathbb{R}} \psi(x', 0, \omega) \left[\int_{\mathbb{R}} \hat{W}(k_x, k(x), \Delta z) \exp(-ik_x (x - x')) dk_x \right] dx'. \quad (2.59)$$

Rewriting equation (2.59) gives

$$\psi(x, \Delta z, \omega) = \int_{\mathbb{R}} \psi(x', 0, \omega) W(x - x', k(x), \Delta z) dx', \quad (2.60)$$

where

$$W(x - x', k(x), \Delta z) = \frac{1}{(2\pi)} \int_{\mathbb{R}} \hat{W}(k_x, k(x), \Delta z) \exp(-ik_x (x - x')) dk_x. \quad (2.61)$$

Equation (2.60) is the theoretical basis for space-frequency explicit wavefield extrapolation methods. The convolution in equation (2.60) becomes nonstationary when the velocity varies with the transverse coordinate, x , and is stationary otherwise. By using the nonstationary convolution operator, W , lateral velocity variation can be accommodated where for each output point a different operator can be used. The

nonstationary convolution operator, W , is also called the wavefield extrapolator in the space-frequency or the Schwartz kernel of the wavefield extrapolation operator³.

2-5 THE STABILITY PROBLEM OF EXPLICIT WAVEFIELD EXTRAPOLATORS

The ideal wavefield extrapolation operator, W , is infinitely long (equation (2.61)) — that is, it is not compactly supported. For a practical implementation of equation (2.60), a finite-length operator that approximates the ideal extrapolator is required. Explicit wavefield extrapolation that uses a finite-length operator rather than the ideal operator is a useful approximation to the GPSPI integral only if the operator is numerically stable, which is the subject of the next section.

2-5.1 Numerical instability

The numerical instability can result from approximating the infinitely long operator with a finite-length operator. Let's denote the truncated operator in the space-frequency domain as \tilde{W} , and its Fourier transform over the spatial coordinates as \hat{W} . Hereafter, \hat{W} will be referred to as the actual spectrum of \tilde{W} , where the phase-shift operator, \hat{W} , will be referred to as the exact spectrum. Figure 2-1 shows the amplitude and the phase of the exact spectrum for a particular frequency.

³ It is also the inverse Fourier transform of the symbol of the GPSPI over the transverse wavenumber coordinate.

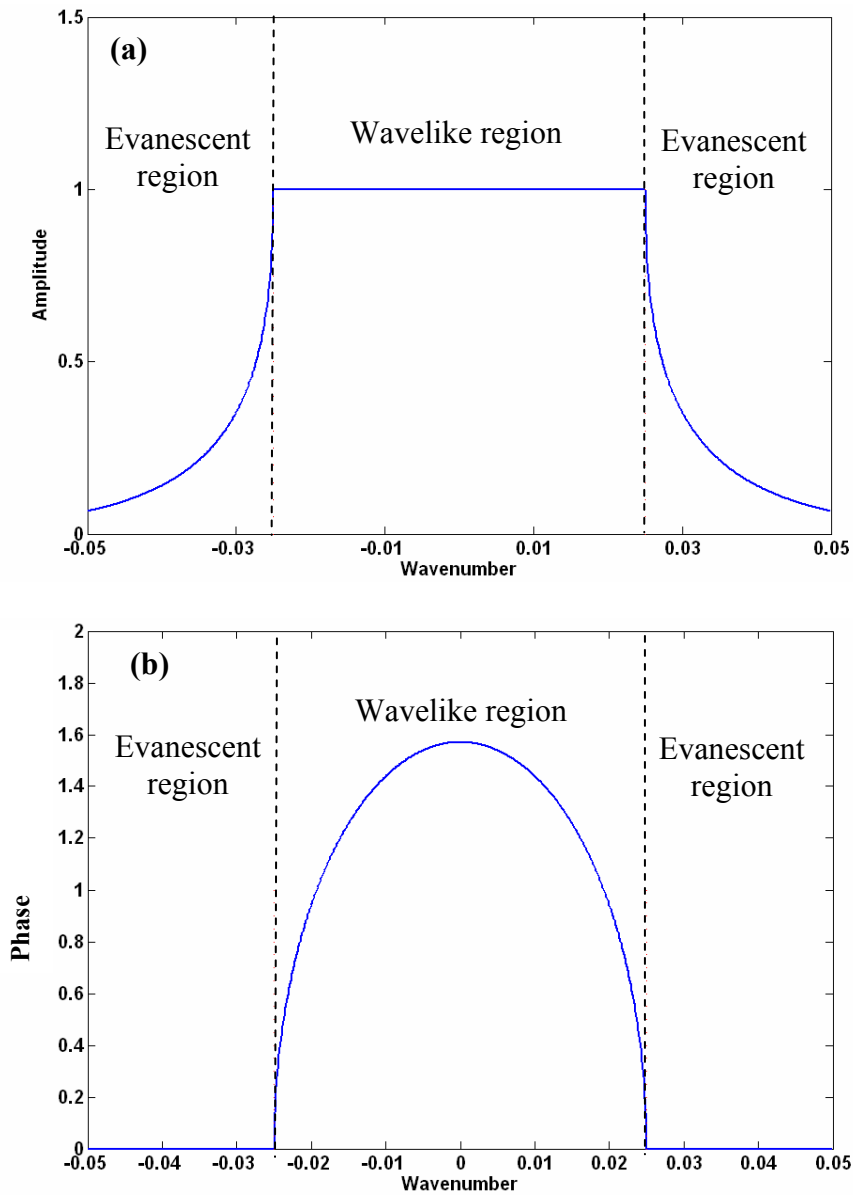


Figure 2-1. The (a) amplitude and (b) phase spectra of the exact spectrum, where $\Delta x = 10$ m, $\Delta z = 10$ m, $f = 50$ Hz, and $V = 2000$ m/s. The dashed lines indicate the evanescent boundaries.

Figure 2-2 shows the amplitude and phase of the exact spectrum for different frequencies.

The wavelike region is where $|k_x| < |k|$, and the evanescent region is where $|k_x| > |k|$.

These figures show that the slope (first derivative with respect to the transverse wavenumber) of the exact spectrum is discontinuous at the evanescent boundaries. These boundaries separate the wavelike and evanescent regions. Note that the amplitude of the exact spectrum is exactly one for the wavelike region and less than one for the evanescent region (Figure 2-1a).

One of the difficulties of the Fourier series is the *Gibbs phenomenon*, first observed by H. Wilbraham in 1848 and then analyzed in detail by Josiah W. Gibbs (1839–1903). The *Gibbs phenomenon* is simply an overshoot (or "ringing") of a Fourier series occurring at simple discontinuities. It occurs when discontinuous functions, or functions with discontinuous slopes, are approximated with any number of coefficients (Parks and Burrus, 1987).

Truncating the infinitely long operator with a window function such as

$$\tilde{W}(x-x', k(x), \Delta z) = \Omega(x-x')W(x-x', k(x), \Delta z), \quad (2.62)$$

where $\Omega(x-x')$ is a symmetric, compactly supported, spatial window localized near $x = x'$, usually results in an unstable approximation (Thorbecke et al., 2004; Margrave et al., 2006). For example, when Ω is a boxcar window, the actual spectrum will suffer from the *Gibbs phenomenon*. A boxcar window is a function that is zero until the start of the segment, one during the segment, and zero after the segment. Figure 2-3a shows the

amplitude of the finite-length operator, \tilde{W} , obtained using a boxcar window. Figures 2-3b and Figure 2-3c show the amplitude and phase of the actual spectrum, \hat{W} , where both have oscillations that are pronounced near the slope discontinuities.

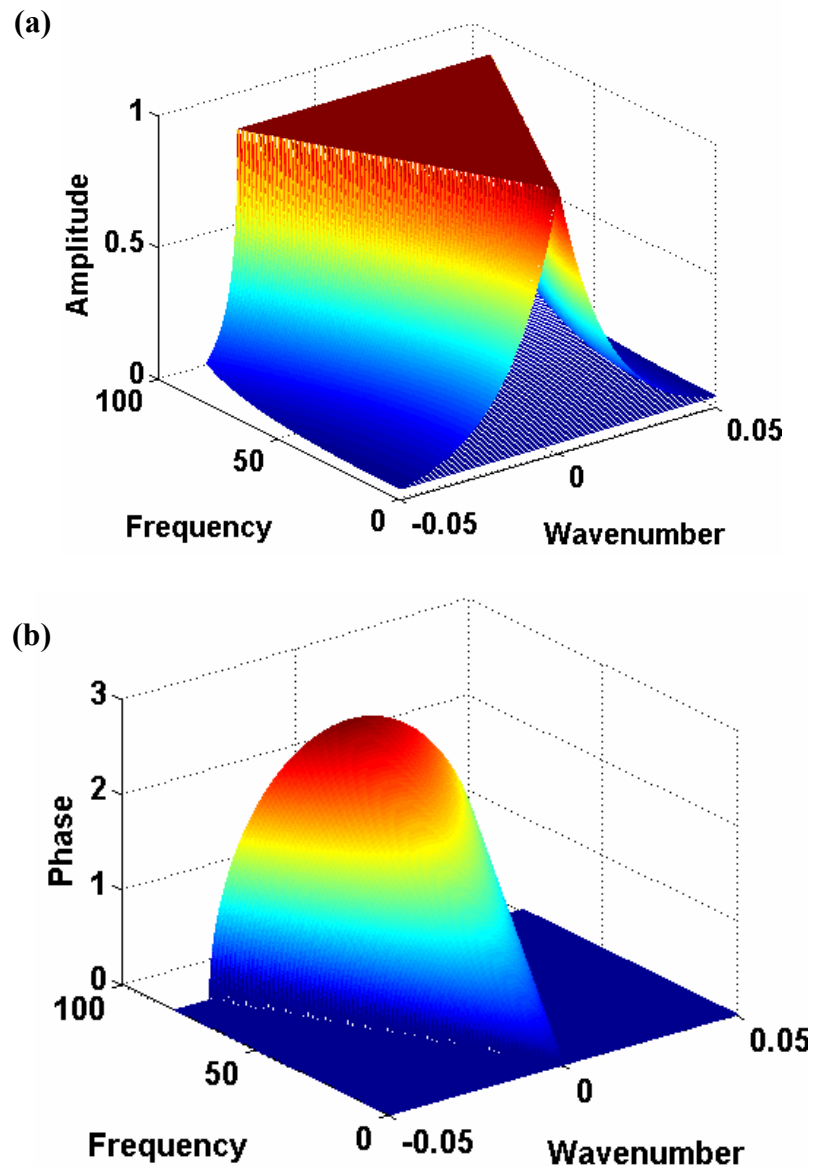


Figure 2-2. The (a) amplitude and (b) phase of the exact spectrum for $f=0-80$ Hz, where $\Delta x=10$ m, $\Delta z=10$ m, and $V=2000$ m/s.

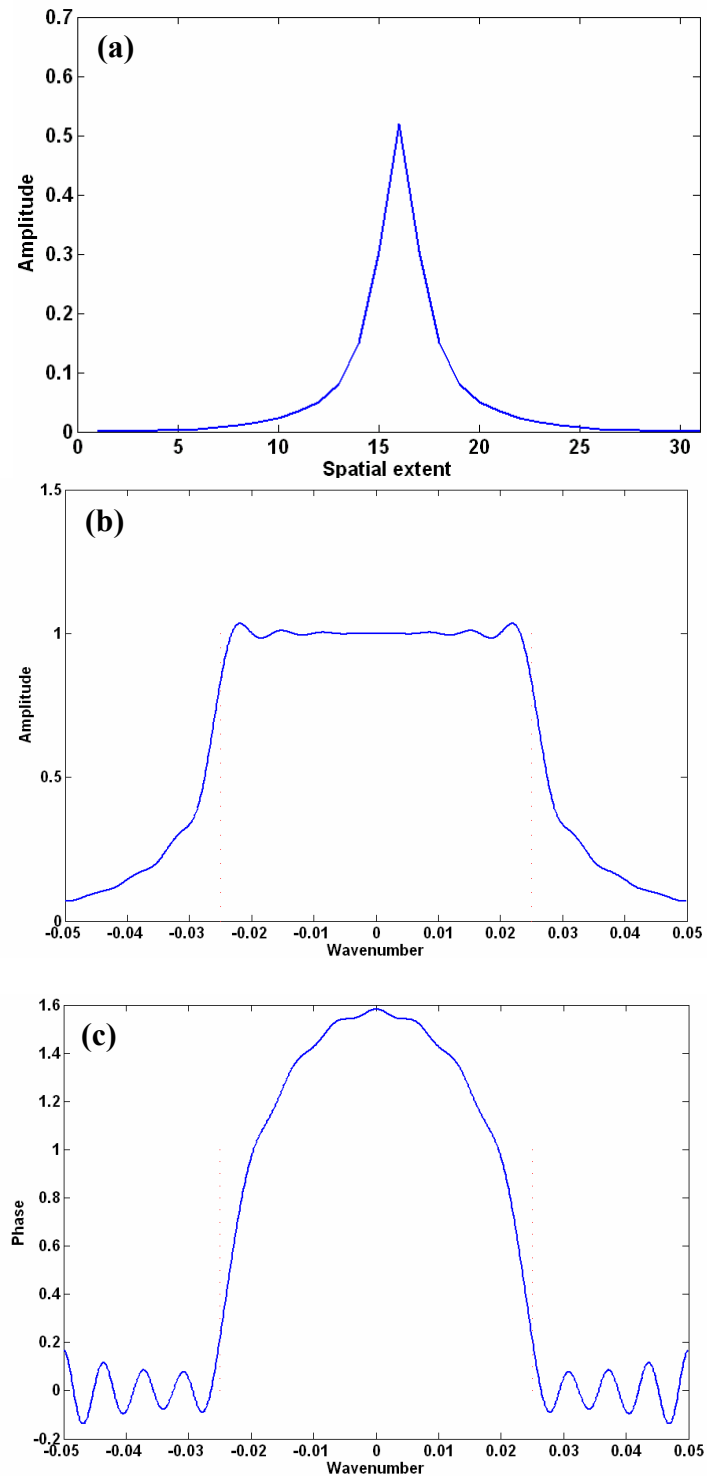


Figure 2-3. The (a) amplitude of a 31-point operator in the space-frequency domain obtained using a boxcar window, (b) amplitude of the actual spectrum, and (c) phase of the actual spectrum using the same parameters as Figure 2-1.

As its amplitude exceeds unity, repeated applications of this extrapolator in a recursive scheme will have a cumulative effect, generating amplitudes greater than one. Also, when Ω is a Hanning window, the actual spectrum will decay for some wavenumbers (Figure 2-4). So using simple window functions in the space-frequency domain to obtain a finite-length operator can either lead to unstable operators or operators that are suboptimal.

However, an operator that is mathematically unstable, as its amplitude exceeds unity, can be considered practically stable if its amplitude deviation from unity is very small.

Margrave et al. (2006) use a criterion to differentiate between mathematical and practical stabilities. That is, after m repeated applications of \tilde{W} in a recursive scheme in a homogeneous medium, the amplitude of its spectrum will be

$$\left| \hat{W} \right|^m \leq |1 + \varepsilon|^m \sim 1 + m\varepsilon, \quad (2.63)$$

where ε is the deviation from unity. The operator is mathematically, or perfectly stable, when $\varepsilon = 0$, and practically stable only if $m\varepsilon \ll 1$.

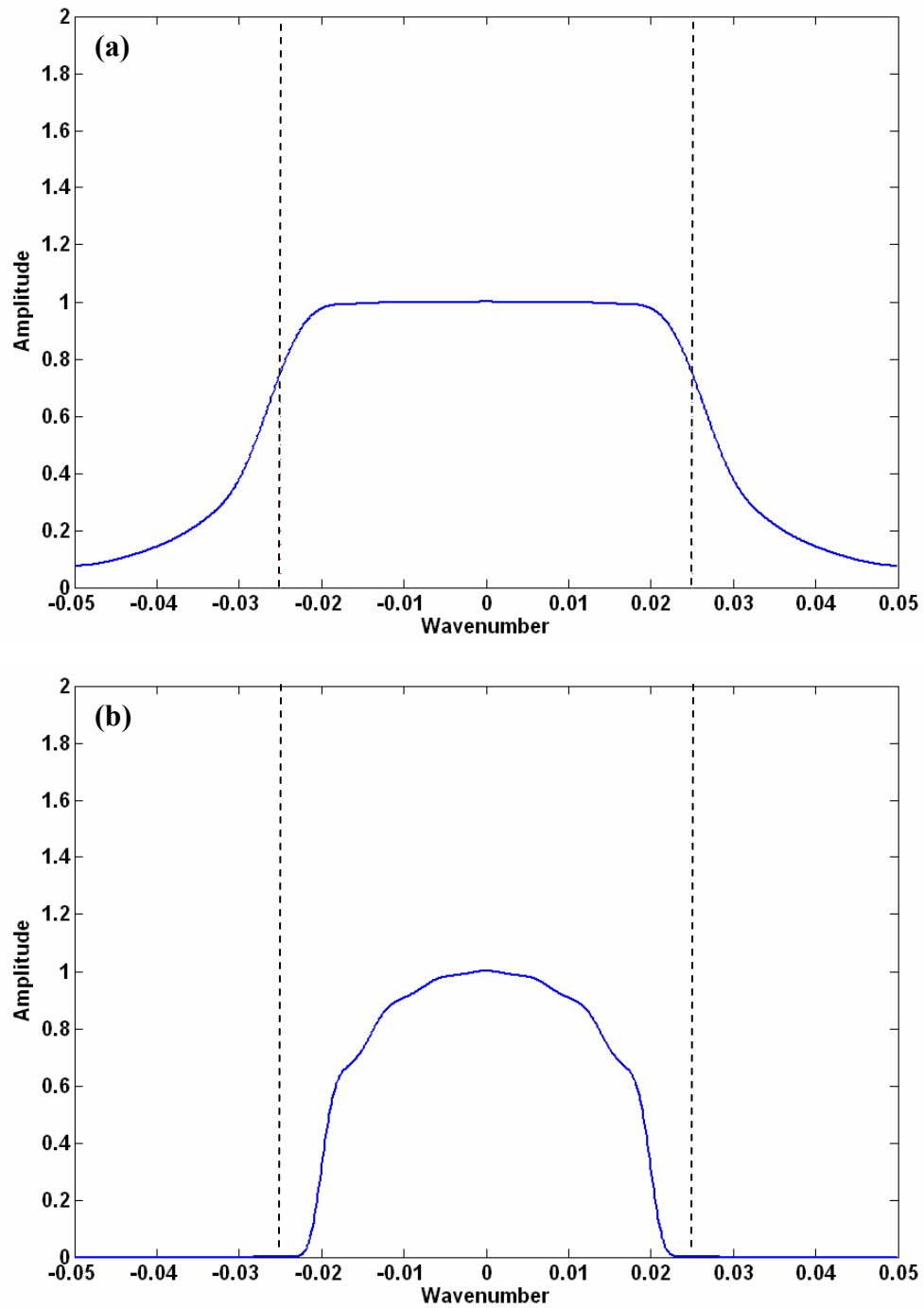


Figure 2-4. The (a) amplitude of the actual spectrum of a 31-point operator obtained by windowing the ideal operator with a Hanning window using the same parameters as Figure 2-1, and (b) the amplitude is raised to a power of 50 or $\left| \hat{\mathcal{W}} \right|^{50}$. The dashed lines indicate the evanescent boundaries. Note that amplitude is less than unity for most propagation angles.

2-5.2 Inherent instability

Designing a numerically stable operator is a challenging problem of explicit wavefield extrapolation methods. There is another type of instability, however, that might cause wavefield extrapolation methods to give unreasonable results. This type of instability is an inherent one, and is not restricted to the explicit methods, but is a general feature of phase-shift based algorithms such as PSPI and GPSPI.

Etgen (1994) has shown that phase-shift based algorithms are not unconditionally stable as previously claimed. In fact, for extreme lateral velocity variations, wavefield extrapolation methods can become unstable. Further, the symbol that is used in these methods is only the high frequency limit of the exact symbol. Fortunately, the amount of exponential growth present in most migrated sections due to this type of inherent instability is small, and in many cases exact treatment of amplitudes is not required (Etgen, 1994).

2-6 CHAPTER SUMMARY

Migration consists of two steps: wavefield extrapolation and imaging condition. In this chapter, different algorithms for extrapolating the wavefield into the subsurface have been reviewed, as well as different imaging conditions. These algorithms were phase-shift, phase-shift plus interpolation, generalized phase-shift plus interpolation, and the explicit wavefield extrapolation. The imaging conditions were the deconvolution and crosscorrelation imaging conditions. Also in this chapter, shot profile migration that

combines the wavefield extrapolation and imaging condition to obtain a prestack depth migration (PSDM) image of the subsurface was reviewed.

Phase-shift extrapolation can only handle vertical velocity variation. The phase-shift plus interpolation (PSPI) algorithm can handle weak lateral velocity variations, the generalized phase-shift plus interpolation (GPSPI) can handle strong lateral velocity variations, and the space-frequency wavefield extrapolation is a useful approximation to GPSPI. Space-frequency extrapolation is attractive because it is computationally more efficient than the GPSPI algorithm, provided the nonstationary convolution operator is practically stable. Designing practical stable operators is a challenging problem for explicit wavefield extrapolation methods. In the next chapter, different advanced methods for designing practically stable operators will be reviewed.

CHAPTER 3: COMPARISONS OF THE HALE, SOUBARAS, WLSQ, AND FOCI WAVEFIELD EXTRAPOLATORS

The techniques developed by Hale (1991), Soubaras (1996), Thorbecke et al. (2004), and Margrave et al. (2006) for designing wavefield extrapolators are derived and compared in this chapter. The purpose of this derivation is to put the various extrapolators in the same context to ease understanding them. Further, comparing them using the same parameters gives us an idea about the weaknesses and strengths of each one.

The amplitude and phase spectra, impulse responses, and prestack implementations of these extrapolators will be used to analyze their stability, accuracy, ability to handle high angles of propagation, and efficiency.

3-1 HALE'S EXTRAPOLATOR

The following development is based on Hale (1991) and reproduced here for completeness and clarity⁴. Let's start with the phase-shift operator, the exact spectrum, in a 2D setting

$$\hat{W}(k_x, k, \Delta z) = \exp(ik_z \Delta z), \quad (3.1)$$

where

⁴ This derivation is similar to Hale (1991) but uses different symbols.

$$k_z = \begin{cases} \sqrt{k^2 - k_x^2}; & |k| > |k_x| \\ i\sqrt{k_x^2 - k^2}; & |k| < |k_x| \end{cases}, \quad (3.2)$$

and

$$k = \frac{\omega}{V}. \quad (3.3)$$

For formal definitions of these terms refer to section 2-1. Equation (3.1) can be rewritten as

$$\hat{W}(\bar{k}_x, k, \Delta z) = \exp\left(i\left(\frac{\Delta z}{\Delta x}\right)\sqrt{(k\Delta x)^2 - \bar{k}_x^2}\right), \quad (3.4)$$

where $\bar{k}_x = k_x \Delta x$ (using Hale's notation) is the normalized transverse number and Δx is the space sample interval. The spectrum, $\hat{W}(\bar{k}_x, k, \Delta z)$, can be uniquely determined by $\Delta z / \Delta x$ and $k\Delta x$. The exact spectrum is symmetric with respect to the normalized transverse wavenumber, \bar{k}_x , which implies that the approximated operator in the space-frequency domain, \tilde{W} , is also even

$$\tilde{W}(-n\Delta x, k, \Delta z) = \tilde{W}(n\Delta x, k, \Delta z), \quad (3.5)$$

where n is the coefficient index bounded by $-(N-1)/2 \leq n \leq (N-1)/2$, and N is the number of operator coefficients. The actual spectrum of the approximated operator, \tilde{W} , can be defined as

$$\hat{\tilde{W}}(\bar{k}_x, k, \Delta z) = \sum_{n=-(N-1)/2}^{(N-1)/2} \tilde{W}(n\Delta x, k, \Delta z) \exp(-i\bar{k}_x n), \quad (3.6)$$

where the discrete Fourier transformation was used. For a symmetric operator, \tilde{W} , equation (3.6) reduces to

$$\hat{W}(\bar{k}_x, k, \Delta z) = \sum_{n=0}^{(N-1)/2} (2 - \delta_{n0}) \tilde{W}(n\Delta x, k, \Delta z) \cos(\bar{k}_x n), \quad (3.7)$$

where δ_{n0} is the Kronecker delta function defined as

$$\delta_{n0} = \begin{cases} 1; & n = 0 \\ 0; & n \neq 0 \end{cases}, \quad (3.8)$$

(see Appendix A). In Hale's method, the coefficients of \tilde{W} can be represented as a sum of \mathbf{M} weighted basis functions:

$$\tilde{W}(n\Delta x, k, \Delta z) = \sum_{m=0}^{\mathbf{M}-1} c_m B_{mn}, \quad (3.9)$$

where Hale's choice for basis functions is

$$B_{mn} = (2 - \delta_{m0}) \cos\left(\frac{2\pi mn}{N}\right), \quad (3.10)$$

and to ensure stability

$$\mathbf{M} < \frac{N+1}{2}. \quad (3.11)$$

That is, only \mathbf{M} basis functions are used, and the remaining $[(N+1)/2 - \mathbf{M}]$ degrees of freedom are used to ensure stability. The weights, c_m , are determined by matching \mathbf{M} even derivatives, for $l = 0, 1, 2, \dots, \mathbf{M}-1$, evaluated at $\bar{k}_x = 0$, which gives a system of linear equations

$$\sum_{m=0}^{\mathbf{M}-1} c_m \left[\hat{B}_m^{(2l)} \right]_{\bar{k}_x=0} = \left[\hat{W}^{(2l)} \right]_{\bar{k}_x=0}, \quad (3.12)$$

where \hat{B}_m is the spectrum of the cosine basis function defined as

$$\hat{B}_m = \sum_{n=0}^{(N-1)/2} (2 - \delta_{n0}) B_{mn} \cos(\bar{k}_x n). \quad (3.13)$$

Once these weights are determined, they can be used in equation (3.9) to obtain Hale's extrapolator.

3-1.1 Stabilizing Hale's extrapolator

To implement and investigate Hale's method, a subroutine was written to design an extrapolator for a given spatial length, frequency, and velocity using the symbolic toolbox in MATLAB. The symbolic toolbox is needed to take the even derivatives of the exact spectrum (equation (3.12)), then evaluate these derivatives at $\bar{k}_x = 0$. As a calibration test for the subroutine, some of the key figures in Hale's paper were reproduced with the same parameters. Figure 3-1 shows the amplitudes of the exact spectrum and the actual spectrum of Hale's extrapolator.

There is no direct formula for choosing the optimum **M** value that ensures stability. Further, choosing a constant **M** value for all frequencies will cause operators corresponding to some frequencies to be unstable (Figure 3-2). To make this extrapolator stable for all frequencies of interest, they should have different **M** values. By breaking the frequencies into partitions and assigning a different **M** for each partition, stability can be ensured for all frequencies⁵.

⁵ Hale (1991) did not show how to ensure stability for all normalized frequencies. One way to achieve that is by assigning a different **M** value for each frequency range.

In general, higher frequencies will be assigned larger \mathbf{M} values than the low ones. Figure 3-3 shows that when varying the \mathbf{M} value with the frequencies, the operator exhibits stability for all frequencies.

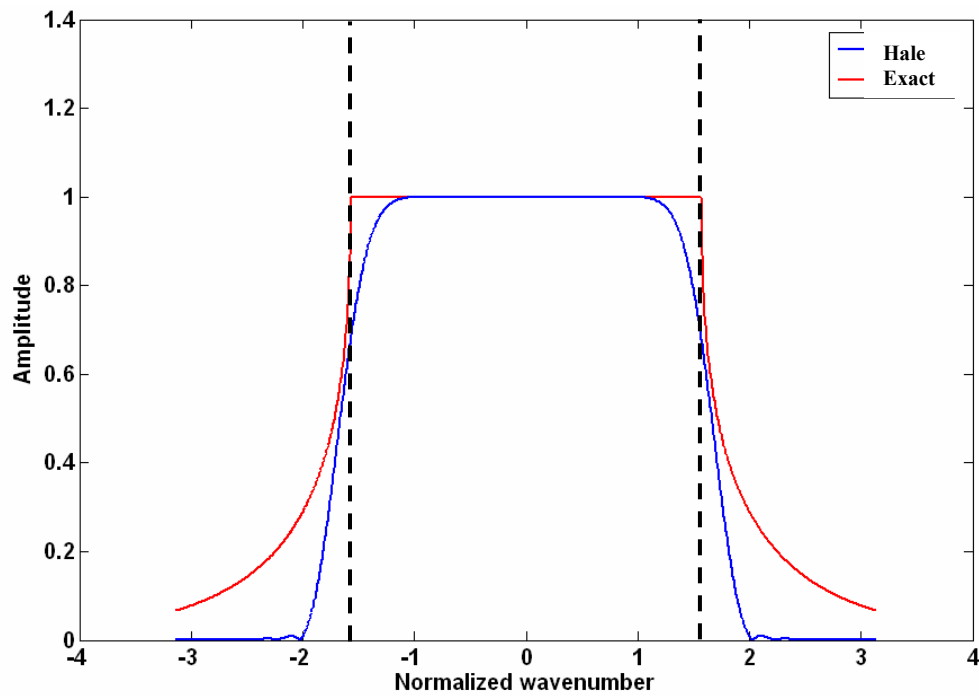


Figure 3-1. Amplitudes of the exact and actual spectra using $\omega\Delta x/V = \pi/2$, $\Delta x = \Delta z = 10$ m, and $N = 31$. The dashed lines define the evanescent boundaries.

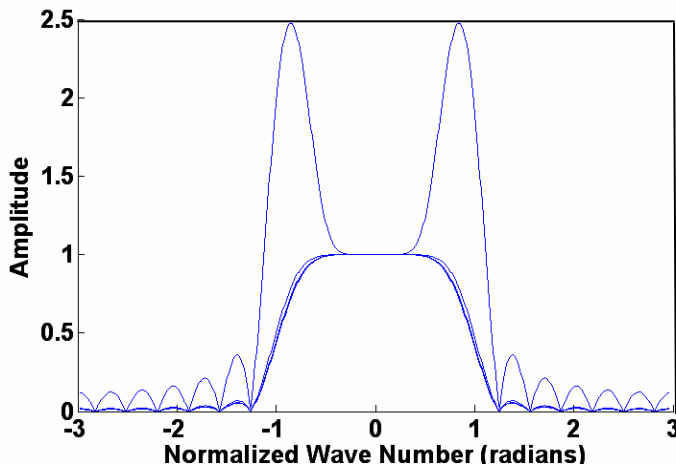


Figure 3-2. Amplitudes of the actual spectrum for different frequencies with a constant $M=5$. The frequency range is 10-100 Hz in increments of 10 Hz, $V=2000$ m/s, $\Delta x=10$ m, $\Delta z=10$ m, and $N=19$.

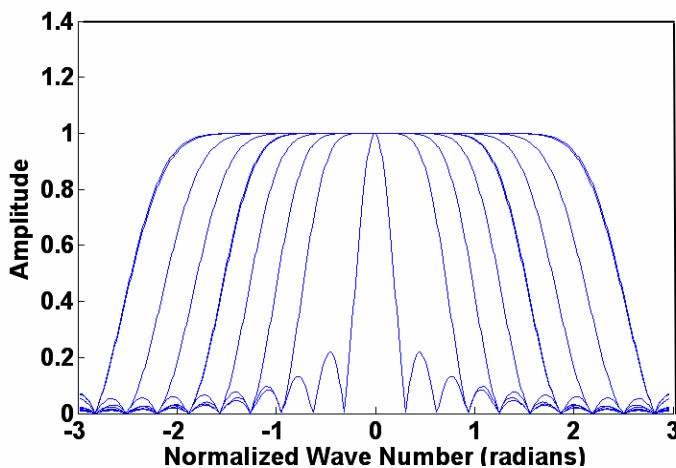


Figure 3-3. Amplitudes of the actual spectrum for different frequencies after varying the value of M . The frequency range is 10-100 Hz in increments of 10 Hz, $V=2000$ m/s, $\Delta x=10$ m, $\Delta z=10$ m, the range of M is 1-8, and $N=19$.

3-2 THEORY OF THE SOUBARAS EXTRAPOLATOR

Soubaras (1996) uses the Remez Exchange algorithm (McClellan and Parks, 1972) to design practically stable operators by first decomposing the exact spectrum,

$$\hat{W}(k_x, k, \Delta z) = \exp(ik_z \Delta z), \quad (3.14)$$

into real and imaginary parts as in

$$\hat{W}(k_x, k, \Delta z) = \hat{W}_r(k_x, k, \Delta z) + i\hat{W}_i(k_x, k, \Delta z), \quad (3.15)$$

where

$$\hat{W}_r(k_x, k, \Delta z) = \cos(k_z \Delta z) \quad (3.16)$$

and

$$\hat{W}_i(k_x, k, \Delta z) = \sin(k_z \Delta z). \quad (3.17)$$

Then the Remez exchange algorithm is used to solve the following problem: given ideal real symmetrical spectra $\hat{W}_r(k_x, k, \Delta z)$ and $\hat{W}_i(k_x, k, \Delta z)$, and a positive weighting function $\Upsilon(k_x)$, find $\hat{\tilde{W}}_r(k_x, k, \Delta z)$ and $\hat{\tilde{W}}_i(k_x, k, \Delta z)$, such that the maximum error functions $\|E_r\|_\infty$ and $\|E_i\|_\infty$ are minimized, where

$$\|E_r\|_\infty = \max |E_r(k_x, k, \Delta z)|, \quad k_x \in [0, k_N] \quad (3.18)$$

and

$$\|E_i\|_\infty = \max |E_i(k_x, k, \Delta z)|, \quad k_x \in [0, k_N], \quad (3.19)$$

where $\| \cdot \|_\infty$ is the L_∞ norm, $| \cdot |$ is the L_1 norm, and $k_N = \pi / \Delta x$ is the Nyquist

wavenumber. The error functions can be defined as

$$E_r(k_x) = \Upsilon(k_x) \left(\hat{W}_r(k_x, k, \Delta z) - \hat{\tilde{W}}_r(k_x, k, \Delta z) \right) \quad (3.20)$$

and

$$E_i(k_x) = \Upsilon(k_x) \left(\hat{W}_i(k_x, k, \Delta z) - \hat{\tilde{W}}_i(k_x, k, \Delta z) \right). \quad (3.21)$$

The weighting function can be defined as

$$\Upsilon(k_x) = \begin{cases} 1; & |k_x| < k_\alpha \\ \varepsilon; & |k_x| > k_\alpha \end{cases}, \quad (3.22)$$

where $\varepsilon \ll 1$, $k_\alpha = |k| \sin \alpha$, and α determines the maximum angle of propagation⁶. The actual spectra can be defined as (see Appendix B)

$$\hat{\tilde{W}}_r(k_x, k, \Delta z) = \sum_{m=0}^M (2 - \delta_{m0}) \tilde{W}_r(m\Delta x, k, \Delta z) \cos(k_x m\Delta x) \quad (3.23)$$

and

$$\hat{\tilde{W}}_i(k_x, k, \Delta z) = \sum_{m=0}^M (2 - \delta_{m0}) \tilde{W}_i(m\Delta x, k, \Delta z) \cos(k_x m\Delta x), \quad (3.24)$$

where $M = (N - 1)/2$ and δ_{m0} was defined in equation (3.8). The Soubaras extrapolator can be assembled according to

$$\tilde{W}(x, k, \Delta z) = \tilde{W}_r(x, k, \Delta z) + i\tilde{W}_i(x, k, \Delta z). \quad (3.25)$$

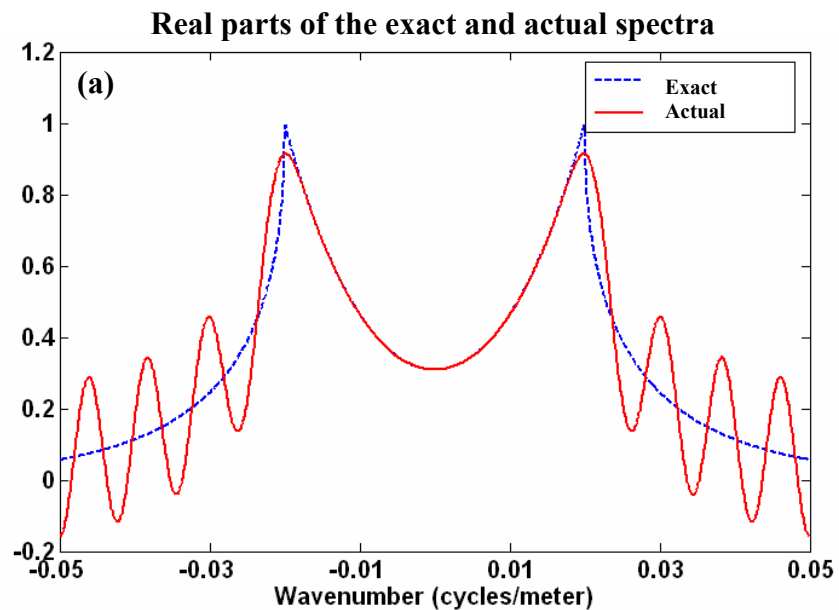
In this method, the coefficients of $\tilde{W}_r(x, k, \Delta z)$ and $\tilde{W}_i(x, k, \Delta z)$ are found such that their

spectra, $\hat{\tilde{W}}_r(x, k, \Delta z)$ and $\hat{\tilde{W}}_i(x, k, \Delta z)$, are the minimax approximations of $\hat{W}_r(x, k, \Delta z)$

⁶ α is a user-defined parameter.

and $\hat{W}_i(x, k, \Delta z)$ (see Appendix C for more details), where minimax means that the maximum error is minimized.

Figure 3-4a shows the real parts of the exact and actual spectra, Figure 3-4b shows the imaginary parts of the exact and actual spectra, and Figure 3-4c shows the amplitudes of the exact and the actual spectra using $\Delta x = 10$ m, $\Delta z = 10$ m, $V = 2000$ m/s, and $f = 40$ Hz. These figures show that the Remez exchange algorithm can be used to design operators that are practically stable (Soubaras, 1996). However, the weight function, Υ , that is used to stabilize the operator design, depends on the parameters. The same weight function is not guaranteed to give the same results for every combination of parameters⁷.



⁷ That is, operators corresponding to different frequencies may require different weight values.

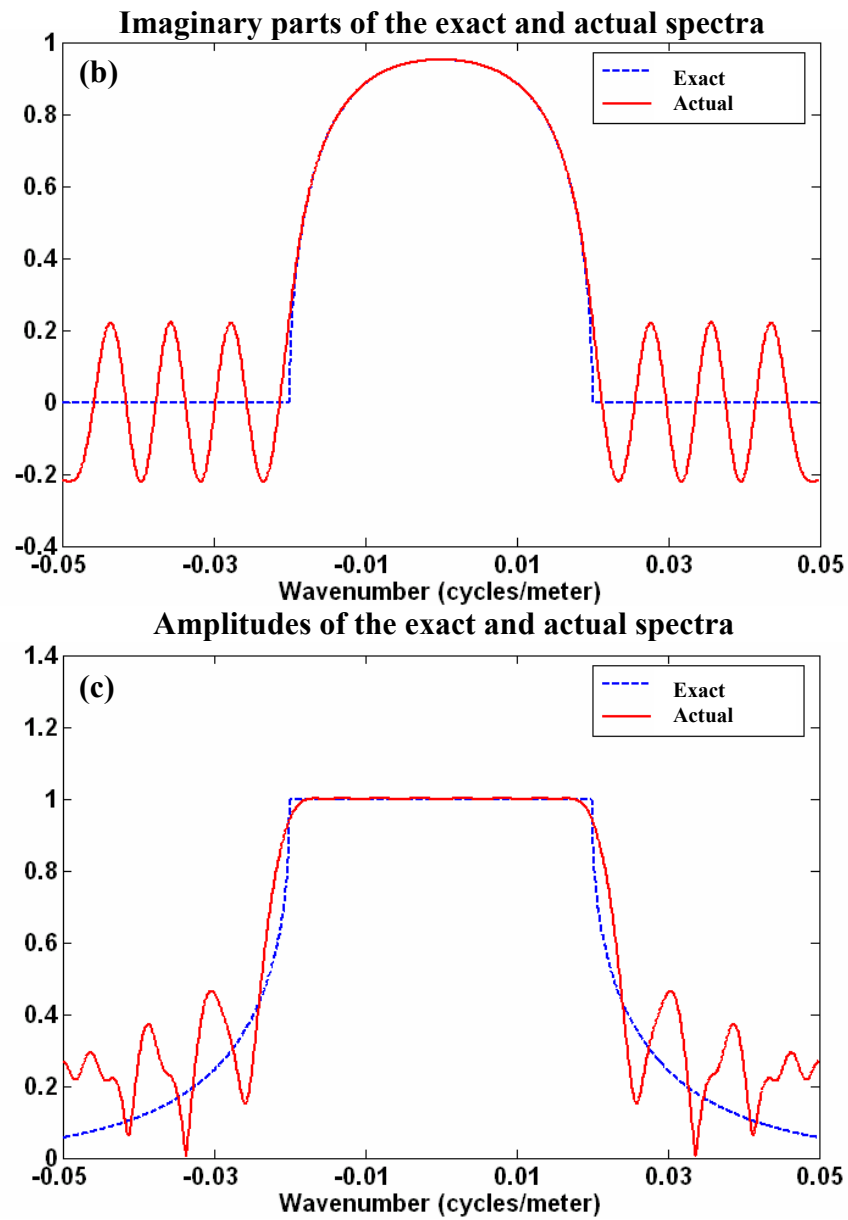


Figure 3-4. Comparisons of the exact and actual spectra, where (a) shows the real parts of the spectra, (b) shows the imaginary parts of the spectra, and (c) shows the amplitudes of the spectra, using $\alpha = 75^\circ$, $\Delta x = 10$, $\Delta z = 10$ m, and $N = 31$.

3-3 THE WLSQ EXTRAPOLATOR

Following the derivation of Thorbecke et al. (2004), the spectrum of a compactly supported operator, $\tilde{W}(x, k, \Delta z)$, can be written (using the discrete Fourier transformation) as

$$\hat{\tilde{W}}(m\Delta k_x, k, \Delta z) = \Delta x \sum_{n=-(N-1)/2}^{(N-1)/2} \tilde{W}(n\Delta x, k, \Delta z) \exp(im\Delta k_x n\Delta x), \quad (3.26)$$

where

$$-(M-1)/2 \leq m \leq (M-1)/2, \quad (3.27)$$

$$\Delta k_x > 2\pi/(N\Delta x), \quad (3.28)$$

$$k_x = m\Delta k_x, \quad (3.29)$$

and

$$x = n\Delta x. \quad (3.30)$$

M is the number of samples of the transverse wavenumber, and N is the number of operator coefficients. Rewriting equation (3.26) in matrix notation gives

$$\hat{\underline{\tilde{W}}} = \underline{\underline{F}} \underline{\tilde{W}}, \quad (3.31)$$

where “ $\underline{\quad}$ ” indicates a vector and “ $\underline{\underline{\quad}}$ ” indicates a matrix. To obtain a least-squares solution, there should be more equations than unknowns, that is, $M > N$. The weighted least-squares solution of equation (3.31) is given by

$$\underline{\tilde{W}} = \left[\underline{\underline{F}}^H \underline{\underline{\Upsilon}} \underline{\underline{F}} \right]^{-1} \underline{\underline{F}}^H \underline{\underline{\Upsilon}} \hat{\underline{\tilde{W}}}, \quad (3.32)$$

where $\underline{\tilde{W}}$ is an $N \times 1$ vector, $\underline{\underline{F}}$ is an $M \times N$ matrix, $\underline{\underline{\Upsilon}}$ is an $M \times M$ diagonal matrix, $\underline{\hat{W}}$ is an $M \times 1$ vector, and the superscript H denotes the complex-conjugate transpose. The components of the Fourier transformation matrix, $\underline{\underline{F}}$, are given by

$$F_{mn} = \exp(im\Delta k_x n\Delta x). \quad (3.33)$$

Also, the components of the diagonal matrix $\underline{\underline{\Upsilon}}$ are defined as

$$\Upsilon_{mn} = \Lambda(m\Delta k_x) \delta_{mn}, \quad (3.34)$$

where $\underline{\Lambda}$ is a $1 \times M$ box-shaped weighting vector defined as

$$\Lambda(m\Delta k_x) = \begin{cases} 1; & |m\Delta k_x| \leq k_\alpha \\ \varepsilon; & |m\Delta k_x| > k_\alpha \end{cases}, \quad (3.35)$$

where $0 < \varepsilon \ll 1$, and the transverse wavenumber, k_α , corresponding to the maximum propagation angle of interest, α , can be defined as

$$k_\alpha = |k| \sin \alpha, \quad (3.36)$$

and δ is the Kronecker delta function defined as

$$\delta_{mn} = \begin{cases} 1; & m = n \\ 0; & m \neq n \end{cases}. \quad (3.37)$$

Thorbecke et al. (2004) use weighted least-squares with a transition function to design the extrapolator. That is, instead of using the exact spectrum, $\underline{\hat{W}}$, a model-based function, $\underline{\hat{W}}_D$, is used

$$\underline{\tilde{W}} = \left[\underline{\underline{F}}^H \underline{\underline{\Upsilon}} \underline{\underline{F}} \right]^{-1} \underline{\underline{F}}^H \underline{\underline{\Upsilon}} \underline{\hat{W}}_D. \quad (3.38)$$

The desired spectrum only approximates the exact spectrum in the wavelike region, and its amplitude and phase spectra can be defined as follows

$$\left\| \hat{W}_D(k_x, k_\alpha, \Delta z) \right\| = \begin{cases} 1.0; & |k_x| \leq k_\alpha \\ \text{spline}; & k_\alpha < |k_x| < \frac{\pi}{\Delta x} \\ 0.0; & |k_x| = \frac{\pi}{\Delta x} \end{cases} \quad (3.39)$$

and

$$\arg(\hat{W}_D(k_x, k_\alpha, \Delta z)) = \begin{cases} k_z \Delta z; & |k_x| \leq k_\alpha \\ \text{spline}; & k_\alpha < |k_x| < \frac{\pi}{\Delta x} \\ 0.0; & |k_x| = \frac{\pi}{\Delta x} \end{cases} . \quad (3.40)$$

The only difference between equations (3.38) and (3.32) is that they use different desired spectra. Figure 3-5a shows the amplitudes of the exact and desired spectra, and Figure 3-5b shows their phases. Note that the amplitude and phase of the desired spectrum do not have the sharp slope discontinuities that are present in the exact spectrum. Figure 3-6a shows the amplitudes of the exact spectrum and the actual spectrum of the WLSQ extrapolator, and Figure 3-6b shows their phases. These figures show that the WLSQ approach can be used to design practically stable operators.

Thorbecke et al. (2004) refer to this approach as the modified weighted least-squares approach. The weighted least-squares approach, however, was first introduced by

Thorbecke and Rietveld (1994), where the exact spectrum was used in equation (3.32) as the desired spectrum. Their first approach did not generate very stable operators (Thorbecke et al., 2004). In contrast, when a model-based function is used as the desired spectrum, it yields much more stable operators.

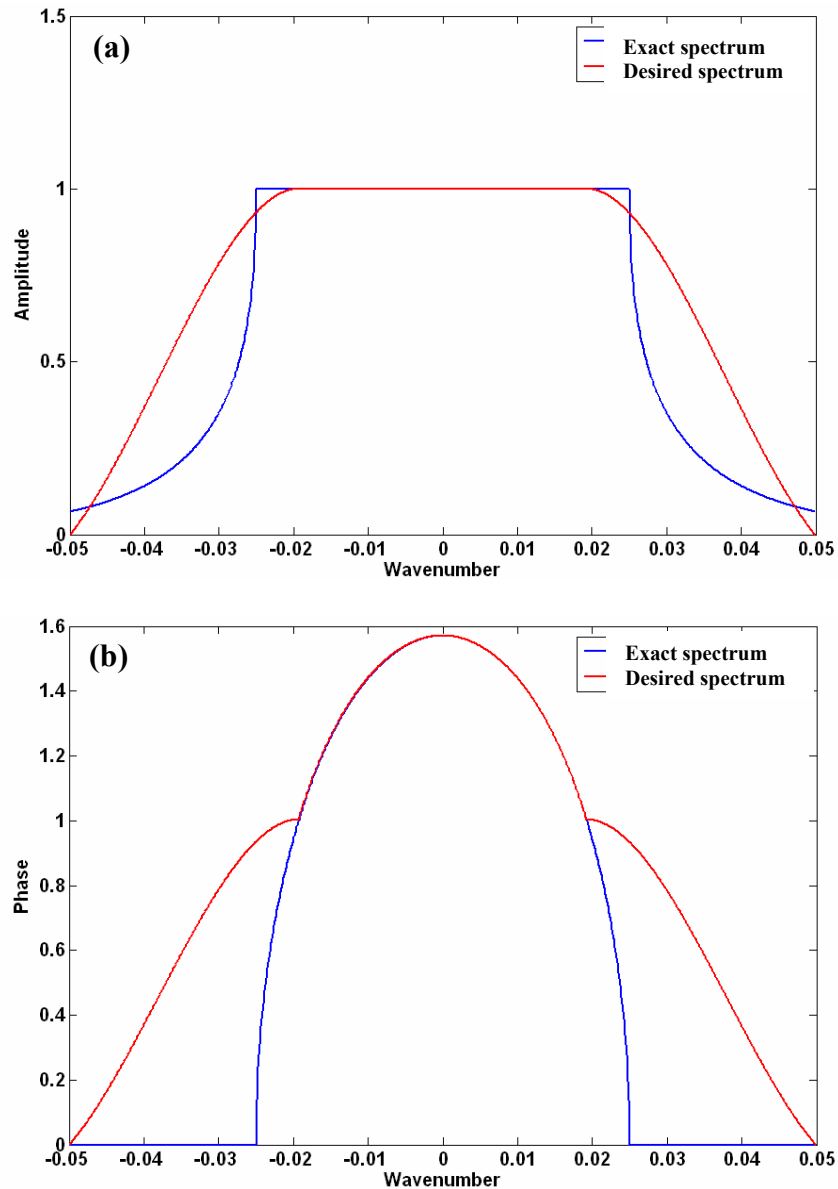


Figure 3-5. (a) Amplitudes and (b) phases of the exact and desired spectra, where $\alpha = 75^\circ$, $\Delta x = 10$, $\Delta z = 10$ m, $f = 50$ Hz, and $\varepsilon = 0.0001$.

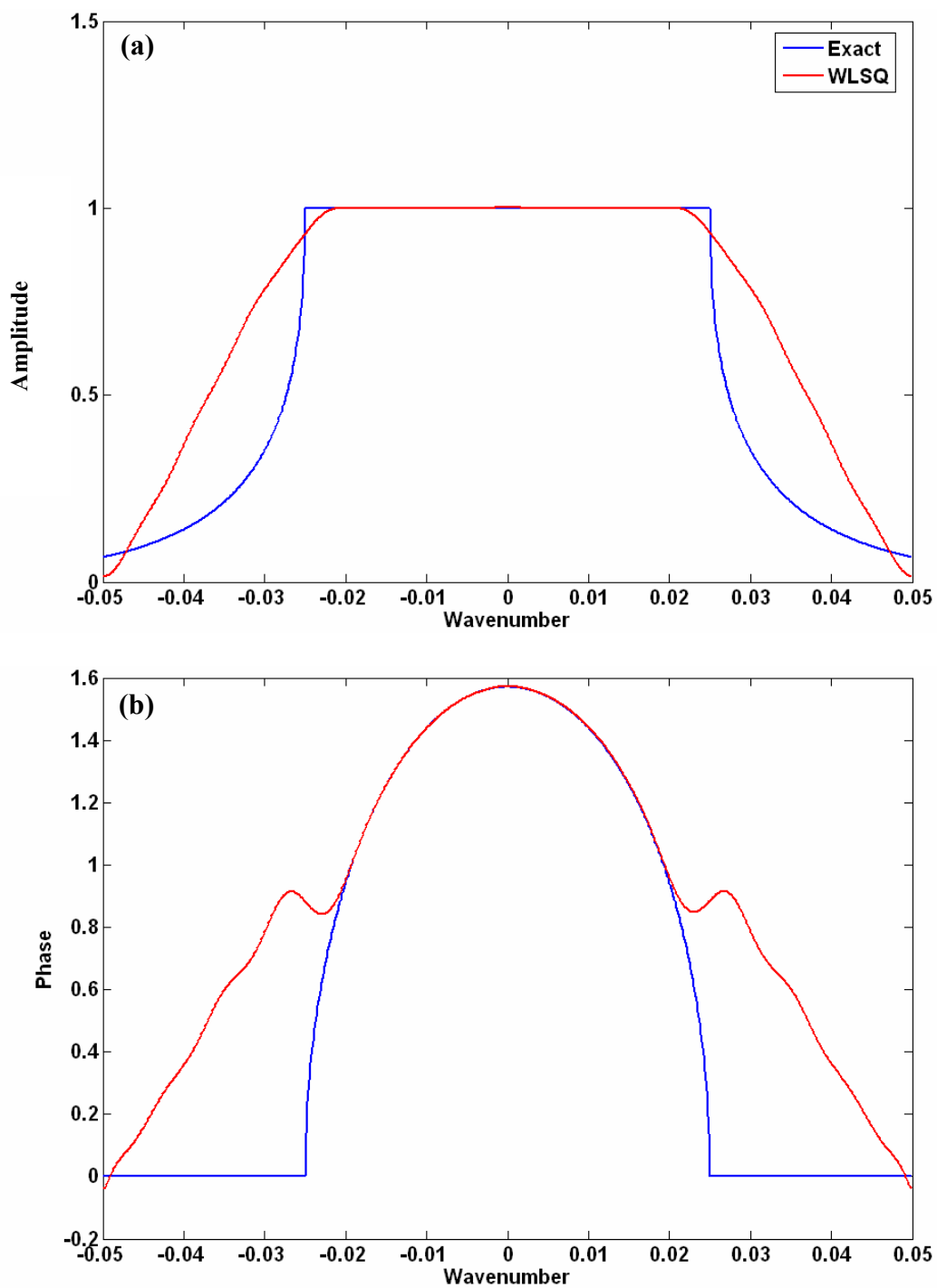


Figure 3-6. (a) Amplitudes and (b) phases of the exact spectrum and actual spectrum of WLSQ, where $N=31$, $\alpha = 75^\circ$, $\Delta x=10$, $\Delta z=10$ m, $f=50$ Hz, and $\varepsilon=0.0001$.

3-4 THE FOCI EXTRAPOLATOR

Based on the derivation of Margrave et al. (2006), the forward operator and conjugate inverse (FOCI) method uses the following two useful properties:

- The product of two spectra, in the wavenumber-frequency domain for a half depth step, gives the spectrum for the full depth step

$$\hat{W}(k_x, k, \Delta z) = \hat{W}(k_x, k, \Delta z / 2) \hat{W}(k_x, k, \Delta z / 2). \quad (3.41)$$

- The inverse of a spectrum equals its conjugate in the wavelike region

$$\hat{W}^{-1}(k_x, k, \Delta z / 2) = \hat{W}^*(k_x, k, \Delta z / 2), \quad |k_x| < |k|. \quad (3.42)$$

In this method, two operators are needed: a forward operator, \tilde{W}_{for} , for a half depth step obtained as

$$\tilde{W}_{for}(x, k, \Delta z / 2) = \Omega(x) W(x, k, \Delta z / 2), \quad (3.43)$$

and an inverse operator, \tilde{W}_{inv} , obtained by solving the following equation in least-squares sense

$$\tilde{W}_{inv}(x, k, \Delta z / 2) \bullet \tilde{W}_{for}(x, k, \Delta z / 2) = \frac{1}{2\pi} \int_{\mathbb{R}} \left[\left| \hat{W}(k_x, k, \Delta z / 2) \right|^\eta \right] \exp(-ik_x x) dk_x, \quad (3.44)$$

where W is the ideal, infinitely long, extrapolator (section 2-4), Ω is a symmetric

Hanning window whose length equals the length of the forward operator, n_{for} . The

length of \tilde{W}_{inv} is n_{inv} , \bullet indicates spatial convolution, and $\eta \geq 0$ is an adjustable

parameter such that when $\eta = 0$, then \tilde{W}_{inv} is an exact inverse, and a bandlimited inverse

otherwise. The FOCI operator can then be assembled by convolving the forward operator with the conjugate of the inverse operator according to

$$\tilde{W}(x, k, \Delta z) = \tilde{W}_{for}(x, k, \Delta z / 2) \bullet \tilde{W}_{inv}^*(x, k, \Delta z / 2). \quad (3.45)$$

The FOCI operator is compactly supported because both the forward and inverse operators are compactly supported by design. The length of the FOCI operator is $n_{for} + n_{inv} - 1$. The phase accuracy of \tilde{W} , however, is limited by the initial estimate of the forward operator for a half step. That is, the inverse operator can, at best, negate the phase of the forward operator. In other words, for $n_{inv} > n_{for}$, the phase of \tilde{W} will be, at best, as accurate as double the phase of \tilde{W}_{for} .

The parameter η in equation (3.44) controls the degree of evanescent filtering in the final composite operator, \tilde{W} . For $\eta = 0$, the resulting operator is mathematically stable but with no evanescent filtering. On the other hand, when $\eta = 2$, the resulting operator is practically unstable but has strong evanescent filtering.

Further, a post-design shorter operator can be obtained by multiplying the final operator with a Hanning window as in

$$\tilde{W}_{win}(x, k, \Delta z) = \Omega(x) \tilde{W}(x, k, \Delta z), \quad (3.46)$$

where the length of the post-design operator and the Hanning window is n_{win} . The instability induced by the operator defined by equation (3.46) should be less than the

instability of the forward because the spectrum of the FOCI operator, \hat{W} , should have the slope discontinuities smoothed, unlike the exact spectrum, \hat{W} .

3-4.1 Dual operator tables for increased instability

Figure 3-7 shows the amplitude and phase of the exact and FOCI spectra, calculated with $\eta = 1$. The amplitude of the spectrum of FOCI, in Figure 3-7a, is not practically stable. In fact, repeated applications of this operator in a recursive scheme will amplify the wavefield dramatically. Notwithstanding its instability, it has relatively strong evanescent filtering. Figure 3-8 shows the amplitude and phase of the exact and FOCI spectra, calculated with $\eta = 0.01$. It is practically stable but with weak evanescent filtering. Using this operator in a recursive scheme will not mute the evanescent energy as it should.

The FOCI algorithm assumes that evanescent filtering is not needed at every depth step. As a result, dual operator tables can be used in depth migration where the first table is used for evanescent filtering applied every j^{th} step, and the other is used for most of the extrapolation steps. The first table can be calculated using a large value of η such as 1.0, and the other one can be calculated using a smaller value of η such as 0.01.

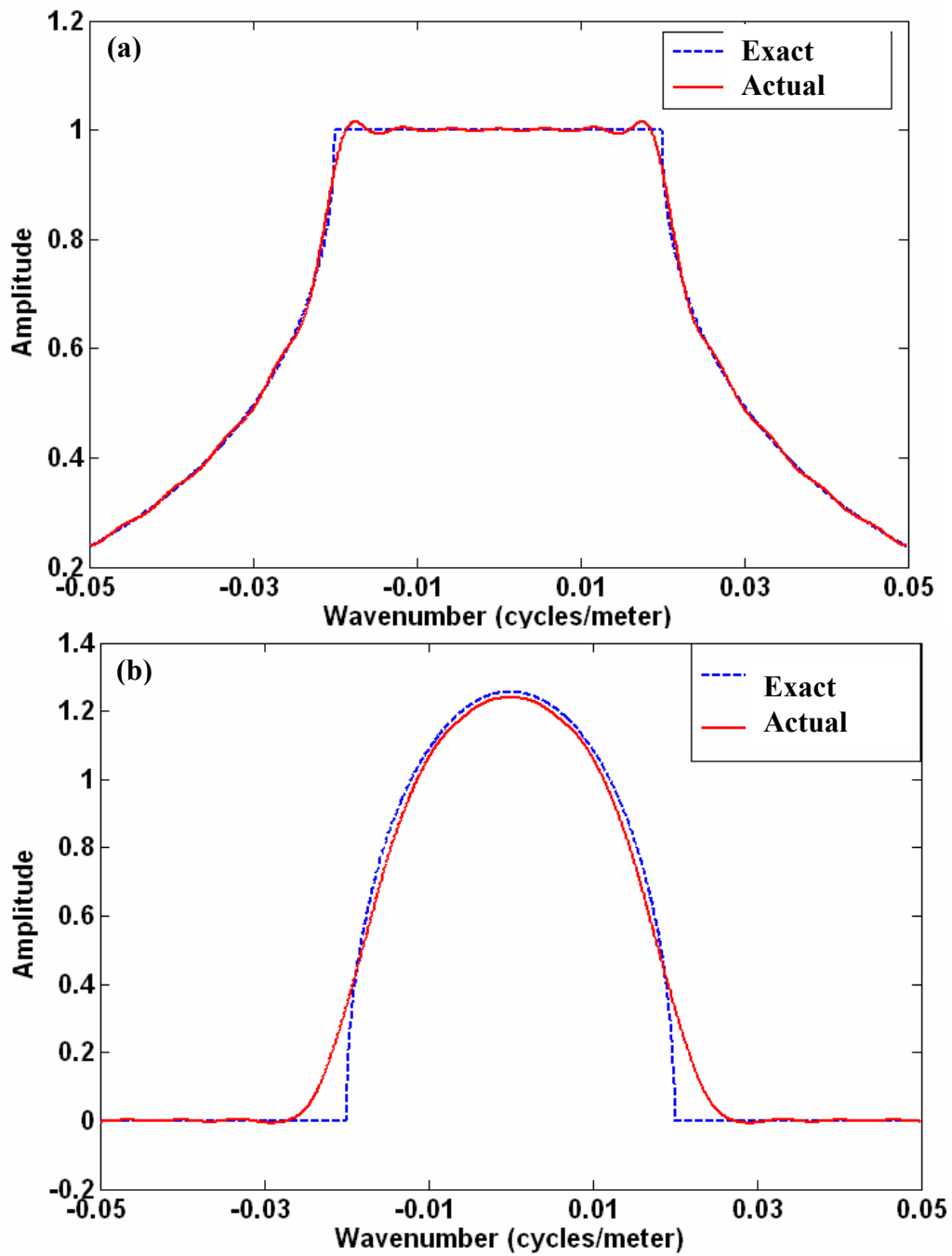


Figure 3-7. The (a) amplitudes and (b) phases of the exact and FOCI spectra, where $\eta=1$, $n_{for}=21$, $n_{inv}=31$, and $f=40$ Hz.

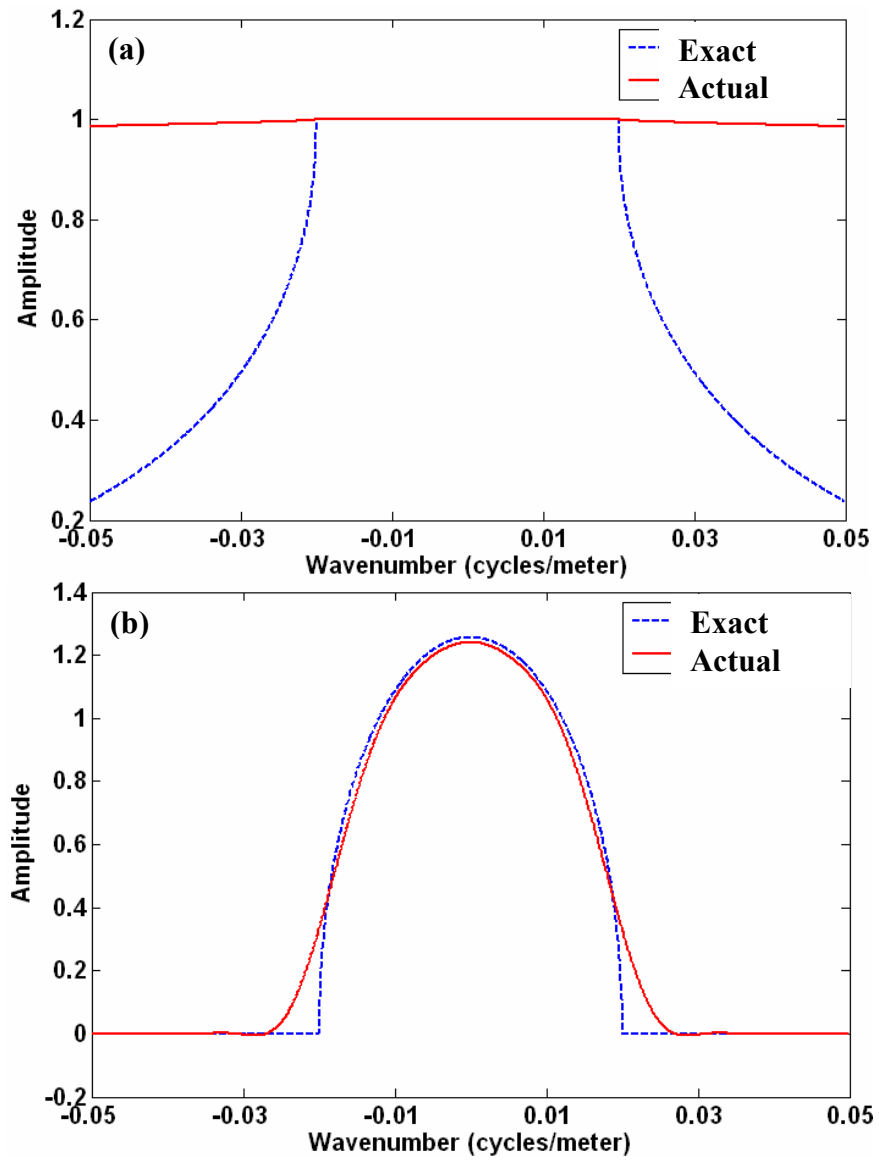


Figure 3-8. The (a) amplitudes and (b) phases of the exact and FOCI spectra, where $\eta=0.01$, $n_{for}=21$, $n_{inv}=31$, and $f=40$ Hz.

3-4.2 Spatial resampling

Besides the use of dual tables, the FOCI algorithm spatially down-samples the lower frequencies to increase operator accuracy and decrease run times. The spectra of operators corresponding to low frequencies, high velocities, or both, usually have few control points in the wavelike region. This means that such operators have poor amplitude and phase control for propagating waves. Spatial resampling can be used to overcome these problems by dividing the data into frequency partitions during the extrapolation process, extrapolate each partition, where each will have a different spatial sampling depending on the frequency content, then resample the data back to the original spatial sampling rate.

The following development of spatial resampling is due to Margrave et al. (2006). In a 2D setting, let Δx be the spatial sample size in the transverse coordinate, and as a result the Nyquist wavenumber is $k_N = \pi / \Delta x$, while the evanescent boundary is at $|k_x| = |k|$. For most surveys, $|k_N| > |k|$ for all frequencies of interest, but this might not be always true. Let's now examine the spectral properties of an n_{op} – length approximate wavefield extrapolator, designed by any method. The spectrum of an n_{op} point operator, \hat{W} , designed with any extrapolation method (e.g. FOCI), will have samples at wavenumbers

$$k_{xop} = \Delta k \left(0, \pm 1, \pm 2, \dots, \pm (n_{op} - 1) / 2 \right), \quad (3.47)$$

where

$$\Delta k = 2\pi / (n_{op} \Delta x). \quad (3.48)$$

That is, the operator has a sample at 0 wavenumber and then $(n_{op} - 1)/2$ samples distributed out to just shy of $+k_N$ in the positive wavenumber band and similarly for the negative wavenumbers. Thus, the operator may have only a few, or in the worst case only one (at zero), such wavenumbers (Figure 3-9), while the data may have hundreds of wavenumbers below $|k_x| = |k|$. As frequency decreases or velocity increases, this becomes increasingly likely to happen. In fact, when extrapolating the wavefield using a fixed-length operator, there will be many circumstances where most operator wavenumbers will fall in the evanescent region. Such operators have poor phase control and are relatively unstable.

Spatially resampling the data at lower frequencies to a sample rate $\Delta x' > \Delta x$ so that most operator wavenumbers fall inside the wavefield region, is a solution to this problem (Figure 3-10). This requires specifying a frequency band of interest, say

$$\omega_{mig} \in [\omega_{min}, \omega_{max}], \quad (3.49)$$

and dealing only with these frequencies. The frequency band, $[\omega_{min}, \omega_{max}]$, is then broken into $npart$ frequency partitions

$$[\omega_{min}, \omega_{max}] = [\omega_{min}, \omega_1) \cup [\omega_1, \omega_2) \dots \cup [\omega_{npart-2}, \omega_{npart-1}) \cup [\omega_{npart-1}, \omega_{max}], \quad (3.50)$$

where the number of frequency partitions, $npart$, is an integer that is greater than zero.

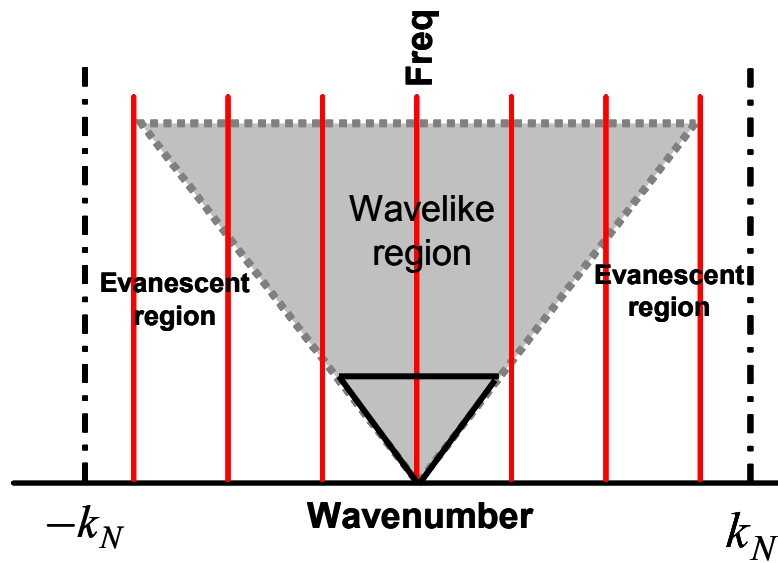


Figure 3-9. In red are the wavenumbers of the spectrum of a 7 point filter. Note that the shaded area bounded by the solid lines contains only one wavenumber which means poor control.

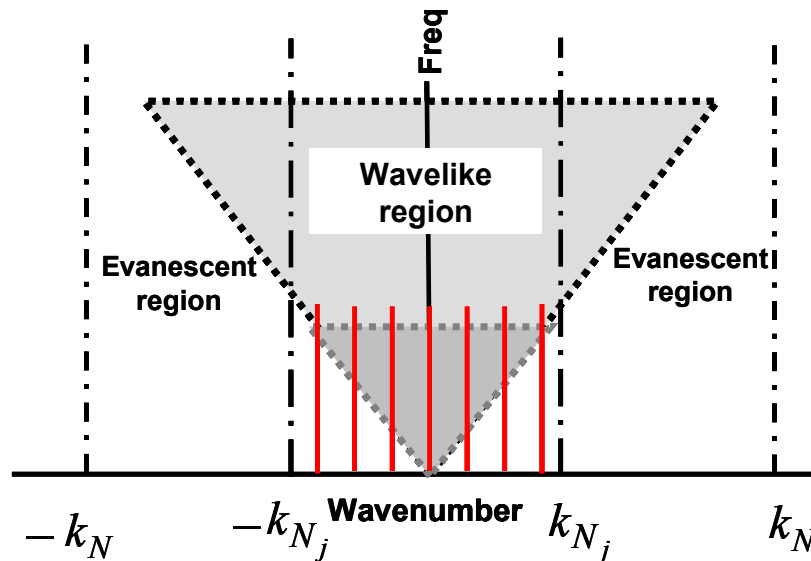


Figure 3-10. After spatial resampling of the j^{th} partition, the wavenumbers of a 7 point operator falls inside the wavelike region where k_{N_j} is the new Nyquist wavenumber, compare with Figure (3-9).

Spatially resample the j^{th} partition from Δx to $\Delta x_j > \Delta x$ such that

$$\alpha \left(\frac{\pi}{\Delta x_j} \right) \leq k_{crit} \leq \beta \left(\frac{\pi}{\Delta x_j} \right), \quad \alpha < \beta \in [0,1], \quad \omega \in [\omega_{j-1}, \omega_j), \quad (3.51)$$

where

$$k_{crit} = \frac{\omega}{V_{crit}}. \quad (3.52)$$

V_{crit} is a velocity that defines the highest evanescent boundary of interest, a good and always sufficient choice for this velocity is

$$V_{crit} = \min(V(x, z)). \quad (3.53)$$

In this thesis, the spatial resampling will be implemented using $\alpha = 0.7$ and $\beta = 0.9$.

Since spatial resampling increases the spatial sample size, an anti-alias filter is required to avoid aliasing. The objective of this filter is to preserve data at the highest wavelike wavenumbers without any loss, yet reject the evanescent energy. This can be accomplished by a truncation operation in the wavenumber domain where data at all wavenumbers greater than the new Nyquist are rejected, and data at wavenumbers greater than k_{crit} are zeroed.

The data has n spatial locations before resampling, and $m_j < n$ wavenumbers are retained after resampling. The new spatial sample interval, Δx_j , can be written as

$$\Delta x_j = \frac{2\pi}{m_j \Delta k_d}, \quad (3.54)$$

where the wavenumber sample interval of the spectrum of the data is

$$\Delta k_d = \frac{2\pi}{n\Delta x}. \quad (3.55)$$

Inserting equation (3.55) into equation (3.54) gives

$$\Delta x_j = \frac{n}{m_j} \Delta x. \quad (3.56)$$

So the new sample interval is formed by multiplication of the original sample interval by the ratio n/m_j . Since $\Delta x_j \geq \Delta x$, the designed operators using Δx_j have a better stability and phase accuracy for propagating waves compared to operators designed with Δx for low k values (Figure 3-11).

After resampling, each partition is extrapolated separately using operators that are calculated using the spatial sample interval that corresponds to that partition. At each depth level, the extrapolated partitions are assembled back to the original spatial sample interval to invoke the imaging condition since it requires a summation over frequency (section 2-2).

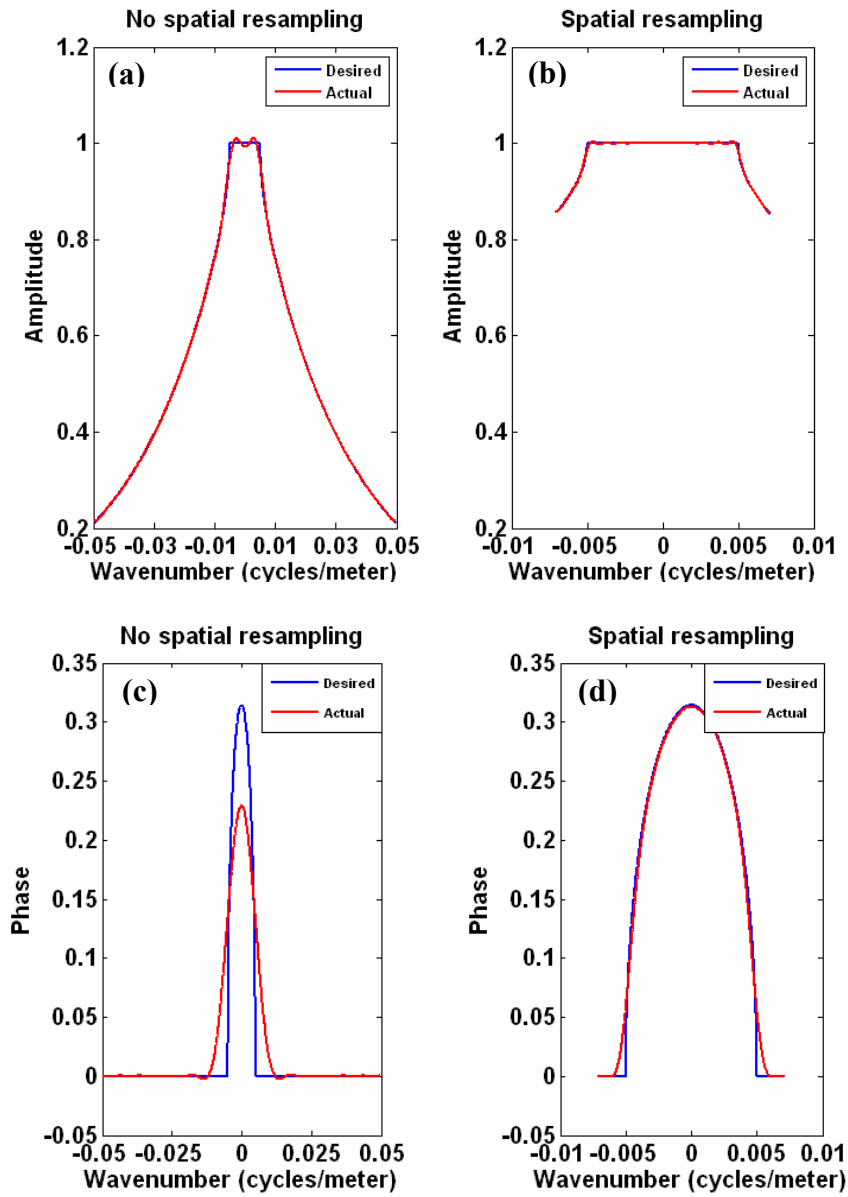


Figure 3-11. Spectra of two operators, designed with and without spatial resampling, compared with the exact spectrum, where (a) and (b) show their amplitudes, and (c) and (d) show their phases. The parameters are: $\Delta x = 10\text{m}$, $\Delta z = 10\text{m}$, $f = 40\text{Hz}$, $V = 2000\text{m/s}$, $n_{op} = 51$ points, and $\Delta x_j = 70\text{m}$.

3-5 A COMPARISON OF THE VARIOUS EXTRAPOLATORS

The stability of the various extrapolators depends significantly on the chosen parameters. For example, for the WLSQ and Soubaras extrapolators, different weight values can dramatically change the stability of the extrapolators. Further, different frequencies may require different weight values.

In a way, the WLSQ and Soubaras methods are similar to the Hale method in that each frequency range may require a different weight value. On the other hand, the stability of the FOCI extrapolator is less sensitive to the parameters.

In this section, the Hale, Soubaras, WLSQ and FOCI extrapolators are compared. The analysis is done by inspecting:

- The amplitudes of the spectra of the various operators compared with the amplitude of the exact spectrum.
- The phase error of the extrapolators in the wavenumber domain.
- Impulse responses of the various extrapolators.
- Prestack depth migration (PSDM) images based on the various extrapolators.

3-5.1 Amplitude and phase spectra

Figure 3-12a shows the amplitudes of the spectra of Hale, Soubaras, WLSQ, and FOCI extrapolators compared with the amplitude of the exact spectrum. The amplitude is plotted between 0.999 and 1.001 to emphasize the oscillatory behaviour of the various

extrapolators⁸. The parameters are $\Delta x = 10$ m, $\Delta z = 10$ m, $f = 50$ Hz, $V = 2000$ m/s and the operator length is 31 points.

Soubaras and WLSQ methods use a weight value, ε , of 10^{-5} for the evanescent region, and 70° for the maximum angle of propagation, α . Also, for the FOCI extrapolator, $n_{inv} = 19$, $n_{for} = 13$, and $\eta = 0.005$. This figure shows that while Hale's extrapolator is perfectly stable⁹, the Soubaras, WLSQ, and FOCI extrapolators are practically stable.

Despite the fact that Hale's extrapolator is more stable than the others, it cannot handle high angles of propagation. In Figure 3-12a, the amplitude of the spectrum of Hale's extrapolator starts decaying well before the evanescent boundary. Also, the FOCI extrapolator has better stability than the Soubaras and WLSQ extrapolators.

Figure 3-12b shows the maximum amplitudes after applying the extrapolator 500 times in a homogenous medium. This figure shows that these operators will not amplify the wavefield significantly even after repeating them 500 times in a homogeneous medium.

Figure 3-13 shows the phase errors of the extrapolators are relatively small.

⁸ This display was originally used by Thorbecke et al. (2004) to compare the WLSQ extrapolator with other methods.

⁹ Perfectly stable also means mathematically stable.

The phase error is the difference between the phase of the spectra of the various operators and the phase of the exact spectrum. This figure shows that the various extrapolators have relatively small phase errors¹⁰.

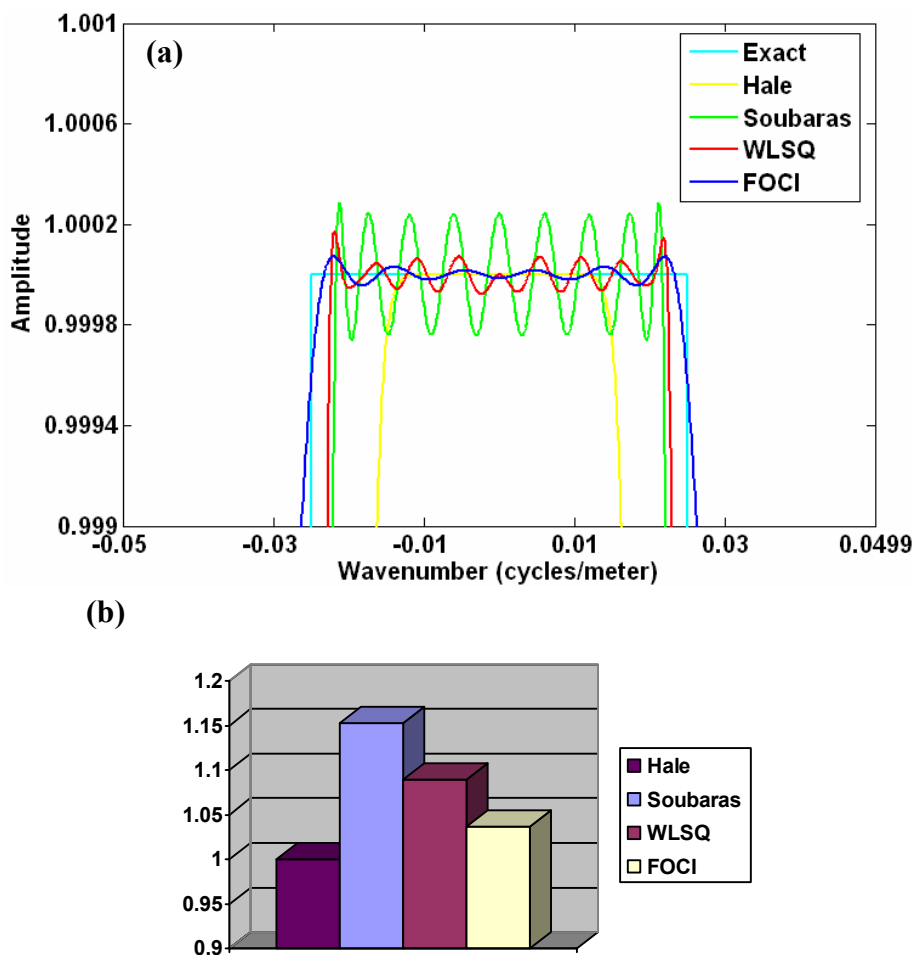


Figure 3-12. The amplitudes spectra of Hale , Soubaras, WLSQ, and FOCI extrapolators in the wavenumber domain compared with the amplitude of the exact spectrum, where (a) shows a zoomed part of the amplitudes of the various extrapolators, and (b) shows the maximum amplitudes after applying the extrapolators 500 times in a homogenous medium.

¹⁰ This criterion was also used by Hale (1991) to analyze the accuracy of wavefield extrapolators.

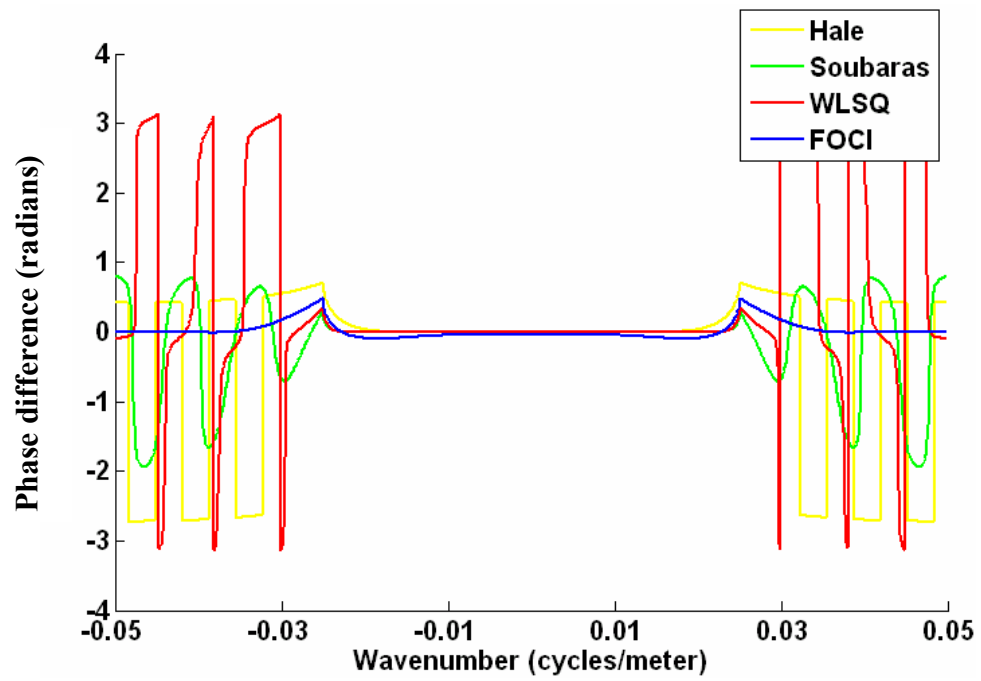


Figure 3-13. Phase errors the Hale, Soubaras, WLSQ, and FOCI extrapolators in the wavenumber domain.

3-5.2 Impulse responses of the Hale, Soubaras, WLSQ and FOCI extrapolators

The impulse responses of the Hale, Soubaras, WLSQ, and FOCI extrapolators are used to analyze their accuracies. The zero-offset experiment (coincident source-receiver) is done with an operator length of 31 points in a homogenous medium, a maximum extrapolation depth of 1280 m, a velocity of 4000 m/s, a spatial spacing of $\Delta x = 10$ m, a vertical spacing of $\Delta z = 10$ m, and a temporal sampling of 0.004 seconds. The trace located at the centre of the input wavefield contains five Ricker wavelets at 0.0600, 0.1240, 0.1880, 0.2520, and 0.3160 seconds. The dominant frequency of the Ricker wavelet is 30 Hz. Both the Soubaras and WLSQ methods use $\varepsilon = 10^{-5}$ and $\alpha = 70^\circ$. For the FOCI result, a 31-point post-design operator was used. Some of these parameters such as the weight value and the maximum angle of propagation were first used by Soubaras (1996) and Thorbecke et al. (2004). Choosing α such that it is less than 90° improves the stability of the Soubaras and WLSQ extrapolators (Thorbecke et al., 2004).

The impulse responses are obtained by downward-continuing the input wavefield using half of the velocity into the subsurface and invoking the exploding reflector imaging condition at each depth level (i.e., simply evaluate the extrapolated wavefield at $t = 0$)¹¹.

Figure 3-14 shows the impulse responses of the various extrapolators compared with the impulse responses of the phase-shift algorithm. The phase-shift response (Figure 3-14a) is as good as it gets in terms of its ability to handle the high angles of propagation.

¹¹ For more about this type of migration, refer to Margrave (2003).

Further, the phase-shift algorithm does not suffer from the numerical instability that these extrapolators might suffer from. So it is a good calibration tool to test the accuracy, stability, and ability of the various extrapolators to handle high angles of propagation. While Hale's extrapolator could not handle high angles of propagation, the Soubaras, WLSQ, and FOCI extrapolators show that they can better handle high angles of propagation. Further, the results of the Soubaras, WLSQ and FOCI extrapolators are comparable. The impulse responses of the various extrapolators show that they have different maximum angles of propagation despite using the same operator length. In general, the ability of the extrapolators to handle high angles of propagation depends on their spatial extents and the methods that are used to design them.

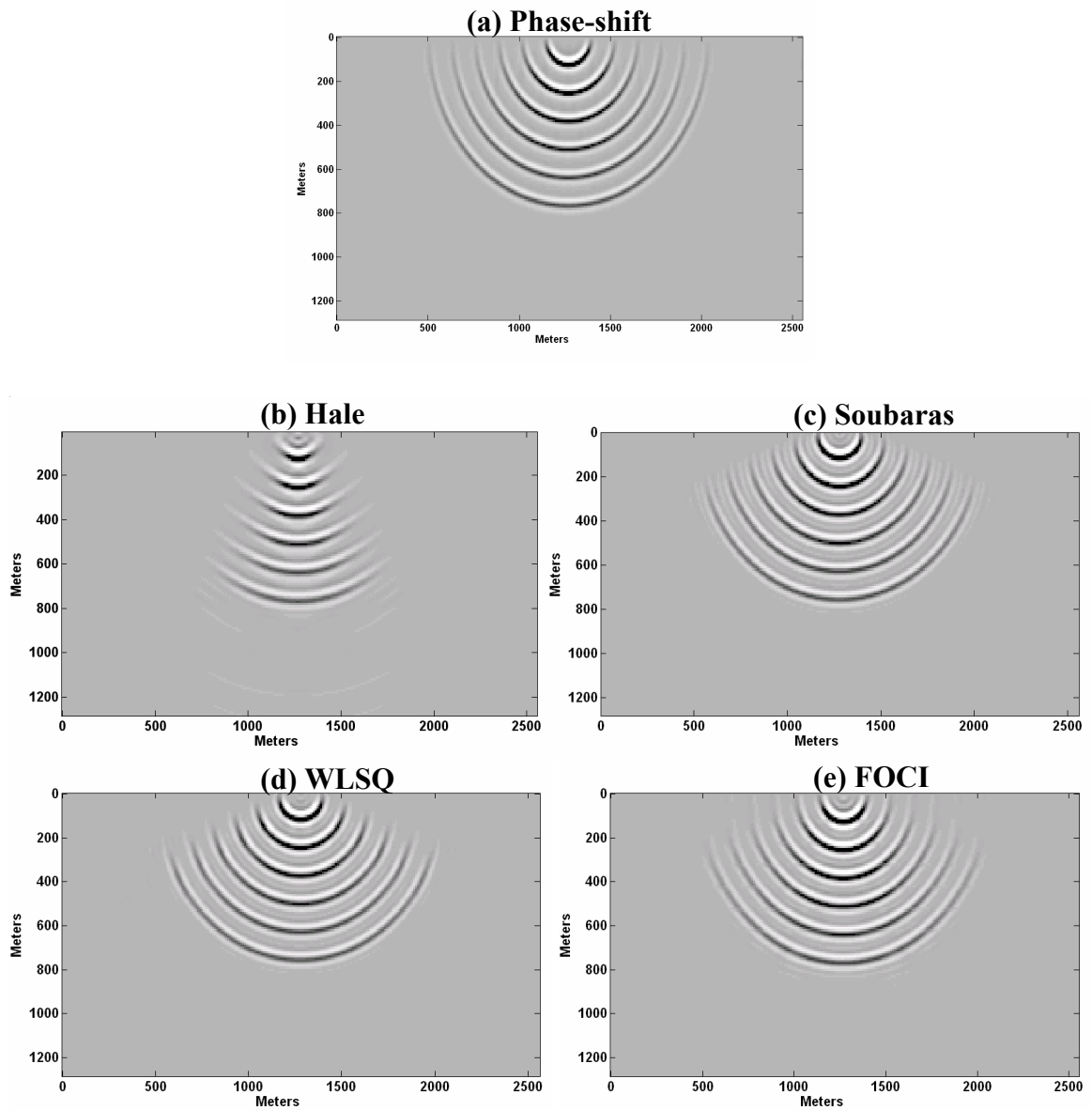


Figure 3-14. Impulse responses of the (a) phase-shift, (b) Hale, (c) Soubaras, (d) WLSQ and (e) FOCI extrapolators for $V=4000$ m/s, $\Delta x=10$ m, $\Delta z=10$ m, and a 31-point operator. The FOCI result was obtained using the spatial resampling technique.

3-5.3 Prestack depth migration with the various extrapolators

A series of tests of the various extrapolation algorithms was conducted in imaging the Marmousi structure with prestack shot profile migration (section 2-2). The 2D acoustic Marmousi dataset was created at the Institut Français du Pétrole (IFP) (Bourgeois et al., 1991). The Marmousi dataset has a strong lateral velocity variation and steeply dipping events, so it is an ideal dataset to test migration algorithms. The dataset consists of 240 individual shot gathers of 96 traces, each in a towed marine streamer configuration. The source and receiver intervals are 25 m; prior to migration, each shot was interpolated to a receiver spacing of 12.5 m to avoid spatial aliasing. Figure 3-15a shows an approximation to Marmousi reflectivity.

The cross-correlation imaging condition is used to generate the images (section 2-2). The operator length used for the Soubaras and WLSQ images is 51 points. For the FOCI result, a post-design operator is used, where $n_{inv} = 121$, $n_{for} = 101$, $n_{win} = 51$, and $\eta = 1$. Due to software limitations of the Symbolic toolbox in MATLAB, Hale's result is not shown.

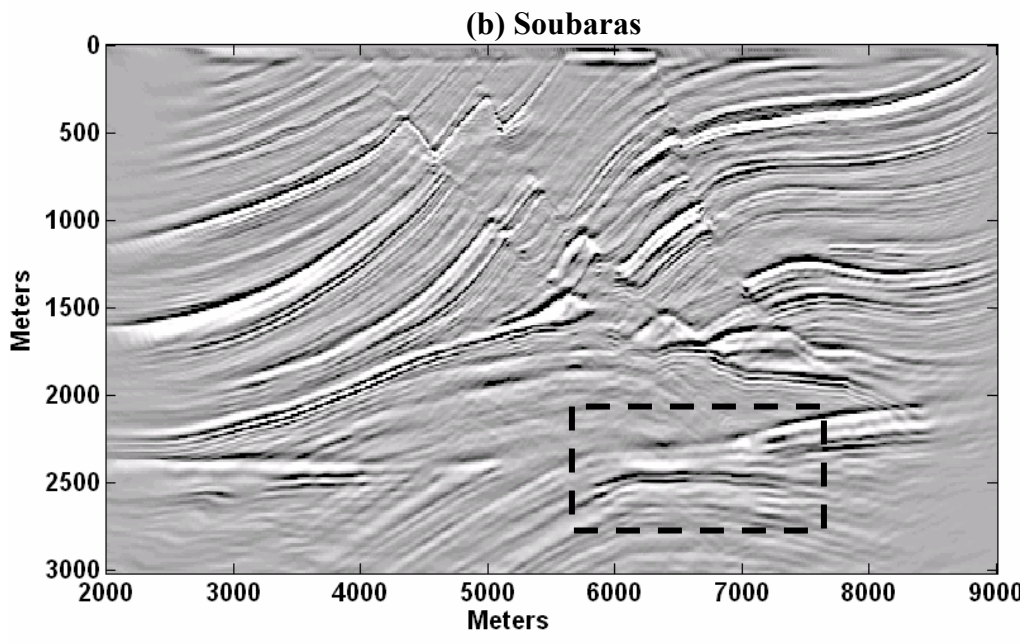
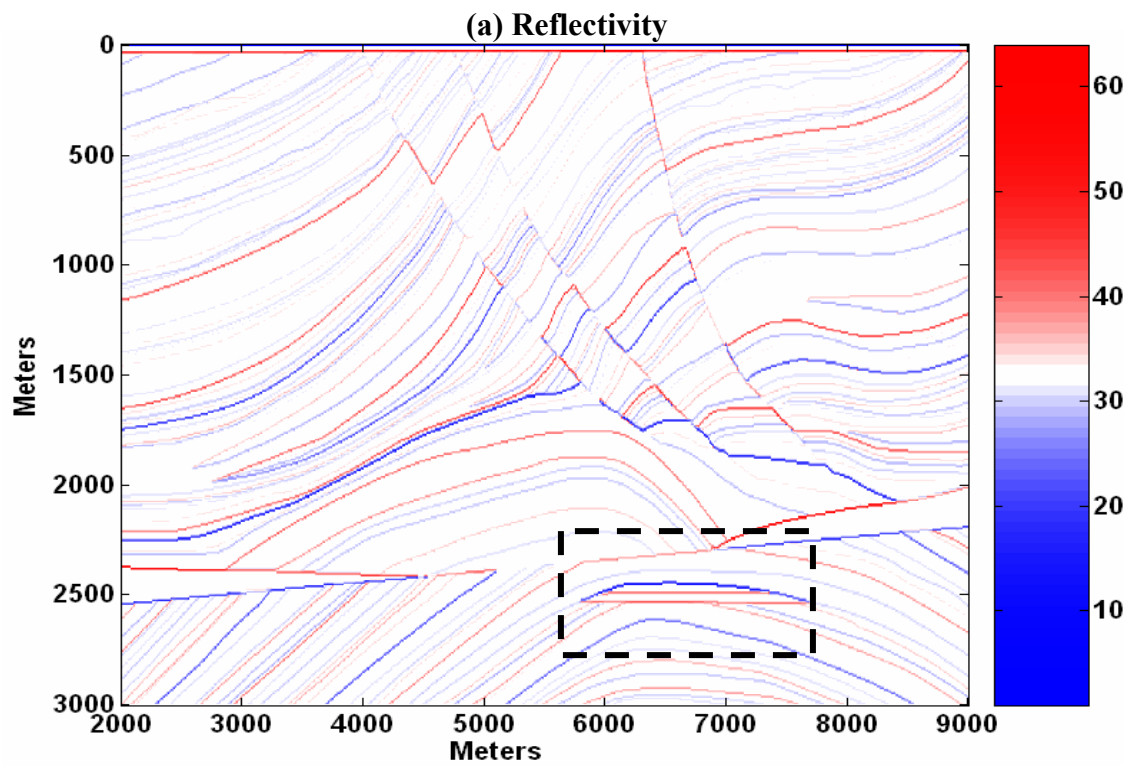
The comparison was done on the whole images and also on zoomed parts of the shallow and deep sections of the Marmousi dataset. Figures 3-15b, 3-15c, and 3-15d show the migration results using the Soubaras, WLSQ, and FOCI extrapolators, respectively. The three methods handled the strong lateral velocity variations and the steeply dipping events. Figures 3-16a, 3-16b, and 3-16c show zoomed parts of the shallow and deep

sections of the Marmousi dataset. There are no significant differences between the three extrapolators; i.e., the results are comparable. The WLSQ and FOCI images, however, contain low frequency noise that could result from weak evanescent filtering in the shallow sections. Due to spatial resampling, the FOCI method is more efficient than WLSQ and Soubaras. Spatial resampling can conceivably be incorporated into any method, though it requires great flexibility in operator design, at which FOCI excels.

3-6 CHAPTER SUMMARY

Unlike Hale's extrapolator, the Soubaras, WLSQ, and FOCI extrapolators are not perfectly stable but have controllable instabilities. However, they can handle higher angles of propagation than Hale's. The stabilities of the Soubaras and WLSQ extrapolators are sensitive to the value of the weight that is used in these methods.

Calculating tables of extrapolators using the Soubaras, WLSQ, and FOCI methods is computationally more efficient than using Hale's method. In particular, FOCI results are comparable with results obtained with other known methods such as Hale's, Soubaras's, and WLSQ extrapolation methods, but the FOCI method, with spatial resampling, is computationally less expensive than the other methods.



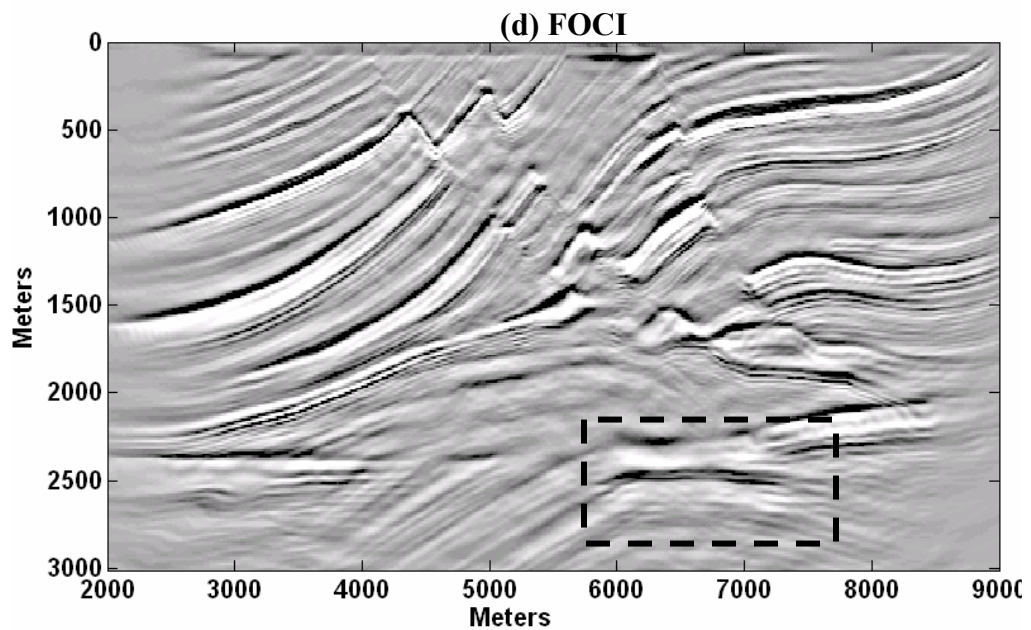
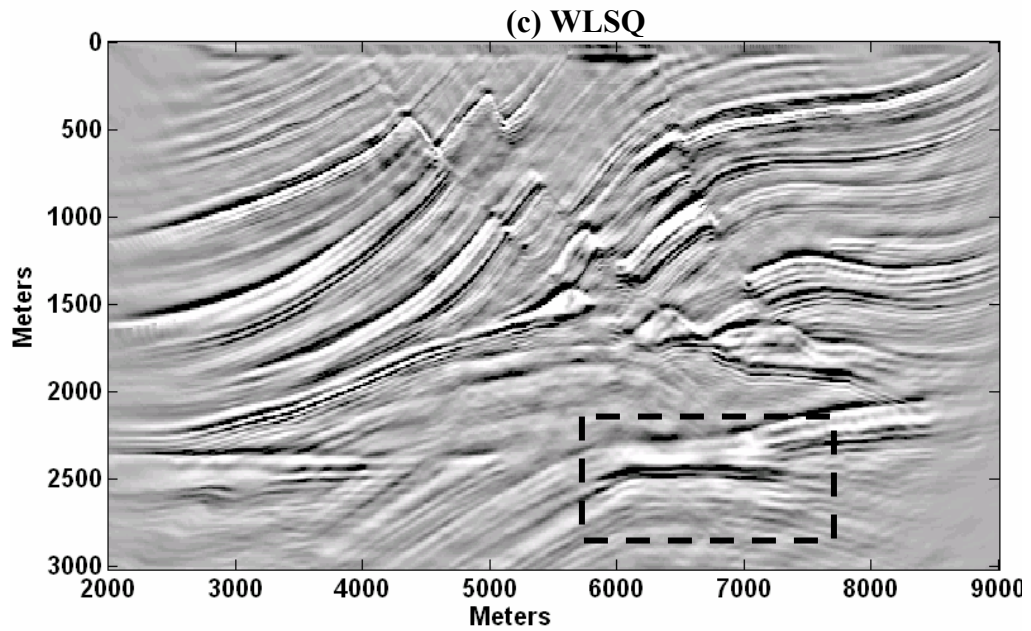


Figure 3-15. Prestack depth migration results from the Marmousi dataset, where (a) shows the reflectivity, and (b), (c), and (d) show the results with the Soubaras, WLSQ, and FOCI extrapolators, respectively (the dashed box contains the target).

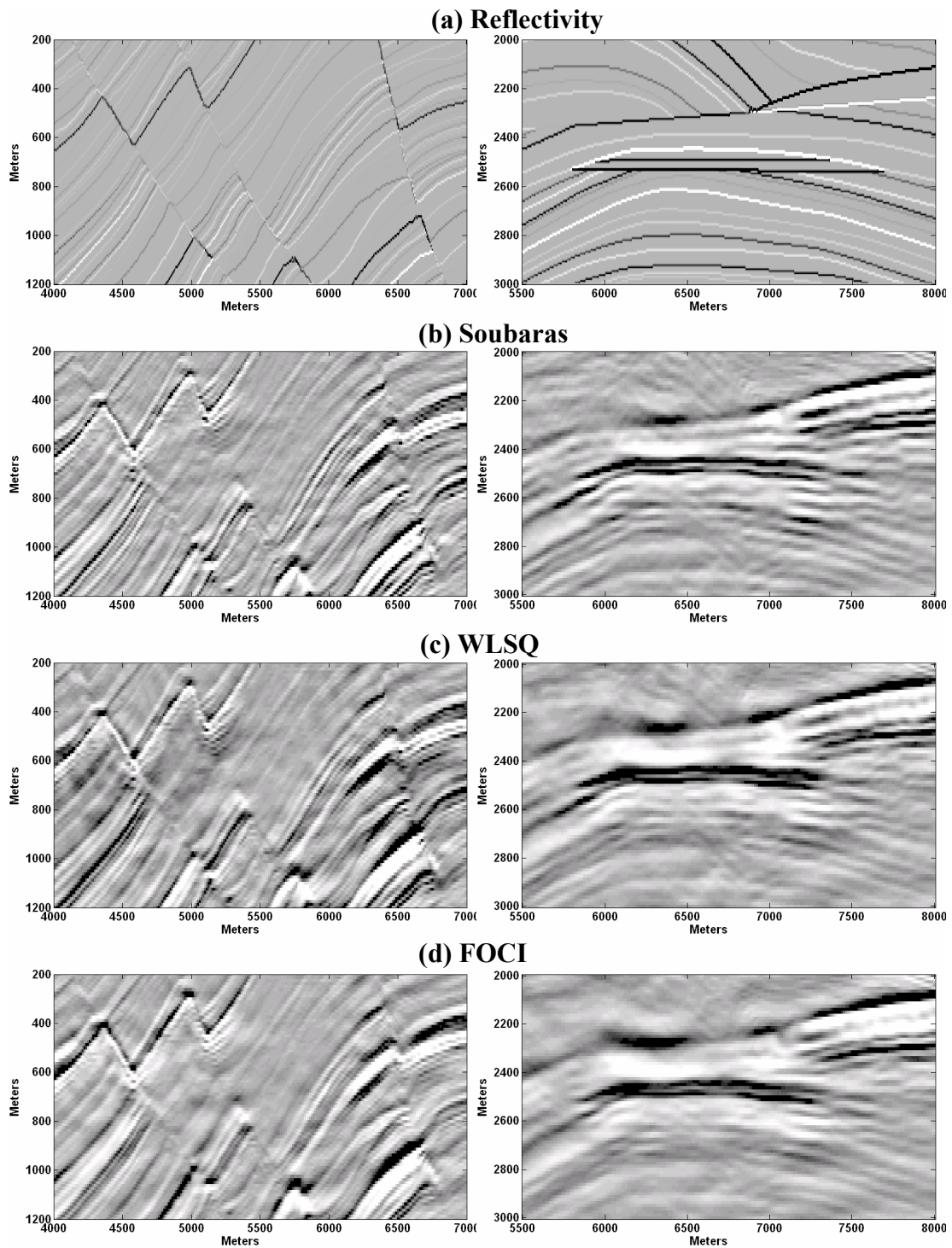


Figure 3-16. Zoomed parts of the shallow central sections of Figures 3-15a, 3-15b, 3-15c, and 3-15d.

CHAPTER 4: USING A TRANSITION BAND IN THE WEIGHTED LEAST-SQUARES DESIGN OF WAVEFIELD EXTRAPOLATORS AND FOCI ENHANCEMENT

A theoretical review of four wavefield extrapolators was presented in Chapter 3. This presentation puts them in the same context to ease understanding and comparing them. In this chapter, the weighted least-squares with a transition band (WLSTB) approach, for designing wavefield extrapolators, is presented. Both the WLSQ (section 3-3) and WLSTB (section 4-1.3) approaches use the L_2 norm¹² to measure the error of the desired and actual spectra, but they use different desired spectra and weight functions.

In this chapter, the WLSTB approach is first derived and then compared to the WLSQ approach, using the same comparison tools that were used in the previous chapter. Then, it is used to optimize the FOCI algorithm.

4-1 LEAST-SQUARES-BASED METHODS FOR DESIGNING WAVEFIELD EXTRAPOLATORS

Three error measures are usually used in designing filters:

1. The least-squares approximation, in which the average of the squared-error is measured, or the " L_2 " norm.

¹² The L_2 minimizes the error between the desired and actual spectra.

2. The Chebyshev approximation, based on the maximum error, or the " L_∞ " norm.
3. The Butterworth or maximally flat approximation that is based on the Taylor series expansion of the desired spectrum.

Soubaras (1996) used the error measure that is based on Chebyshev approximation. Most extrapolation methods, however, measure the error in a least-squares sense. For example, Holberg used non-linear least-squares; Thorbecke et al. (2004) used weighted least-squares; and Margrave et al. (2006) used least-squares to design the inverse operator.

From section 3-3, a least-squares solution that minimizes the weighted error function,

$$E = \sum_{k_x} \Upsilon \left| \hat{W} - \hat{W} \right|^2, \quad (4.1)$$

can be then given as

$$\underline{\tilde{W}} = \left[\underline{\underline{F}}^H \underline{\underline{\Upsilon}} \underline{\underline{F}} \right]^{-1} \underline{\underline{F}}^H \underline{\underline{\Upsilon}} \hat{W}. \quad (4.2)$$

Note that the desired spectrum in equation (4.2) is the exact spectrum, \hat{W} . There are three methods for obtaining a least-squares solution to the above approximation (Parks and Burrus, 1987; Selesnick et al., 1996):

- Unweighted least-squares.
- Weighted least-squares using a transition function to connect the wavelike and evanescent regions.
- Weighted least-squares using a transition band placed between the wavelike and evanescent regions.

4-1.1 Unweighted least-squares

Unweighted least-squares solutions can be obtained by setting the diagonal entries of the weight matrix, Υ , equal to one, or $\varepsilon = 1$ in equation (3.35) (section 3-3). Unweighted least-squares solutions use the same weight value for the wavelike and evanescent regions. It is well established (Parks and Burrus, 1987; Selesnick et al., 1996; Thorbecke et al., 2004) that operators designed with unweighted least-squares are often unstable.

4-1.2 Weighted least-squares using a transition function

The amplitude and phase of the extrapolator, in the wavenumber domain, must match the amplitude and phase of the exact spectrum in the wavelike region, and be only less than unity in the evanescent region. The extrapolator design problem can be made much more flexible by introducing a transition region between the wavelike and evanescent regions. This formulation fits the way filter specifications are usually given much better than designating one wavenumber to specify the boundary between the wavelike and evanescent regions. Also, the *Gibbs phenomenon* can be minimized (section 2-5.1), and the approximation in the wavelike and evanescent regions can be dramatically improved.

The weighted least-squares (WLSQ, Thorbecke et al., 2004) approach is an example of a method that uses a transition function. That is, a spline function goes from k_α to the Nyquist wavenumber, $\pi / \Delta x$ (Figure 4-1a). In this case, the evanescent region becomes

the transition region¹³. The desired spectrum, \hat{W}_D , does not have the slope discontinuities that are present in the exact spectrum, \hat{W} (section 2-5.1), which can cause an inaccurate approximation. The WLSQ extrapolator can be obtained using

$$\underline{\tilde{W}} = \left[\underline{F}^H \underline{\Upsilon} \underline{F} \right]^{-1} \underline{F}^H \underline{\Upsilon} \hat{W}_D. \quad (4.3)$$

Using a transition region in the desired spectrum can significantly reduce the *Gibbs phenomenon* and give greater control over the design process. The transition region allows for a smooth transition between the wavelike and evanescent regions. In fact, when Thorbecke and Revert (1994) used the exact spectrum, \hat{W} , in equation (4.2), the resultant operator, \tilde{W} , was less stable than using \hat{W}_D (compare equations (4.2) and (4.3)). This shows that the choice of the desired spectrum has a large impact on the resulting operator. In fact, this approach is a well known concept in the design of finite impulse response (FIR) filters.

4-1.3 Weighted least-squares using a transition band

One of most effective modifications of the least-squares (LS) error design methods is to change the band of wavenumbers over which the minimization is carried out (Parks and Burrus, 1987).

¹³ In the literature of finite impulse response (FIR) design, the transition function is only used to connect two regions.

The band of wavenumbers for the transition region can be simply removed from the error definition. The region is called the transition band or “don’t care” region. In the weighted least-squares using a transition band (WLSTB) approach, the desired spectrum is the exact spectrum. That is, the exact spectrum is not modified by using a transition function as was the case in the WLSQ approach. It uses, however, a different weight function that can be defined as

$$\tilde{Y}(k_x) = \begin{cases} 1; & |k_x| \leq k_\alpha \\ 0; & k_\alpha < |k_x| < |2k - k_\alpha| \\ \varepsilon; & |2k - k_\alpha| < |k_x| < \frac{\pi}{\Delta x} \end{cases} . \quad (4.4)$$

(Refer to section 3-3 for a formal definition of the terms in the above equation). The region $k_\alpha < |k_x| < |2k - k_\alpha|$ is called the transition band, where it is excluded from the error measure by giving it a weight value of zero. Figure 4-1b shows the amplitude of the exact spectrum after removing this band. The WLSTB extrapolator can be then designed using

$$\underline{\tilde{W}} = \left[\underline{F}^H \underline{\tilde{Y}} \underline{F} \right]^{-1} \underline{F}^H \underline{\tilde{Y}} \underline{\hat{W}} . \quad (4.5)$$

This approach should, in theory, give a smaller squared error and a greater reduction of the overshoot than should be expected using a transition function, because there is no constraint placed on the exact spectrum, $\underline{\hat{W}}$, in the transition region (Parks and Burrus, 1987).

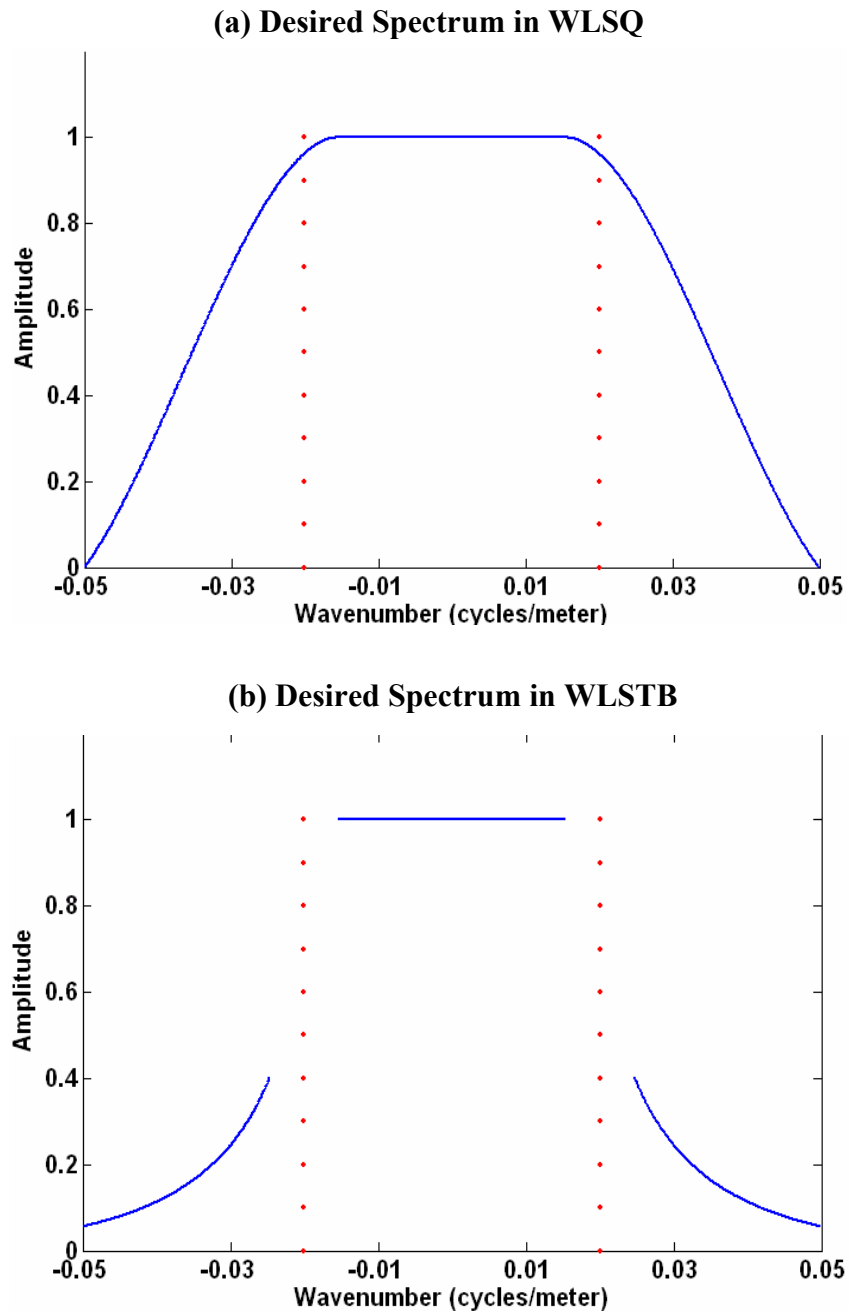


Figure 4-1. Amplitudes of the desired spectra in (a) the WLSQ, and (b) the WLSTB approaches. The dotted lines indicate the evanescent boundaries. The parameters are $\Delta x = 10$ m, $\Delta z = 10$ m, $f = 50$ Hz, and $V = 2000$ m/s.

4-2 A COMPARISON BETWEEN THE WLSQ AND WLSTB EXTRAPOLATORS

For simplicity, the spectrum of the WLSQ extrapolator will be denoted as \hat{W}_F , where the subscript F indicates using a transition function to design it, and the spectrum of the WLSTB extrapolator will be denoted as \hat{W}_B , where the subscript B indicates using a transition band to design it.

Figure 4-2 shows the amplitude spectra of \hat{W}_F and \hat{W}_B , where the amplitude of the exact spectrum, \hat{W} , is shown for comparison. The same parameters that were used by Thorbecke et al. (2004) are used here to reproduce this figure¹⁴ for a fair comparison. The amplitude of \hat{W}_B shows a better approximation to the amplitude of \hat{W} than the amplitude of \hat{W}_F . Further, the oscillations of the amplitude of \hat{W}_B , which can amplify the wavefield when using it recursively, are less than the amplitude of \hat{W}_F . On the other hand, the phases of \hat{W}_F and \hat{W}_B extrapolators show that both have a good phase control, and they are similar to the phase of \hat{W} (Figure 4-3).

¹⁴ I refer to Figure 2.d in Thorbecke et al. (2004).

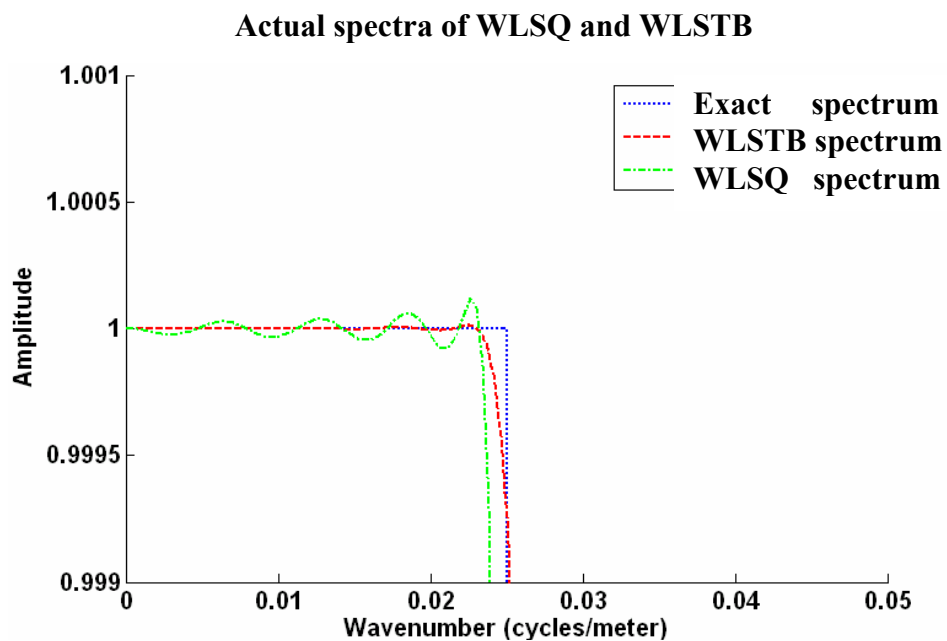


Figure 4-2. Amplitudes of the exact spectrum, WLSQ spectrum, and WLSTB spectrum, where $\Delta z = 2$ m, $\Delta x = 10$ m, $f = 50$ Hz, $V = 2000$ m/s, and $\alpha = 70^\circ$.

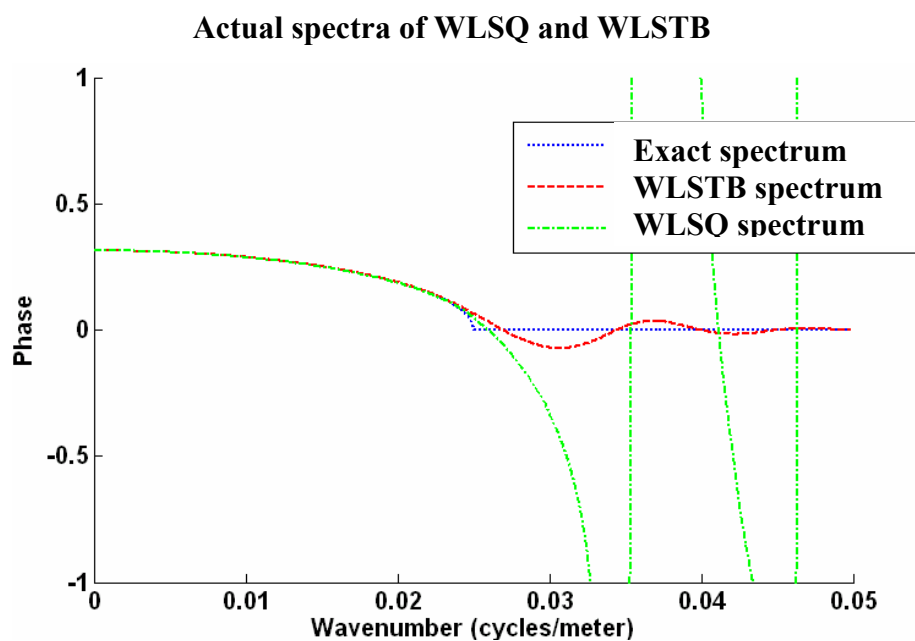


Figure 4-3. Phases of the exact spectrum, WLSQ spectrum, and WLSTB spectrum, where $\Delta z = 2$ m, $\Delta x = 10$ m, $f = 50$ Hz, $V = 2000$ m/s, and $\alpha = 70^\circ$.

4-2.1 Impulse response results using the WLSQ and WLSTB extrapolators

The impulse responses of the WLSQ and WLSTB extrapolators are shown in Figure 4-4, compared with the impulse responses of the phase-shift extrapolator. The phase-shift response (Figure 4-4a) is as good as it gets in terms of its stability and ability to handle the high angles of propagation. Refer to section (3-5.2) for more about how these experiments were conducted.

The parameters are $\Delta z = 10$ m, $V=4000$ m/s, $\Delta x = 10$ m, $\Delta t = 0.004$ seconds, and the operator length for both results is 25 points. Although the WLSTB extrapolator is more stable than the WLSQ, as shown in Figure 4-1¹⁵, the impulse responses of the WLSQ and WLSTB show no noticeable difference. The reasons for this are two-fold: (1) the number of extrapolation steps is relatively small; and (2) despite the fact that the WLSTB operator is more stable than the WLSQ, the deviation of the WLSQ extrapolator from unity is very small.

However, both results differ from the phase-shift migration result in that the high angles of propagation were better handled using the phase-shift algorithm. The reason for that is that both the WLSQ and WLSTB extrapolators are relatively short. To handle high angles of propagation (e.g. close to 90 degrees), the spatial extent of these extrapolators must be very long, which requires more computational effort.

¹⁵ Figure 1 shows that the amplitude of the WLSQ operator is less stable than the amplitude of the WLSTB operator.

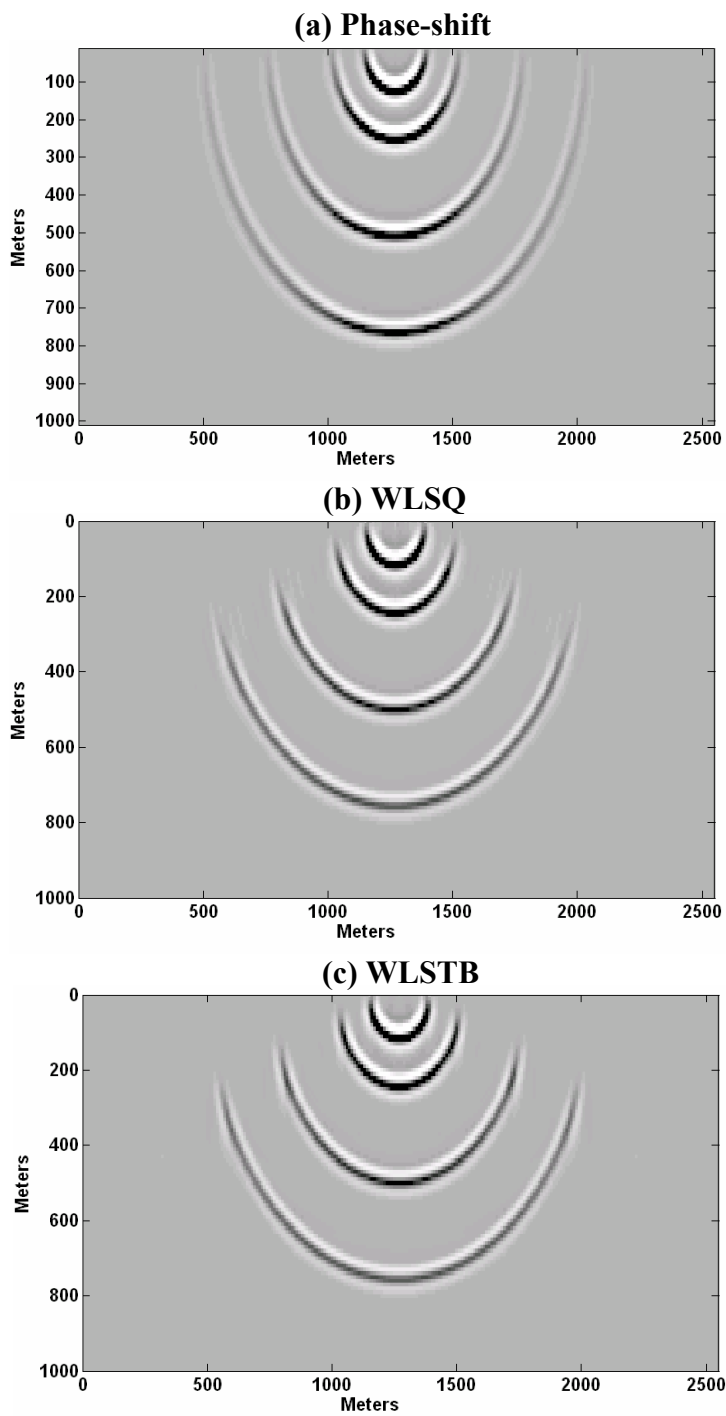


Figure 4-4. Impulse responses of the (a) phase-shift extrapolator, (b) WLSQ extrapolator, and (c) WLSTB extrapolator.

4-2.2 Prestack depth migration results using the WLSQ and WLSTB extrapolators

The Marmousi dataset (Bourgeois et al., 1991), with a maximum dip closed to 90° , is used to test the accuracy of the WLSQ and WLSTB extrapolators. Figure 4-5 shows a detailed comparison of the shallow central sections of the Marmousi dataset of (a) the WLSQ and (b) the WLSTB results. The parameters are $\Delta x = 8.3333$ m, $\Delta z = 8.3333$ m, and the operator length for both results is 31 points. The cross-correlation imaging condition was used to generate these results (section 2-2). In general, the two results are comparable, which means that both extrapolators are effective in handling complex geology. However, the image of the dipping events in the section obtained with a WLSTB extrapolator is superior to the WLSQ image (arrows in Figure 4-5). The WLSTB image, however, contains some low frequency noise in the shallow section that could result from weak evanescent filtering.

4.3 USING THE WLSTB APPROACH TO ENHANCE THE FOCI ALGORITHM

From section 3-4, two operators are used in the FOCI algorithm: (1) a forward operator obtained from windowing the ideal operator for a half depth step (equation (3.43)), and (2) an inverse operator that is specified as a band-limited inverse of the forward operator (equation (3.44)). The least-squares FOCI operator is formed by convolving the first operator with the conjugate of the second (equation (3.45)). This FOCI operator can be windowed to generate a shorter post-design operator (equation (3.46)). The windowing that is currently used in FOCI is done with a Hanning window to obtain the forward and post-design operators.

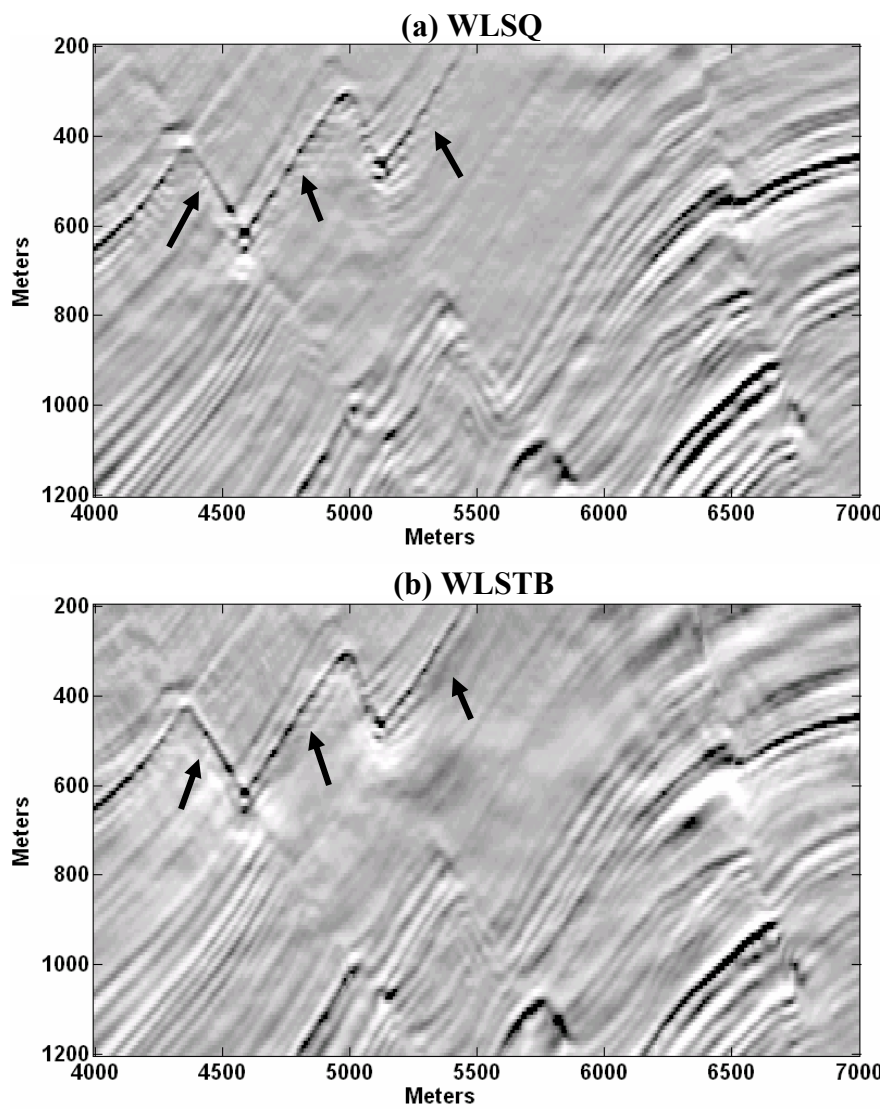


Figure 4-5. A detailed comparison of the shallow central part of the Marmousi dataset, where (a) is the WLSQ result, and (b) is the WLSTB result. The arrows show some comparison areas.

Using a Hanning window for designing operators is suboptimal because it does not minimize the error between the actual and desired spectra. To optimize the FOCI algorithm, the suboptimal windowing is replaced with a weighted least-squares approach. Thus, instead of using a Hanning window to obtain the forward operator, the WLSTB approach is used

$$\underline{\tilde{W}}_{for} = \left[\underline{F}^H \underline{\Upsilon} \underline{F} \right]^{-1} \underline{F}^H \underline{\Upsilon} \hat{\underline{W}}, \quad (4.6)$$

where $\underline{\tilde{W}}_{for}$ is an $N \times 1$ vector that contains the coefficients of the forward operator, which is now obtained in a weighted least-squares sense (refer to section 3-3 for the dimensions of vectors and matrices in equation (4.6))¹⁶. The inverse operator can be then obtained as a band-limited inverse to this optimized forward operator using equation (3.44), and the FOCI operator, $\tilde{\underline{W}}$, for the full depth step can be assembled using equation (3.45) (see section 3-4 for more details)¹⁷. Similarly, the post-design operator can also be obtained optimally using the WLSTB approach

$$\underline{\tilde{W}}_{win} = \left[\underline{F}^H \underline{\Upsilon} \underline{F} \right]^{-1} \underline{F}^H \underline{\Upsilon} \hat{\underline{W}}, \quad (4.7)$$

where in the old design, it was obtained by windowing the FOCI operator with a Hanning window. Note that the desired spectrum is the spectrum of the FOCI operator, $\hat{\underline{W}}$, which means that $\underline{\tilde{W}}_{win}$ is a least-squares¹⁸ approximation to $\tilde{\underline{W}}$. The FOCI algorithm that uses

¹⁶ Also, compare equation (4.6) with equation (3.49) in which the forward operator was obtained using a Hanning window.

¹⁷ So far the only difference between this development and the previous one, shown in section 3-3, is obtaining the forward operator with WLSTB instead of using a Hanning window.

¹⁸ This also means that the post-design operator is a smooth version of the FOCI operator.

WLSTB to obtain the forward and post-design operators will be referred to as the optimized algorithm.

4-3.1 Amplitude and phase spectra comparisons

Figure 4-6a shows a comparison of the amplitude spectra of \hat{W}_{for} before and after the enhancement, where the amplitude of the exact spectrum is shown for comparison. The amplitude of the optimized operator better matches the amplitude of the exact spectrum than the amplitude of the old design. This indicates that using WLSTB is more effective in obtaining a stable forward operator. Phase spectra for the old and new designs are shown in Figure 4-6b, compared with the phase of the exact spectrum. The phase of the optimized forward operator, in the wavenumber domain, shows a better approximation to the phase of the exact spectrum than does the phase of the old design.

Figure 4-7a shows a comparison of amplitudes of the exact, FOCI, and optimized FOCI operators in the wavenumber domain. Their phases are shown in Figure 4-7b. The amplitude of the optimized operator shows a better stability than the old design, and its phase better approximates the phase of the exact spectrum. Also, the oscillations of the phase of the optimized FOCI operator, in the evanescent region (Figure 7b), will not have a significant impact on the final image because the amplitude of the extrapolator in this region is less than unity, and repeated applications of the extrapolator will decay any phase errors.

The post-design operator is another feature of the FOCI algorithm that generally has strong evanescent filtering, but should be long enough to preserve high propagating wavenumbers¹⁹ in the old design. The optimized algorithm can now generate short post-design operators that are more stable than the old designs.

Figure 4-8a shows the amplitude of \hat{W}_{win} before and after the optimization, compared with the amplitude of the exact spectrum. The amplitude of the optimized operator has a wider spectrum than the old-design. This means it can handle higher angles of propagation more efficiently. Also, the phase of \hat{W}_{win} better approximates the phase of the exact spectrum (Figure 4-8b).

¹⁹ In the old design, the short post-design operators tend to decay high wavenumbers during extrapolation because they are obtained with a Hanning window.

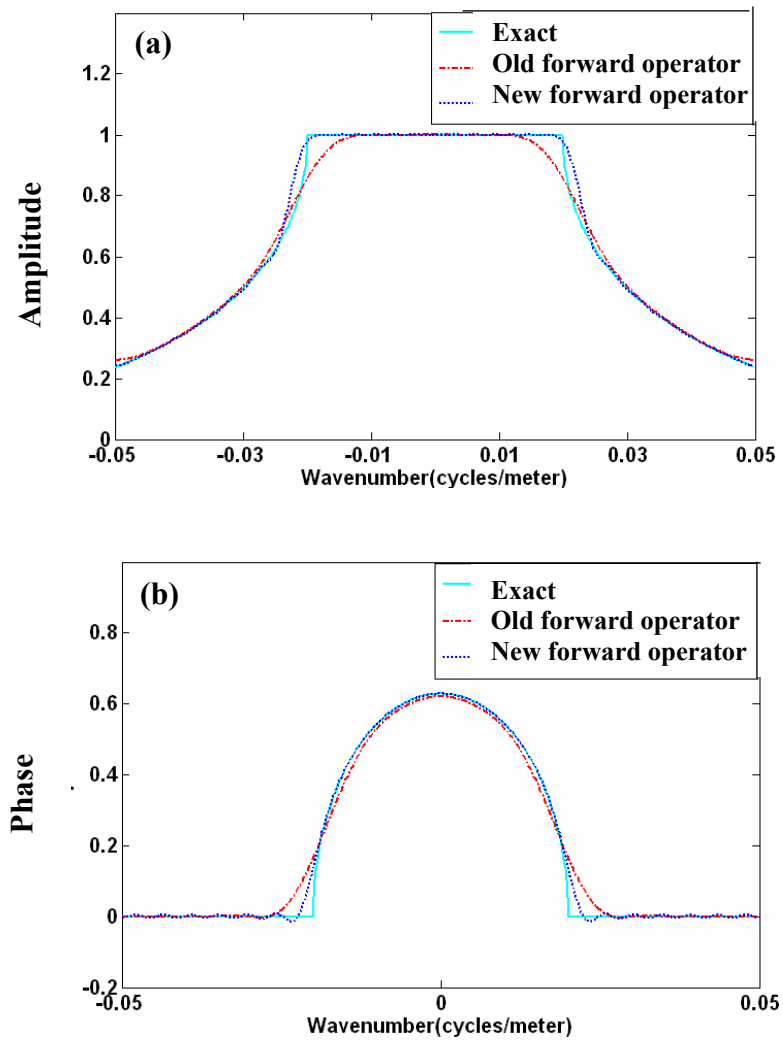


Figure 4-6. (a) Amplitudes and (b) phases of the exact, old forward, and optimized forward operators in the wavenumber domain. The parameters employed are $\Delta x = 10$ m, $\Delta z = 10$ m, and $f = 40$ Hz, and the length spatial length of the forward operator is 21 points.

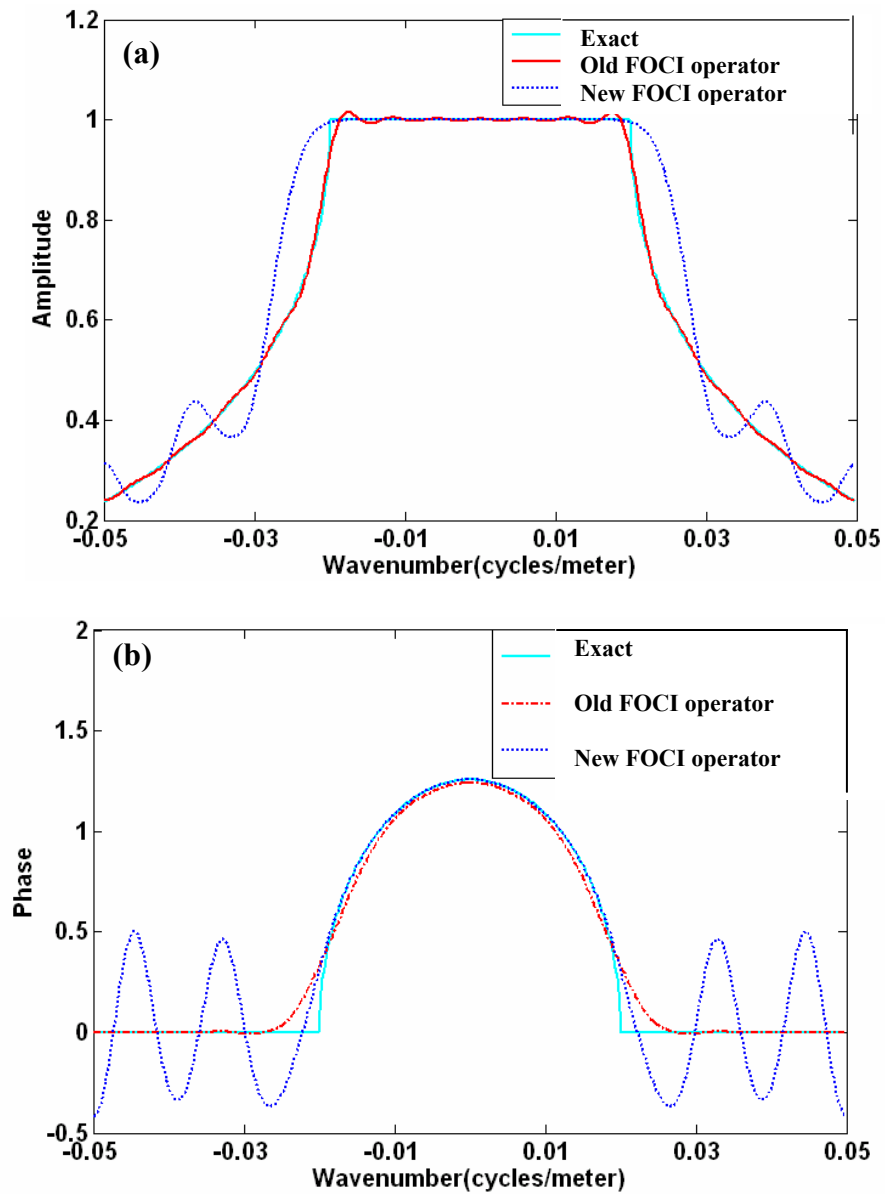


Figure 4-7. (a) Amplitudes and (b) phases of the exact, old FOCI, and optimized FOCI operators in the wavenumber domain. The parameters employed are $\Delta x = 10$ m, $\Delta z = 10$ m, $f = 40$ Hz, $\eta = 1$, and the length of the FOCI operator is 51 points.

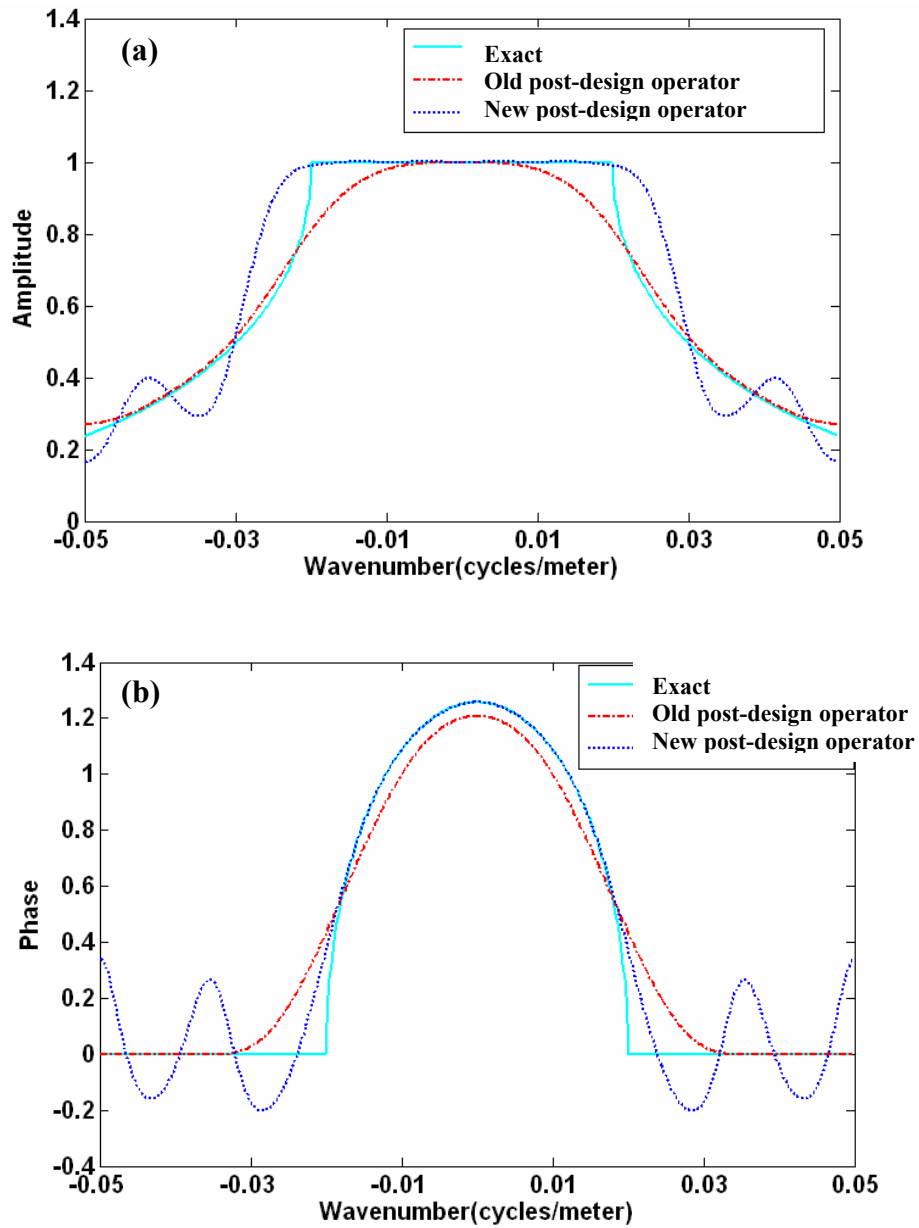


Figure 4-8. (a) Amplitudes and (b) phases of the exact, old post-design operator, and optimized post-design operator in the wavenumber domain. The parameters are $\Delta x = 10$ m, $\Delta z = 10$ m, $f = 40$ Hz, and the operator length is 15 points.

4-3.2 Impulse response examples

Figure 4-9 shows a comparison of the impulse responses of the phase-shift (Figure 4-9a), the FOCI (Figure 4-9 b), and the optimized FOCI (Figure 4-9c) operators. Spatial resampling was used in both FOCI results (section 3-4.2). These experiments were conducted using the same parameters that were used in section 3-5.2 except that the operator length is now 15 points, where post-design operators, designed using the old and new FOCI algorithms, were used to conduct these tests.

Spatial resampling improves the ability of short operators to handle the high angles of propagation (section 3-4.2). Short operators designed using the old algorithm and implemented with spatial resampling, however, could not handle such angles (Figure 4-9b), because they were not obtained optimally. On the other hand, the optimized algorithm has improved the response over the old design (Figure 4-9c), where the high angles of propagation were better handled and the response better matches the phase-shift result (Figure 4-9a).

Figure 4-10 shows the impulse responses of two implementations of the optimized FOCI algorithm: without spatial resampling (Figure 4-10a) and with spatial resampling (Figure 4-10b). From these figures, these short optimal operators can be seen to be capable of handling the high angles of propagation if implemented with spatial resampling. It is the combination of these optimal operators and spatial resampling that allow the optimized algorithm to handle such high angles of propagation with such short operators.

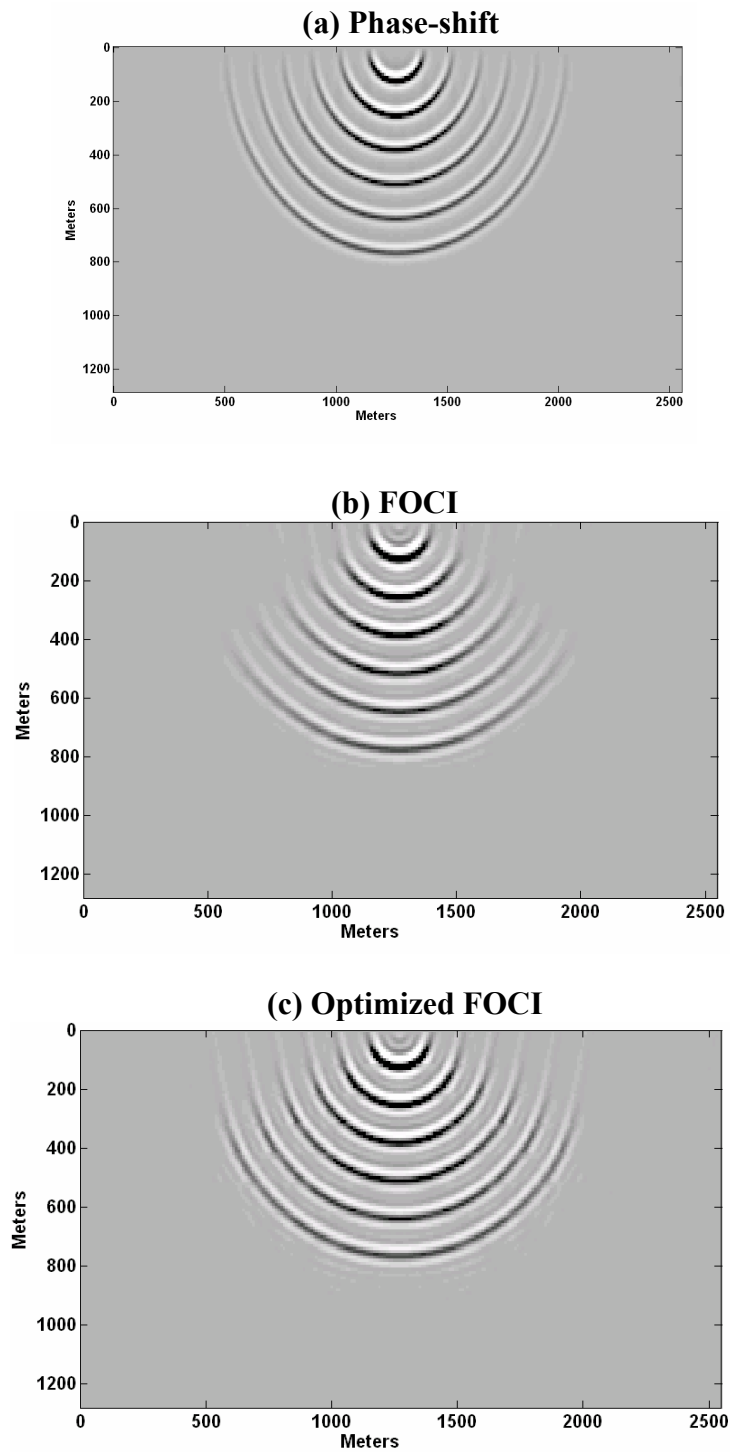


Figure 4-9. Impulse responses of (a) the phase-shift, (b) FOCI, and (c) the optimized FOCI algorithms using $\Delta x = 10$ m, $\Delta z = 10$ m, $V = 4000$ m/s, and an operator length of 15 points.

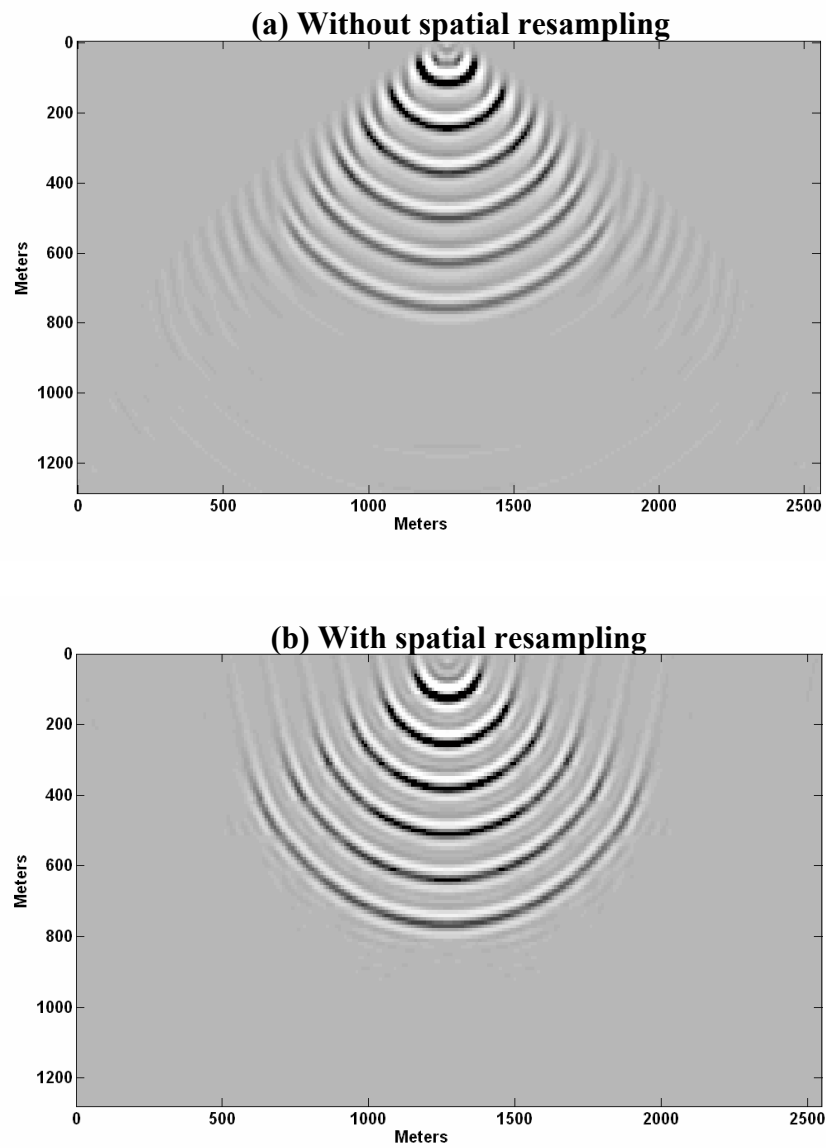


Figure 4-10. Impulse responses of the optimized FOCI algorithm implemented (a) without and (b) with spatial resampling, where an operator length of 11 points was used.

4-3.3 Images of the Marmousi dataset using the FOCI and the optimized FOCI algorithms

Prestack depth migrations (PSDMs) of this dataset were done using the FOCI and optimized FOCI algorithms with post-design operators of different lengths. The results are compared with the old design of FOCI to show the effects of the enhancements. The migration results of the FOCI and the optimized FOCI are shown in Figures 4-11a and 4-11b. The FOCI image that was shown in Figure 3-15d is superior to the image shown in Figure 4.11a because a longer operator was used in Figure 3.15d. Also, comparing the FOCI image (Figure 4.11a) with the reflectivity (Figure 3.15a) shows that the reflectors have the wrong depths due to using suboptimal short operators.

It is apparent that the image in Figure 4-11b is in better agreement with the reflectivity in Figure 3-15a. Figure 4-12a shows a close-up of the central part of Figure 3-15a and Figures 4-12b and 4-12c show close-ups of Figures 4-11a and 4-11b. These demonstrate that much more detail can be seen with the optimized operator, even with just 15 points. The FOCI image that was shown in Figure 3-15d is superior to the image shown in Figure 4.11a because a longer operator was used. Therefore, using WLSTB in FOCI enables us to obtain more efficient operators.

Figure 4-13 shows the PSDM image with a 9-point operator. This demonstrates that a good image of the Marmousi dataset can still be obtained with such a short operator.

Figure 4-14 shows different comparisons of FOCI versus the optimized FOCI with different operator lengths. For example, Figure 4-14a shows close-ups of the best image

obtained using the old design, and Figure 4-14b shows the corresponding image obtained with the optimized algorithm using the same operator length. They are similar, but much more detail is visible with the optimized operator.

As the operator length decreases from 15 points (Figure 4-14c) to 9 points (Figure 4-14d), we can still see significant detail in the image. Figure 4-15 shows the runtimes of six migration results with six operator lengths. This figure shows that shorter operators are computationally more efficient than long operators. The decrease in run times for operators less than 25 points is smaller than expected based on runtimes with operators of greater lengths. This might be due to numerical overhead (e.g. calculating operator tables, memory allocation, looping through depth steps, looping through frequencies...etc).

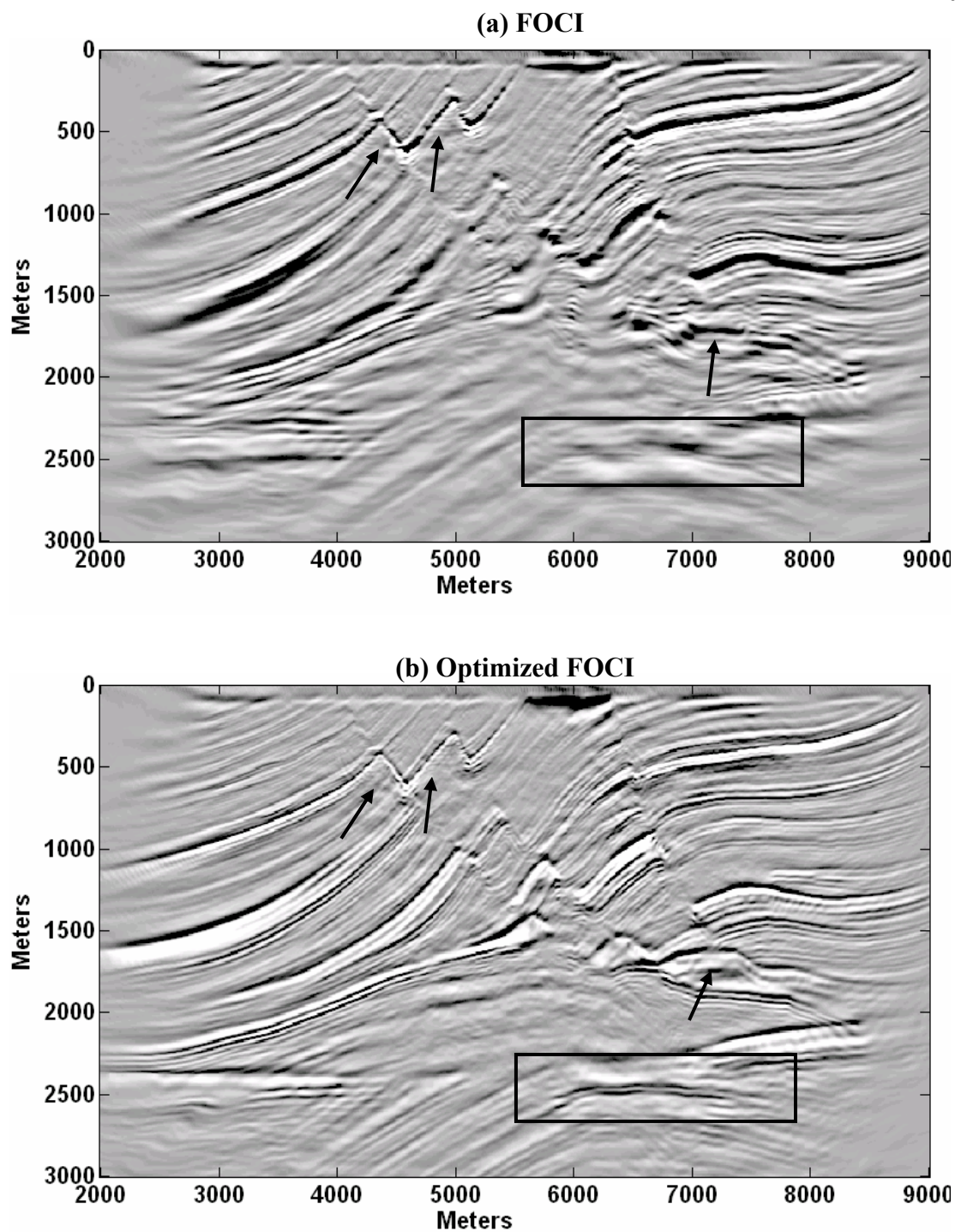


Figure 4-11. PSDM images of the Marmousi dataset, where (a) shows the result of the old FOCI algorithm, and (b) shows the result of the optimized algorithm. The box contains the target area, and the arrows show some comparison areas. The operator length is 15 points.

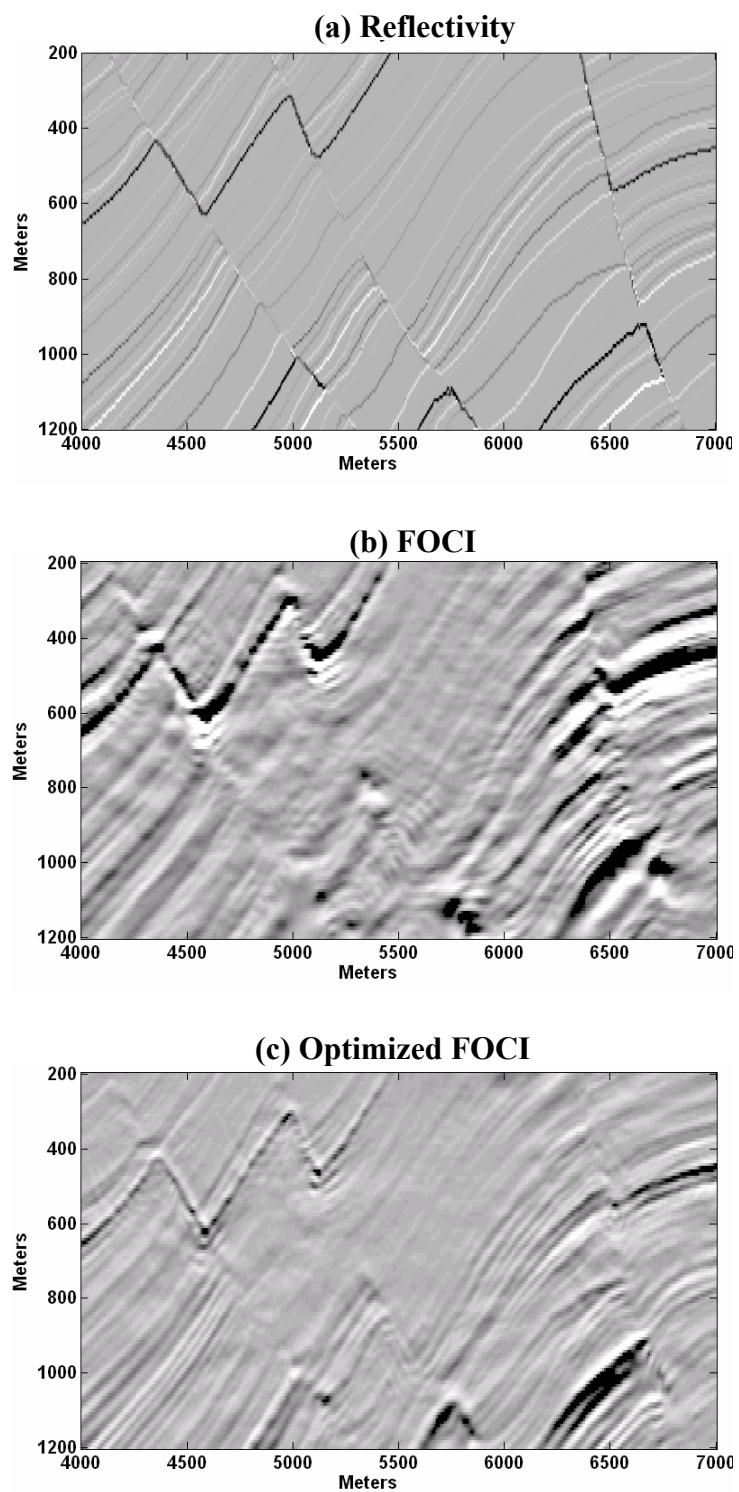


Figure 4-12. Close-up views of the shallow central sections of Figures 3-15a, 4-11a, and 4-11b.

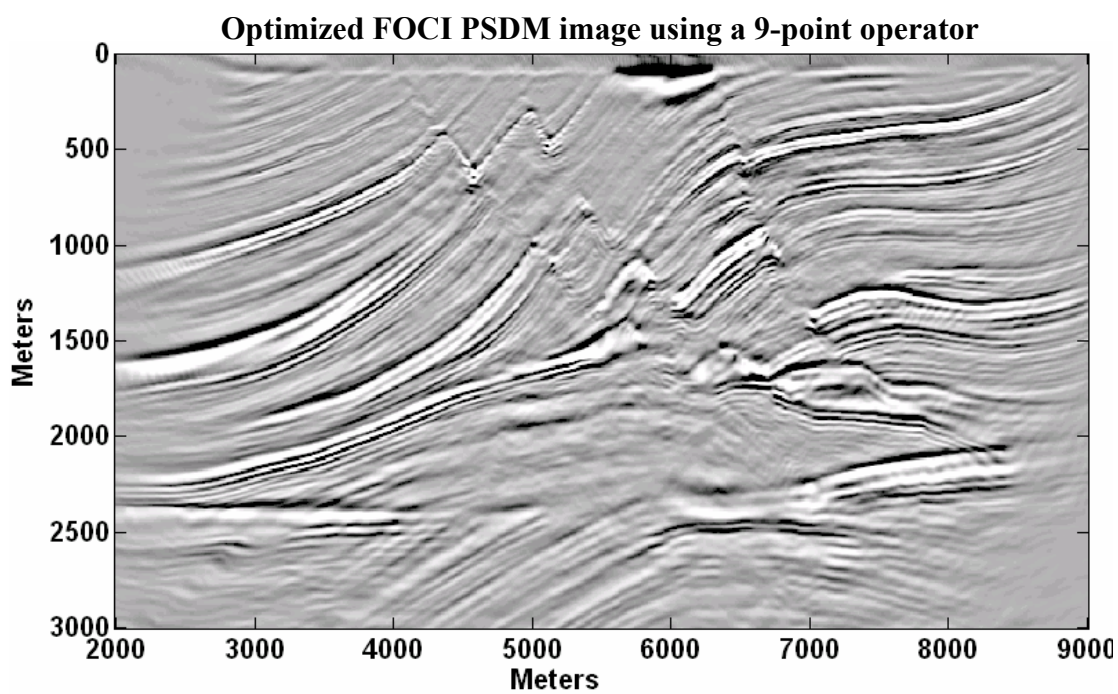


Figure 4-13. PSDM image obtained with the optimized FOCI algorithm with a 9-point operator.

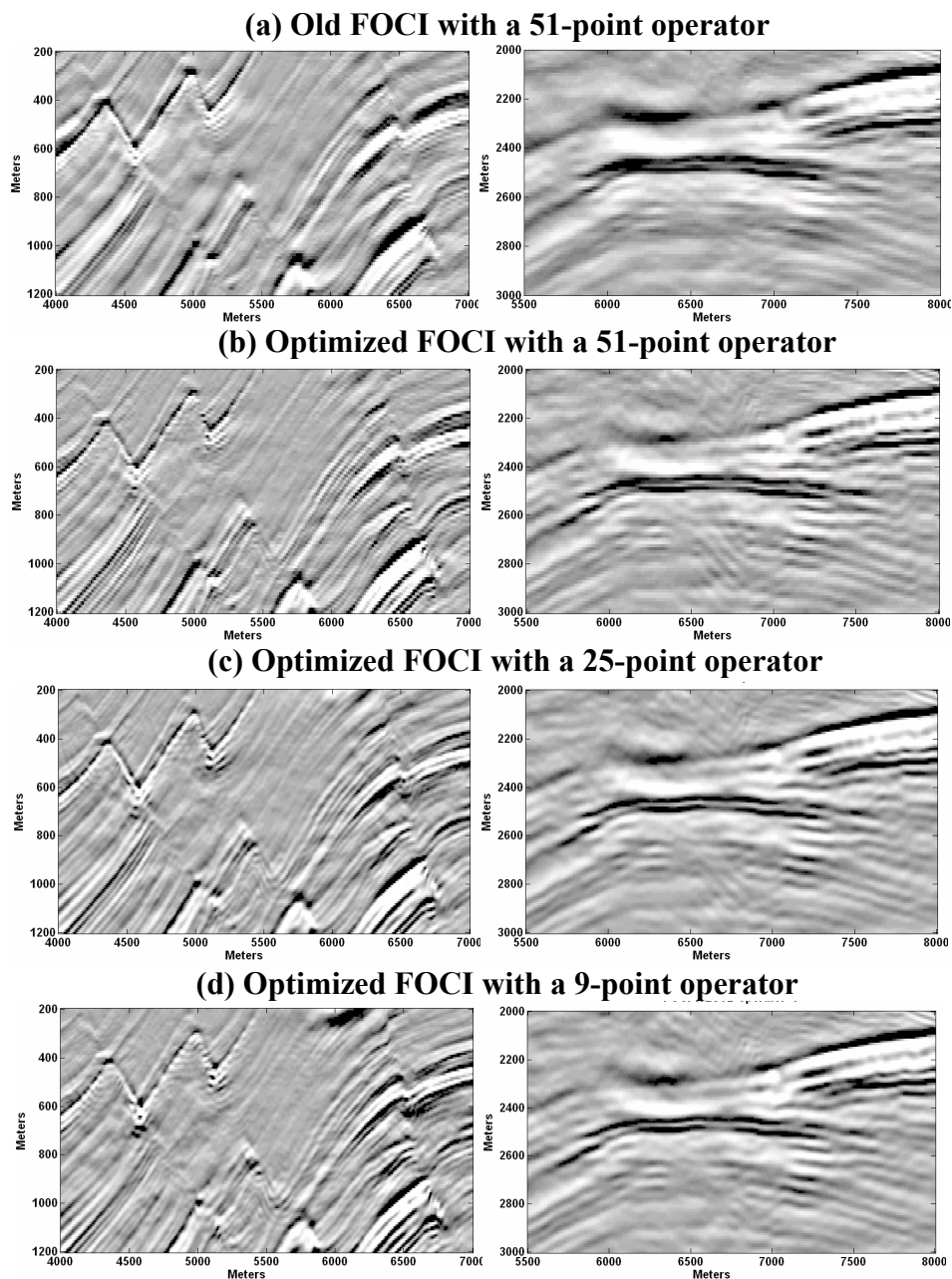


Figure 4-14. Comparisons of FOCI before and after the optimization at zoomed sections with various operator lengths, where (a) was obtained with the old FOCI with an operator length of 51 points, (b) was obtained with the optimized FOCI using an operator length of 51 points, (c) was obtained with the optimized FOCI using an operator length of 25 points, and (d) was obtained with the optimized FOCI using an operator length of 9 points.

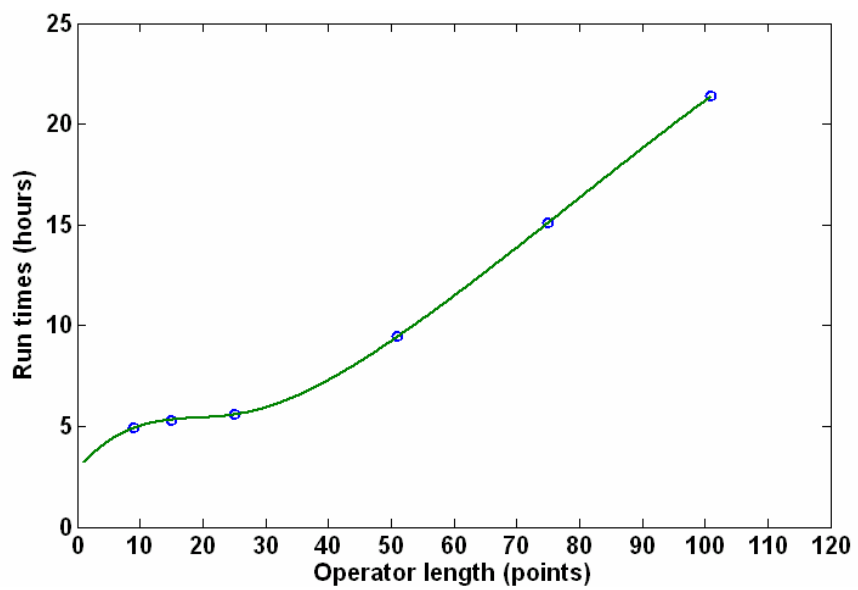


Figure 4-15. Runtimes versus operator lengths.

4-4 CHAPTER SUMMARY

Least-squares methods can be classified into three major categories: unweighted least-squares followed by a windowing function applied in the space-frequency domain; weighted least-squares using a smooth transition function connecting the wavefield and evanescent regions; and weighted least-squares using a transition band for the transition region. The transition band approach can be used to design wavefield extrapolators that remain practically stable in a recursive scheme. Further, results obtained with this approach are comparable to the WLSQ.

The forward operator and conjugate inverse (FOCI) algorithm uses Wiener filtering to design wavefield extrapolators that remain practically stable in a recursive scheme. The old algorithm used suboptimal windowing and thus required long operators to generate good images. Using a weighted least-squares approach to replace the Hanning window in the old design makes the algorithm more efficient.

With the optimized algorithm, it is possible to design short operators that remain practically stable in a recursive scheme. Further, this enhancement eliminates the need for dual tables for evanescent filtering since the operator can attenuate the evanescent energy very effectively.

CHAPTER 5: EXPLICIT WAVEFIELD EXTRAPOLATION FROM TOPOGRAPHY

Downward-continuation methods assume that extrapolation takes place between two horizontal surfaces, but most land surveys are acquired over irregular surfaces. Wavefield extrapolation of such data is difficult to formulate and accomplish. Further, using simple time-shifts to shift the data to a flat horizontal surface is inaccurate for nonvertically travelling waves (Gray, 1997). Migration will inaccurately position the reflectors in depth.

Bevc (1997) applied wave-equation datuming (recorded data are upward-continued to a surface (datum) that equals the highest elevation) prior to migration, so that downward-continuation methods can start from a flat surface. This approach is more accurate than using time-shifts, but requires more computational effort.

A more efficient approach is the “zero-velocity layer” method (Beasley and Lynn, 1992; Gray, 1997) (next section). Although this approach is less expensive than wave-equation datuming, it adds more data to extrapolate. Margrave and Yao (2000) used a laterally-variable depth step in the nonstationary phase-shift (NSPS) algorithm to downward-continue zero-offset data directly from topography. This approach is more efficient than the other methods because it does not require processing prior to migration.

Most publications about the zero-velocity layer only address the zero-offset case and never address the prestack case.

I show an implementation of the zero-velocity layer approach in prestack depth migration is shown (S. Gray, personal communication, 2006) (section 5-1). I also show the extension of the laterally-variable depth step approach of Margrave and Yao (2000) to explicit wavefield extrapolation methods using shot profile and source-receiver migration schemes (sections 5-2 and 5-3). Applications of these approaches are shown using a synthetic dataset.

5-1 THE ZERO-VELOCITY LAYER APPROACH

Beasley and Lynn (1992) introduced an efficient and accurate technique to downward-continue data from topography called the “zero-velocity” approach. In Beasley and Lynn (1992), Lynn et al. (1993), MacKay (1994), and Gray (1997), the use of the zero-velocity layer has resulted in dramatic improvements in image quality over conventional processing.

5-1.1 Defining the geometry

Let’s consider the geometry shown in Figure 5-1, where the datum plane is taken at $z = 0$, and the topography is given by $z = h(x)$. Here, $h(x)$ is a positive function giving the topographic elevation below the datum. Using this geometry, the upgoing wavefield can be defined as

$$U^-(x_s, x, h(x), \omega) \equiv \text{surface recorded data}, \quad (5.1)$$

where x_s is the shot coordinate, s is an integer shot index ranging from 1 to S (number of shots), and x is the transverse coordinate.

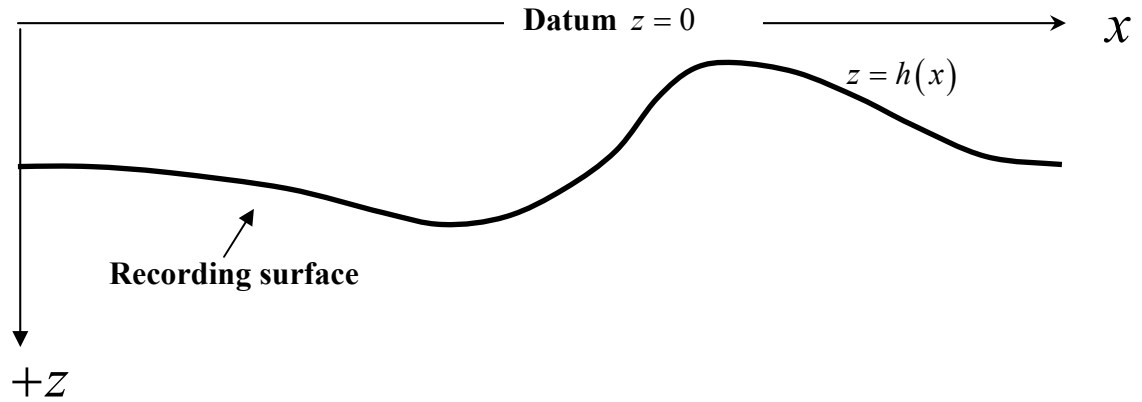


Figure 5-1. The coordinate system and datum plane used in the description.

5-1.2 Time-shifting the data to a flat datum

The implementation of this approach in the prestack domain, from a shot profile perspective (section 2-2), can be achieved by time-shifting the recorded data or the upgoing wavefield, $U^-(x_s, x, h(x), \omega)$, to the flat datum at $z = 0$. A temporal shift in the time domain is a linear phase-shift in the frequency domain. So time-shifting the upgoing wavefield in the frequency domain can be described as

$$U^-(x_s, x, z = 0, \omega) = U^-(x_s, x, h(x), \omega) \exp(i\omega t_e(x)). \quad (5.2)$$

The time-shifts can be calculated using

$$t_e(x) = -\frac{h(x)}{V_o}, \quad (5.3)$$

where V_o is the velocity of the medium between the topography and the datum, a user-defined parameter. From section 2-2, the downgoing wavefield, $D^+(x_s, x, h(x_s) + \Delta z, \omega)$, that is used in shot profile migration, can be modeled using the Green function. It has also to be time-shifted, but in opposite direction according to

$$D^+(x_s, x, z_d(x_s) + \Delta z, \omega) = D^+(x_s, x, h(x_s) + \Delta z, \omega) \exp(-i\omega t_e(x_s)), \quad (5.4)$$

where

$$z_d(x_s) = 2h(x_s). \quad (5.5)$$

Applying a time-shift to the downgoing wavefield may cause it to start at a negative time (equation (5.4)). This makes sense because during extrapolation, the downgoing and upgoing wavefields are extrapolated in opposite directions, where the upgoing wavefield is backward extrapolated, and the downgoing wavefield is forward modeled.

5-1.3 Special extrapolation between the topography and datum

The time-shifted wavefields have now a regular grid on which downward-continuation algorithms can operate. However, a special wavefield extrapolator must be used between the datum and the recording surface — that is, the operator has to be modified in such a way as to undo the effect of the time-shifts. To illustrate this concept, let's decompose the phase-shift operator (section 2-1)

$$\hat{W} = \exp\left(i\Delta z \sqrt{k^2 - k_x^2}\right), \quad (5.6)$$

into a thin-lens²⁰ term defined as

$$W_s = \exp(i\Delta z k_s) \quad (5.7)$$

and a focusing term²¹ defined as

$$\hat{W}_f = \exp \left\{ i\Delta z k_s \left[\sqrt{1 - \left(\frac{k_x}{k_f} \right)^2} - 1 \right] \right\}, \quad (5.8)$$

where

$$k = \frac{\omega}{V}, \quad (5.9)$$

$$k_s = \frac{\omega}{V_s}, \quad (5.10)$$

and

$$k_f = \frac{\omega}{V_f}. \quad (5.11)$$

The velocity terms used in equations (5.10) and (5.11) are defined as

$$V_s = \begin{cases} V_o & \text{for } (x, z) \text{ above the} \\ & \text{recording surface} \\ V(x, z) & \text{otherwise} \end{cases} \quad (5.12)$$

and

²⁰ This thin-lens term is sometimes called the static term.

²¹ This focusing term is sometimes called the diffraction or mixing term.

$$V_f = \begin{cases} 0 & \text{for } (x, z) \text{ above the} \\ & \text{recording surface} \\ V(x, z) & \text{otherwise} \end{cases}, \quad (5.13)$$

where $V(x, z)$ is the background velocity model that best approximates the true velocity field. Thus, using the reference velocity, V_o , in the thin-lens term removes the time-shifts that were applied to the data, and using a zero-velocity in the focusing term prevents any lateral propagation or trace mixing during the extrapolation between the recording surface and the datum. The wavefield extrapolator in the space-frequency domain can be expressed as

$$\tilde{W} = W_s \tilde{W}_f, \quad (5.14)$$

where \tilde{W}_f is a compactly supported approximation to the inverse Fourier transformation of \hat{W}_f over the transverse wavenumber²².

When the depth level of the extrapolation reaches the recording surface at a given lateral position, x , the velocities in equations (5.12) and (5.13) revert to the background velocity model, and migration can be carried out as described in section 2-2.

²² Chapters 3 and 4 describe different methods of designing practically stable operators.

5-1.4 Application of the zero-velocity approach using the Aruma dataset

The 2D Aruma dataset is used to test the zero-velocity layer approach. This dataset was generated at Saudi Aramco using an acoustic finite-difference modeling program. The dataset consists of 626 shots. The maximum source-receiver lateral separation, offset, of each shot is 3000 m. The acquisition geometry has a roll on and a roll off at the beginning and the end of the line, where the number of receivers per shot profile ranges from 188 to 375 depending on the lateral position of the shot profile. The source and receiver intervals are 16 m. Prior to migration, each shot was interpolated to an 8-m trace spacing to avoid spatial aliasing. The operator length used in this test is 25 points, designed using the optimized FOCI algorithm (section 4-3).

A vertical exaggeration of the elevation profile of this dataset is shown in Figure 5-2, which shows the strong topographic variation. Figure 5-3 shows the reflectivity of the dataset obtained from the velocity model²³. Figure 5-4 shows the velocity model, and Figure 5-5 shows the result after extracting the zero-offset (source-receiver offset = 0) trace from each shot profile. Due to the rough topography, the reflections are greatly distorted, and they do not resemble the geology of the subsurface.

²³ To generate a reflectivity image, I assumed the density to be constant. The result was then convolved with a Ricker wavelet with 25 Hz as the dominant frequency.

Figure 5-6a shows the modeled downgoing wavefield to the depth level, $h(x_s) + \Delta z$, and Figure 5-6b shows the downgoing wavefield at the depth level, $z_d + \Delta z$ — that is, after applying the time-shift of the source, $-t_e(x_s)$, calculated using equation (5.3). Note that after applying the time-shift, the downgoing wavefield starts at a negative time.

Figure 5-7a shows the upgoing wavefield as recorded from the topography, and Figure 5-7b shows the upgoing wavefield at the datum, $z = 0$ — that is, after applying the calculated time-shifts using equation (5.3). As a result, the upgoing wavefield is now delayed in time.

Figure 5-8 shows the same shot gather in Figure 5-7, but downward-continued to a depth level=500 m, which is well below the topography. Thereby most of the elevation statics have been removed. Figure 5-9 shows a single imaged shot gather, and Figure 5-10 shows the PSDM image using the zero-velocity approach. The cross-correlation imaging condition was used to obtain the result (section 2-2). This approach was effective in handling data recorded from an irregular surface. The shallow channels are resolved and the deep reflectors do not suffer from the elevation related statics.

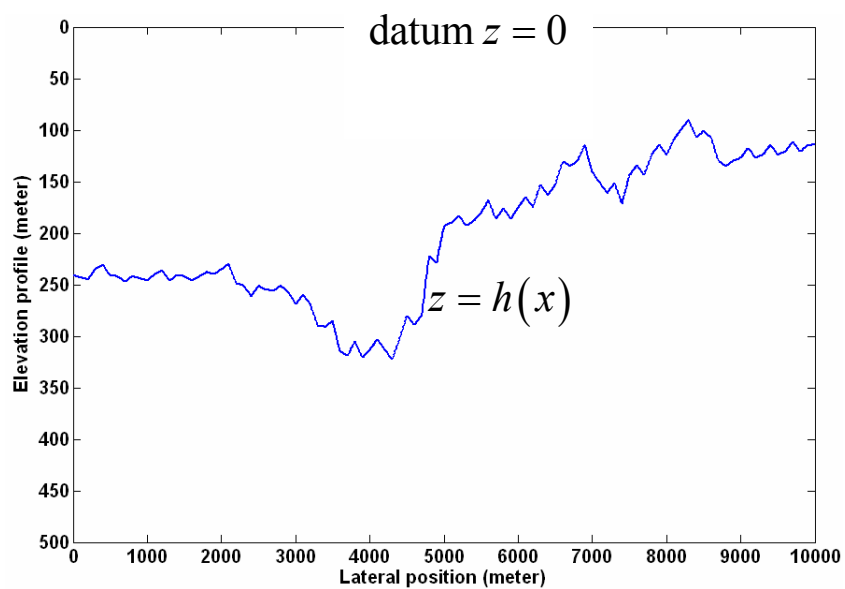


Figure 5-2. Elevation profile of the Aruma dataset.

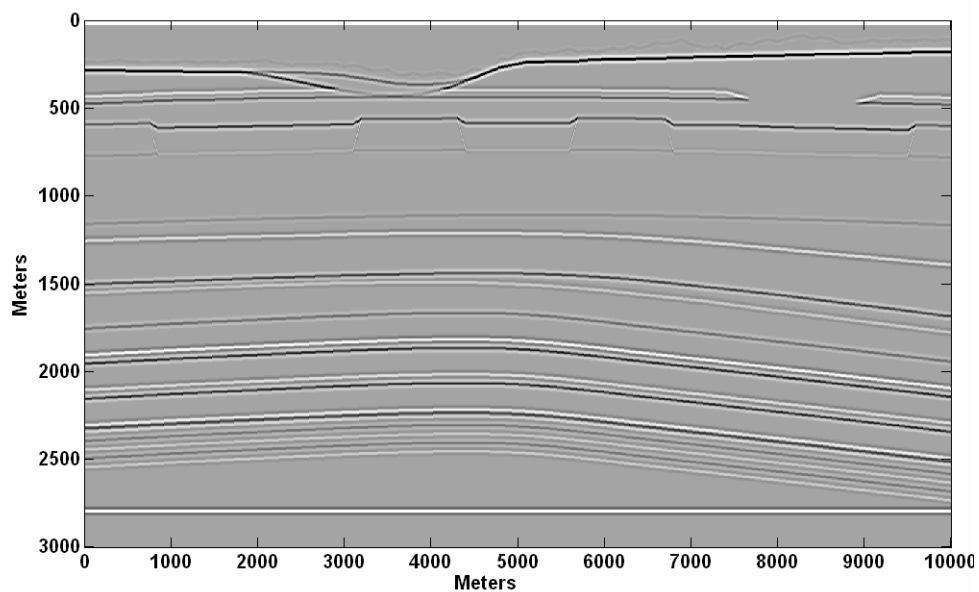


Figure 5-3. The reflectivity of the Aruma dataset.

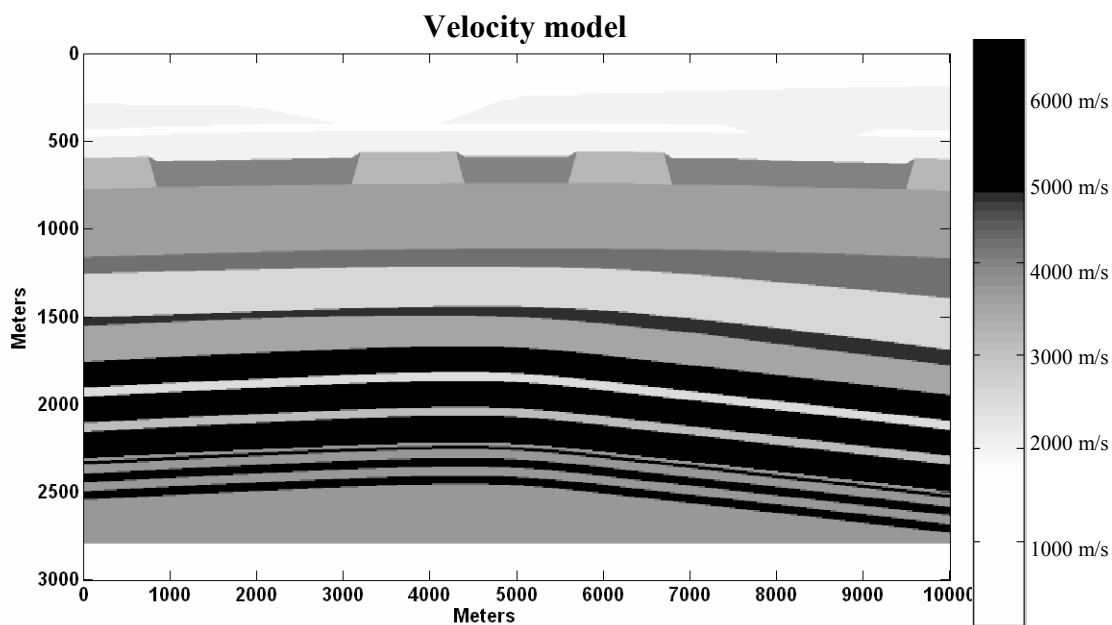


Figure 5-4. The velocity model of the Aruma dataset.

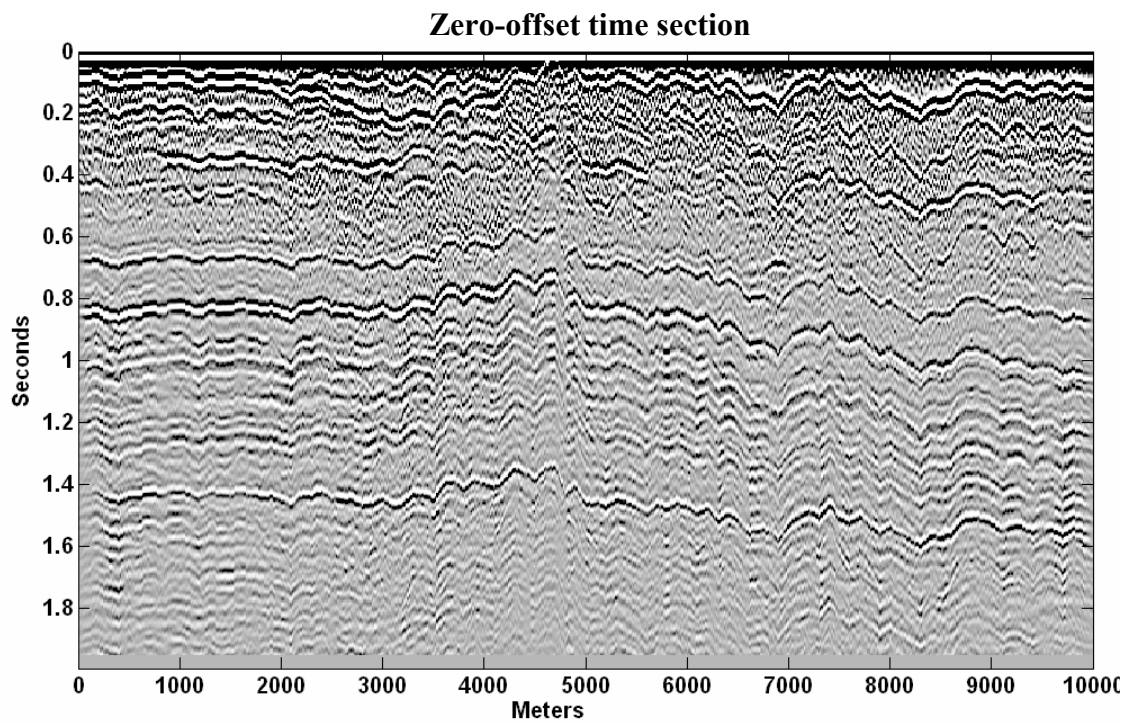


Figure 5-5. The zero-offset time section of the Aruma dataset.

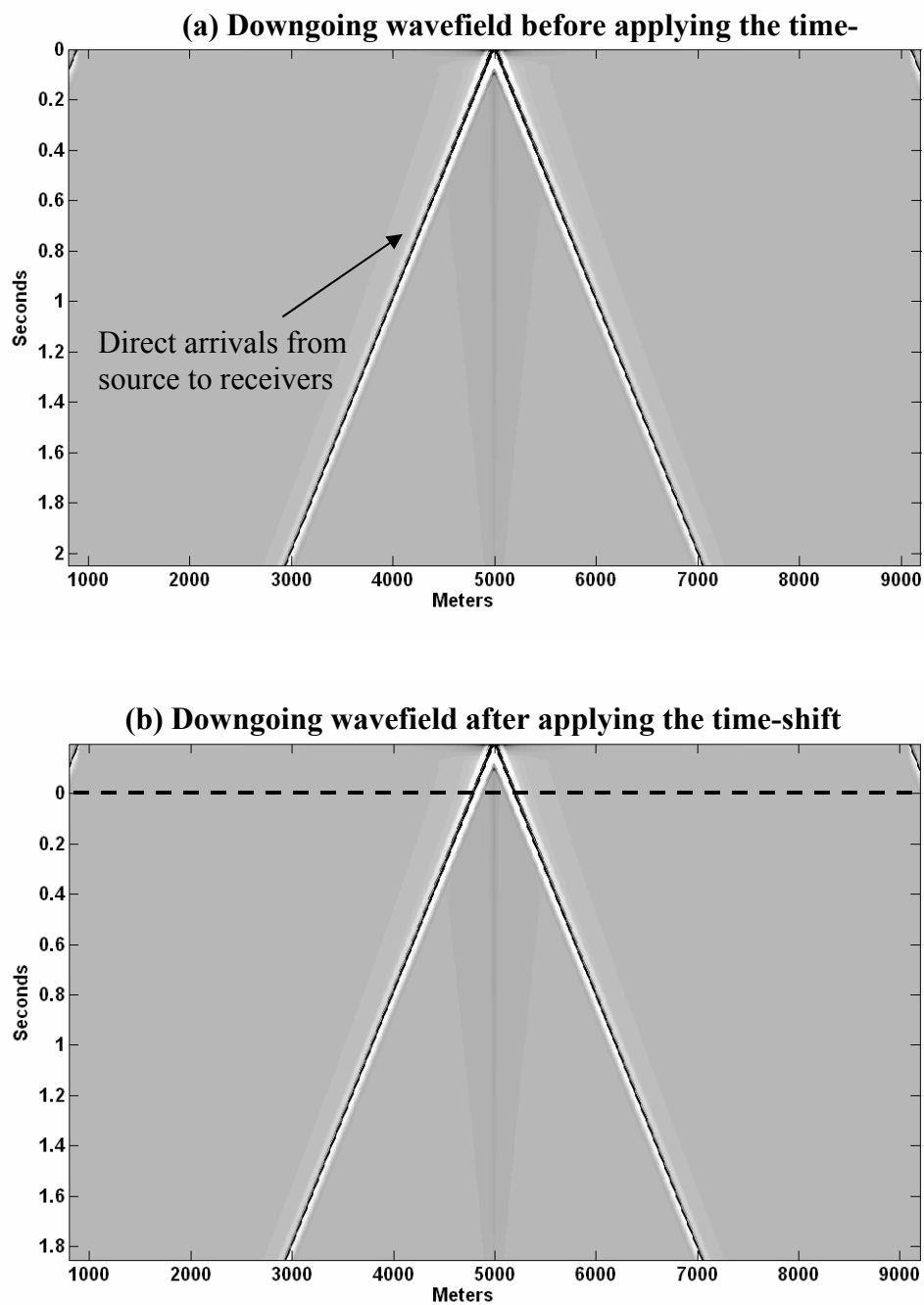


Figure 5-6. The modeled source wavefield, (a) before applying the source time-shift, and (b) after applying it, where the dashed line indicates the zero time line.

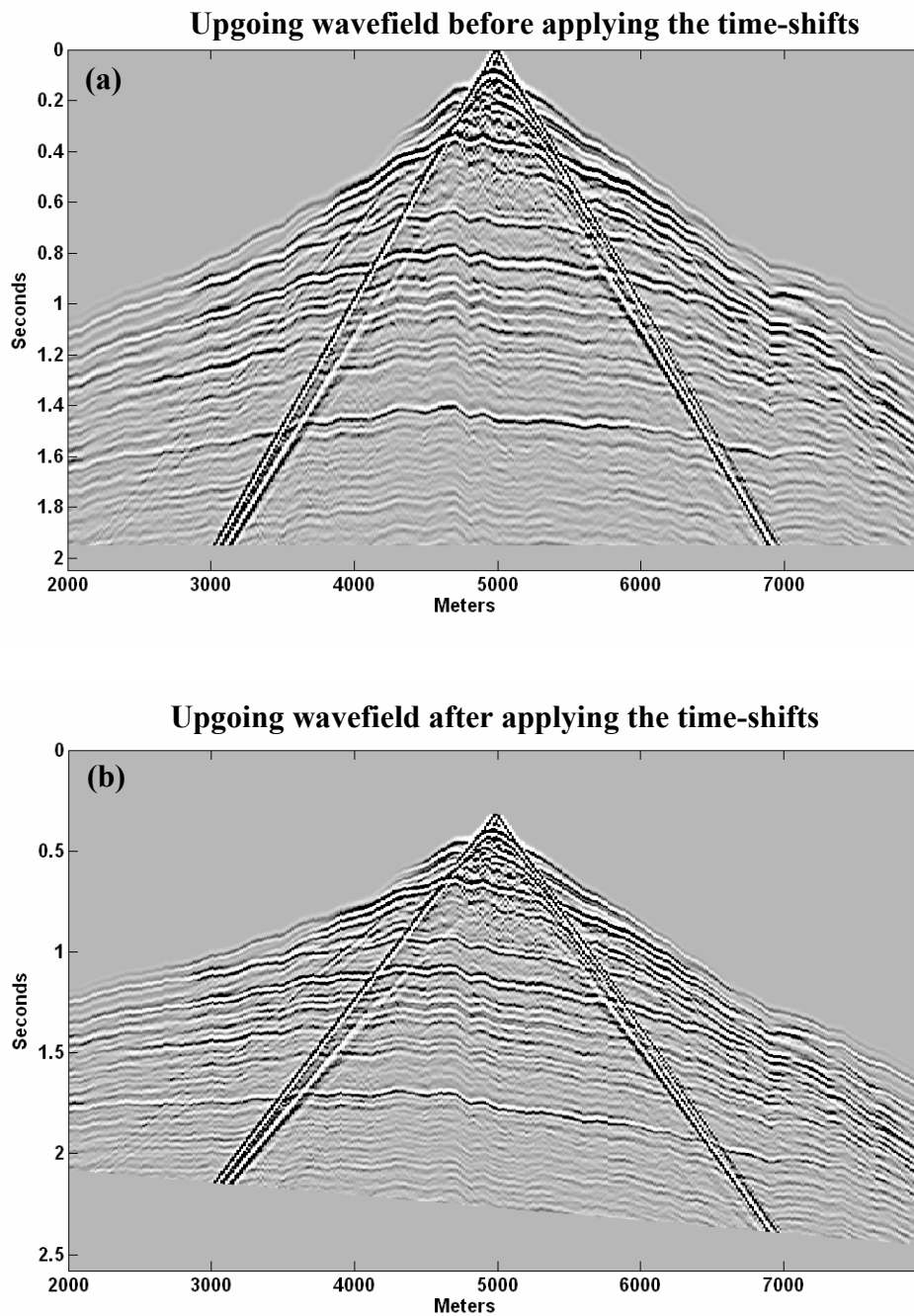


Figure 5-7. Shot profile at a lateral position of 5000 m (a) before applying the static shifts, and (b) after applying them. The reference velocity is $V_o = 1000$ m/s.

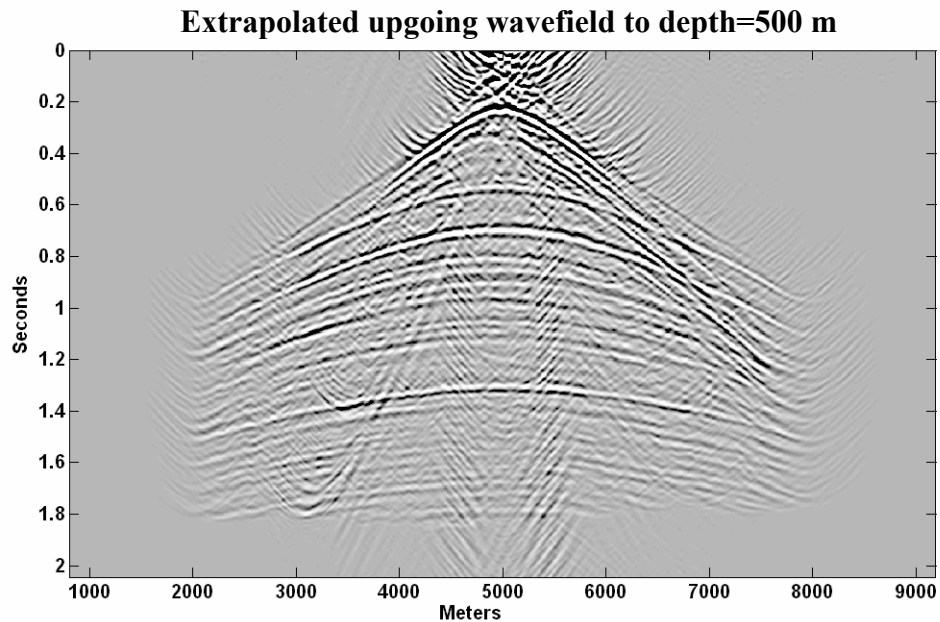


Figure 5-8. The same shot profile as in Figure 5-6 but extrapolated to a depth of 500 m.

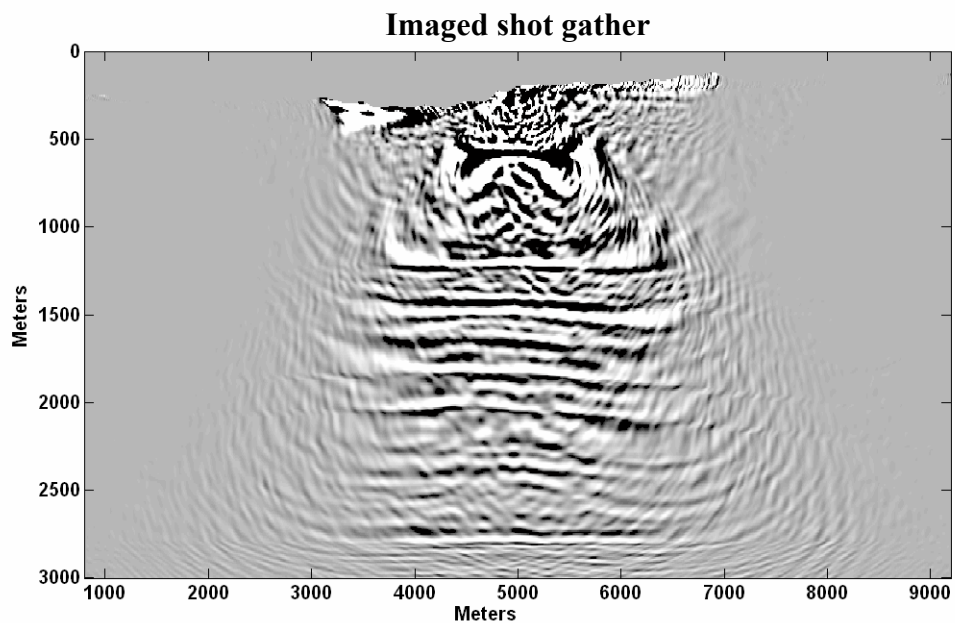


Figure 5-9. Single imaged shot profile that was shown in Figures 5-6 and 5-7.

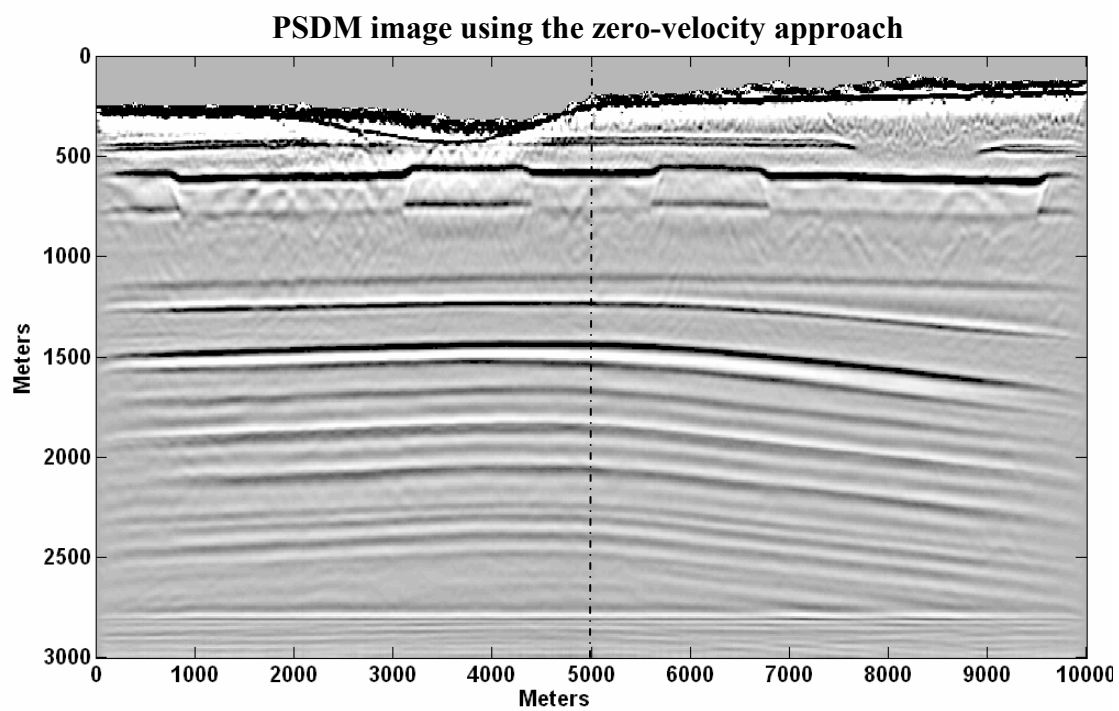


Figure 5-10. The PSDM image of the Aruma dataset using the zero-velocity approach, where the dashed line indicates the lateral position of the shot profile that was shown in Figures 5-6 - 5-8.

5-2 SOURCE-RECEIVER MIGRATION FROM TOPOGRAPHY WITH A LATERALLY VARIABLE DEPTH STEP

From section 2-2, in shot profile migration, each shot can be imaged independently, and the PSDM image is formed by the superposition (stacking) of the individually imaged gathers. In this section, another migration method, called source-receiver migration, is reviewed. This method is based on the concept of survey sinking (Claerbout, 1985). At each depth level, the downward-continued shot gathers are sorted into receiver gathers, which are downward-continued to the same depth level. The extrapolated data are equivalent to the data that would have been recorded if all sources and receivers were placed on that level. The reflectivity is then estimated by invoking the zero-time and zero-offset imaging conditions, which will be described shortly.

Source-receiver extrapolation can be implemented by applying a cascade of operators to the surface recorded data, $U^-(x_r, x_s, h(x), \omega)$, according to

$$U^-(x_r, x_s, N\Delta z, \omega) = \left[\left(\prod_{n=1}^N \mathbf{W}^r_{n\Delta z} \right) \left(\prod_{n=1}^N \mathbf{W}^s_{n\Delta z} \right) U_o^- \right] (x_r, x_s, N\Delta z, \omega), \quad (5.15)$$

where

$$U_o^- \equiv U^-(x_r, x_s, h(x), \omega), \quad (5.16)$$

$N\Delta z$ is the maximum depth of interest, x_r is the receiver coordinate, and r is an integer receiver index ranging from 1 to R (number of receivers). The cascade of operators

$\prod_{n=1}^N \mathbf{W}^s_{n\Delta z}$ operates on the source axis to downward-continue the receivers according to

$$\prod_{n=1}^N \mathbf{W}_{n\Delta z}^s = \mathbf{W}_{N\Delta z}^s \circ \mathbf{W}_{(N-1)\Delta z}^s \circ \dots \circ \mathbf{W}_{\Delta z}^s, \quad (5.17)$$

and the cascade of operators $\prod_{n=1}^N \mathbf{W}_{n\Delta z}^r$ operates on the receiver axis to downward-continue the sources according to

$$\prod_{n=1}^N \mathbf{W}_{n\Delta z}^r = \mathbf{W}_{N\Delta z}^r \circ \mathbf{W}_{(N-1)\Delta z}^r \circ \dots \circ \mathbf{W}_{\Delta z}^r. \quad (5.18)$$

" \circ " denotes operator composition, and $\mathbf{W}_{\Delta z}^s U_o^-$ can be expressed as

$$\left(\mathbf{W}_{\Delta z}^s U_o^- \right) (x_r, x_s, \Delta z, \omega) = \frac{1}{2\pi} \int_{\mathbb{R}} U^- (x'_r, x_s, h(x), \omega) \Theta (x'_r - x_r, k(x_r), \Delta \tilde{z}) dx'_r, \quad (5.19)$$

and $\mathbf{W}_{\Delta z}^r U_o^-$ can be expressed as

$$\left(\mathbf{W}_{\Delta z}^r U_o^- \right) (x_r, x_s, \Delta z, \omega) = \frac{1}{2\pi} \int_{\mathbb{R}} U^- (x_r, x'_s, h(x), \omega) \Theta (x'_s - x_s, k(x_s), \Delta \tilde{z}) dx'_s. \quad (5.20)$$

Downward-continuation from topography can be accomplished by using the laterally variable depth step approach of Margrave and Yao (2000) in defining the kernel, Θ , of equations (5.19) and (5.20), according to

$$\Theta (x - x', k(x), \Delta \tilde{z}) = \begin{cases} \delta (x - x'); & \gamma (x') < 0 \\ \tilde{W} (x - x', k(x), \Delta \tilde{z}); & \text{otherwise} \end{cases}, \quad (5.21)$$

where

$$\Delta \tilde{z} = \begin{cases} \gamma (x); & 0 < \gamma (x) < \Delta z \\ \Delta z; & \text{otherwise} \end{cases}, \quad (5.22)$$

and

$$\gamma(x) = n\Delta z - h(x). \quad (5.23)$$

In these equations, x' and x are the traverse coordinates at input and output, respectively, that can be either x_s or x_r depending on the axis of extrapolation. Also, \tilde{W} is the wavefield extrapolator that is compactly supported (section 2-5.1).

When the extrapolation level is above the surface elevation, $\gamma < 0$ the convolution with a delta function returns the original wavefield²⁴. When the elevation of the output wavefield, however, falls between two extrapolation levels, $0 < \gamma < \Delta z$, then γ is used as the depth step to build the extrapolator. When the difference between the extrapolation depth level and the elevation of the input wavefield is equal to or greater than Δz , $\gamma \geq \Delta z$, then the operator is designed using Δz . Using equations (5.19) and (5.20) simultaneously allow source-receiver wavefield extrapolation to be implemented directly from an irregular surface. Once the extrapolation level is well below the lowest elevation, the same depth step can be used to build all extrapolators. The advantage of using the laterally variable depth step approach is to allow wavefield extrapolators to handle topographic variation.

Claerbout (1985) showed how source-receiver migration can be implemented by extrapolating one frequency at a time. Here, it is implemented by sorting the data into a

²⁴ Convolution with $\delta(x)$ is the identity operation.

matrix for each frequency. The rows of each matrix represent the receivers and columns represent the shots (Figure 5-11).

The matrices that correspond to the different frequencies can be extrapolated together or separately for one depth level. After each extrapolation, the image can be obtained by invoking the zero-offset and zero-time imaging conditions according to (Claerbout, 1985)

$$I(n\Delta z, x_r = x_s) = -\frac{1}{\pi} \int_0^{\infty} \text{diag} \left(U^-(x_r, x_s, n\Delta z, \omega) \right) d\omega. \quad (5.24)$$

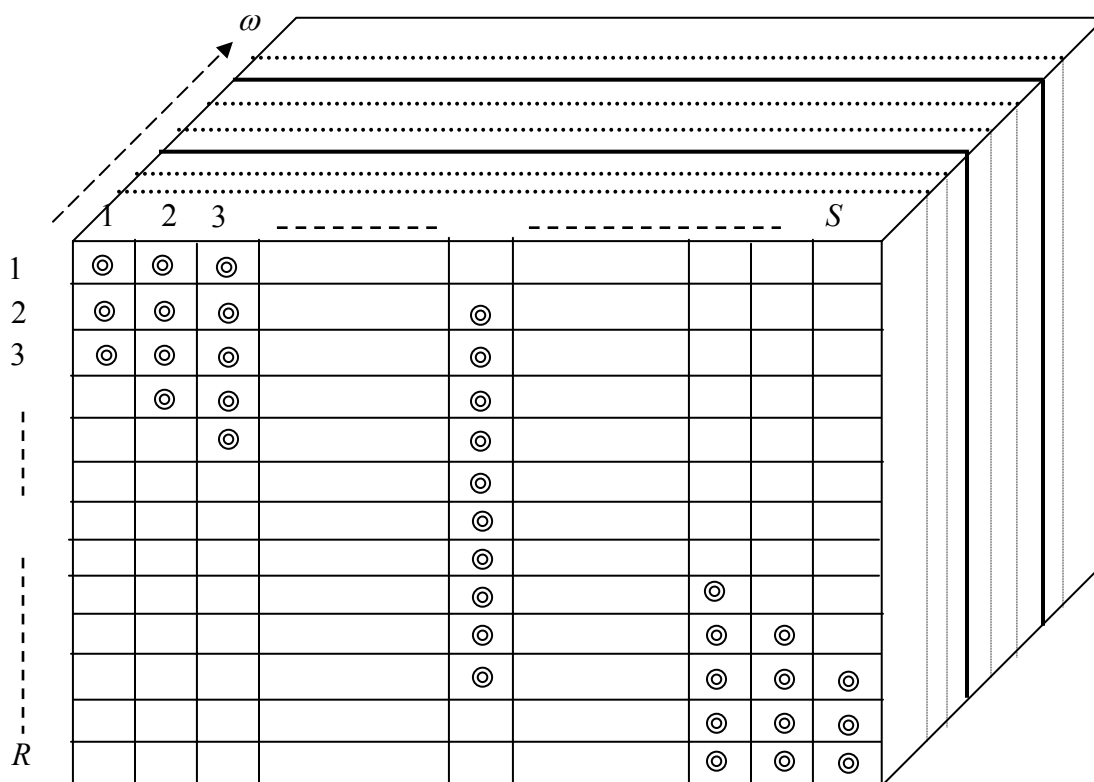


Figure 5-11. Source-receiver extrapolation can be performed by sorting the data into a matrix for each frequency, where the rows represent the receivers, the columns represent the shots, S is the number of shots, and R is the number of receivers.

Figure 5-12 shows the PSDM image using this approach. The deep reflectors are imaged to the correct depth, and do not suffer from any static distortions. The shallow channels are also imaged where they do not have any static problems due to topography. A 25 point operator, designed using the optimized FOCI algorithm (section 4-3), was used to obtain this result.

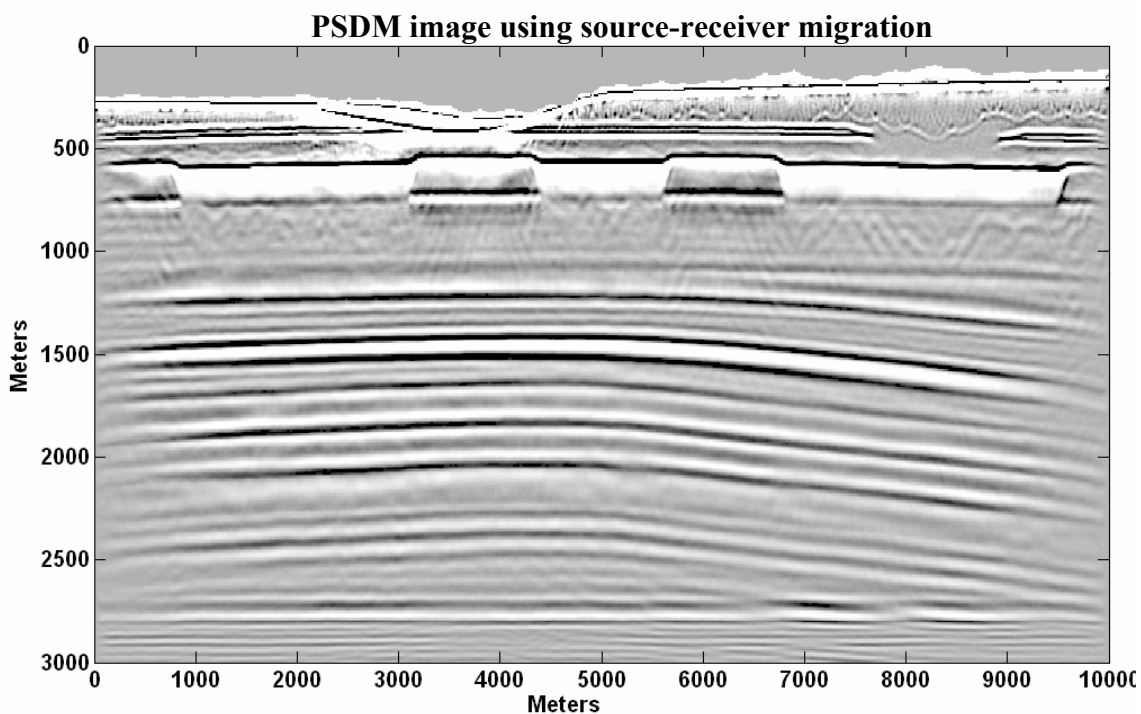


Figure 5-12. The PSDM image of the Aruma dataset using source-receiver migration with the laterally variable depth step approach.

5-3 SHOT PROFILE MIGRATION FROM TOPOGRAPHY WITH A VARIABLE DEPTH STEP

Shot profile migration can also be performed directly from topography using downward-continuation methods without using the zero-velocity layer approach, or the wave-equation datuming approach. It can be carried out in a similar fashion that was followed in the previous section to perform source-receiver downward-continuation from topography: that is, by using laterally variable depth steps in the extrapolators. In shot profile migration (section 2-2), two wavefields are used: the upgoing wavefield, U^- , and the downgoing wavefield, D^+ . Downward-continuing the upgoing wavefield to the first depth level, with respect to the datum, $z = 0$, can be expressed as

$$\left(W_{\Delta z} U_o^-\right)(x_s, x, \Delta z, \omega) = \frac{1}{2\pi} \int_{\mathbb{R}} U_o^-(x_s, x, h(x), \omega) \Theta(x - x', k(x), \Delta \tilde{z}) dx', \quad (5.25)$$

where U_o^- was defined in equation (5.16). Similarly, forward modeling the downgoing wavefield to the first depth level can be expressed as

$$\left(W_{\Delta z} D_o^+\right)(x_s, x, \Delta z, \omega) = \frac{1}{2\pi} \int_{\mathbb{R}} D_o^+(x_s, x, h(x_s), \omega) \Theta^*(x - x', k(x), \Delta \tilde{z}) dx', \quad (5.26)$$

where Θ was defined as in equation (5.21), and $*$ is the complex conjugate, D_o^+ is the modeled source wavefield at the surface that can be defined using the 2D Green function

$$D_o^+(x_s, x, h(x_s), \omega) = G(x_s, x, h(x_s), \omega), \quad (5.27)$$

where the Green function can be approximated by

$$G(x_s, x, h(x_s), \omega) \approx \frac{\sqrt{2\pi V_0 \tilde{r}} e^{i\omega \tilde{r}/V_0}}{\sqrt{-i\omega} 4\pi \tilde{r}}, \quad (5.28)$$

where

$$\tilde{r} = \begin{cases} \sqrt{(x_s - x)^2 + (h(x_s) - h(x))^2}; & x \neq x_s \\ 1; & x = x_s \end{cases} \quad (5.29)$$

where V_o is a reference velocity²⁵. Equation (5.27) is used to simulate a downgoing wavefield that has the same topographic statics as the upgoing wavefield. Further, using Θ in equations (5.25) and (5.26) allows the extrapolators to handle lateral velocity and topographic variations. For each output point, the extrapolator can be built using the velocity of that point and the depth step that accounts for the difference between the extrapolation depth level and the recording surface.

This approach was tested on the Aruma dataset. Figure 5-13a shows the upgoing wavefield as recorded from topography, and Figure 5-13b shows the result after downward-continuing it to a depth level of 500 m, where each shot was interpolated to 8 m spacing prior to migration, and an operator length of 25 points, designed with the optimized FOCI algorithm (section 4-3), was used. Note that most of the elevation related statics have been removed after the extrapolation below the topography. Figure 5-14 shows the PSDM image of the same shot shown in Figure 5-13. The PSDM image (Figure 5-15) is formed by stacking the imaged shot gathers (Figure 5-14), where it shows that this approach is effective in extrapolating from topography without the need to use the zero-velocity layer approach or wave-equation datuming, both of which are

²⁵ This velocity can be measured from the direct arrival on a shot profile.

computationally more expensive. The channels are well resolved and the continuity of the deep reflectors indicates that surface-related statics were removed.

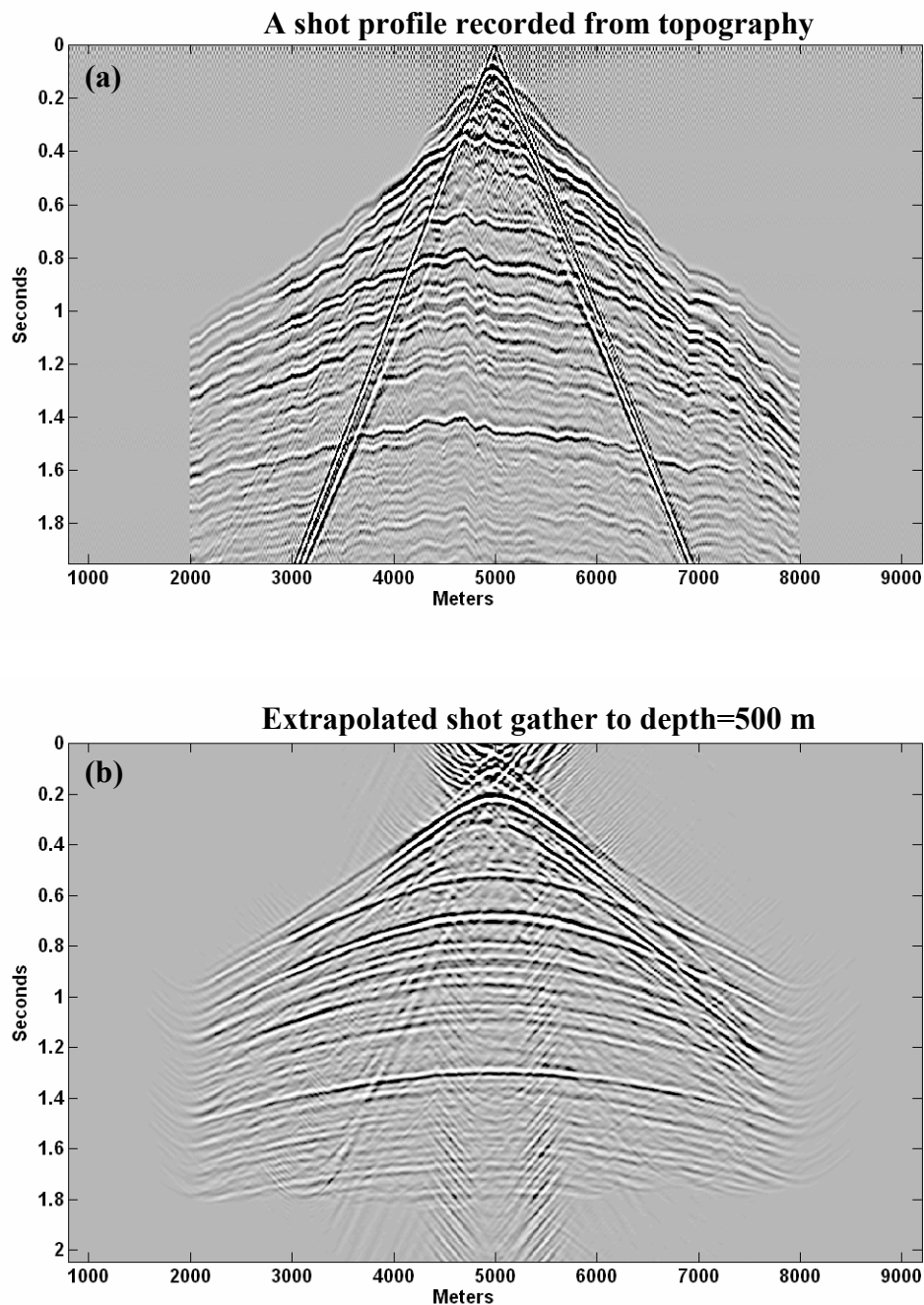


Figure 5-13. Shot gather at a lateral position= 5000 m (a) as recorded from topography, and (b) after downward-continuation to a depth level of 500 m.

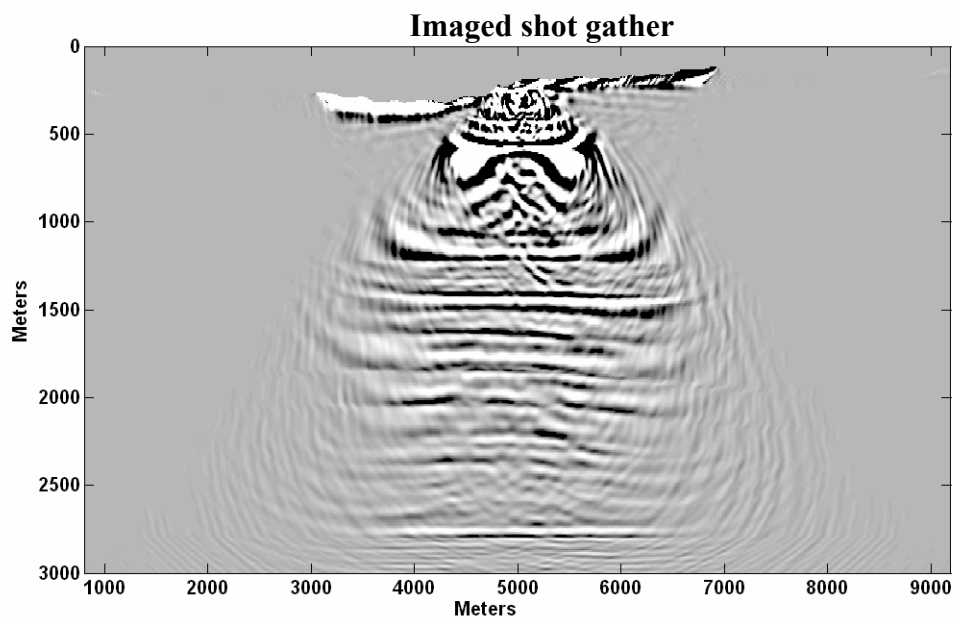


Figure 5-14. Imaged shot gather that was shown in Figure 5-13.

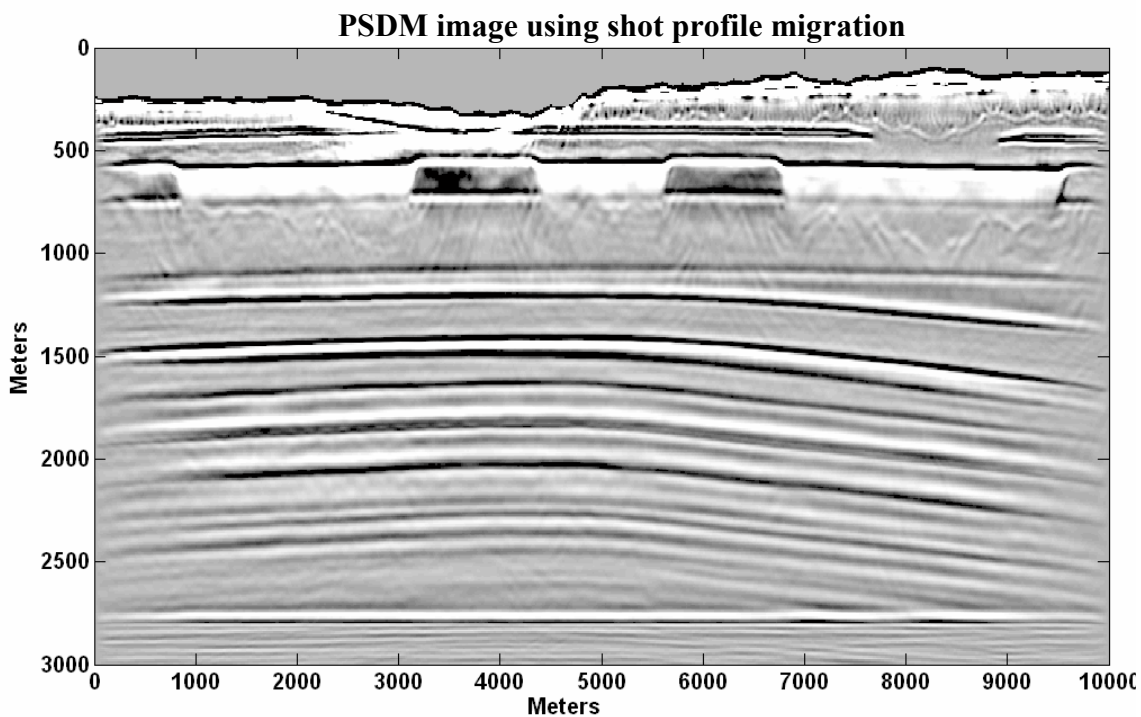


Figure 5-15. The PSDM image using the shot profile migration with a laterally variable depth approach.

5-4 CHAPTER SUMMARY

Although downward-continuation methods can better handle lateral velocity variations than ray-based methods, they are also generally computationally more expensive.

Further, downward-continuing data recorded from topography makes them even more expensive. For example, using wave-equation datuming to upward-continue the data to a datum equal to the highest elevation prior to migration is a computationally intensive process and adds more data to be extrapolated. The use of the zero-velocity layer approach also increases the computational cost of downward-continuation methods, although it is less expensive than wave-equation datuming.

In this chapter, one way to extend the zero-velocity approach to the prestack case using explicit wavefield extrapolation was shown. Also, wavefield extrapolation can be carried out directly from topography by building extrapolators that can handle both lateral velocity and topographic variations. This approach was shown using source-receiver and shot profile migrations. For large datasets, shot profile migration may be more attractive than source-receiver migration because each shot can be migrated separately instead of migrating all the shots and receivers at each depth level simultaneously, which requires a lot of disk space and memory.

CHAPTER 6: REFORMULATING THE RCA, DFA, AND CFP MVA DOMAINS INTO MATHEMATICAL HYPOTHESES

In previous chapters, it has been assumed that the velocity model is known. In reality, the velocity model is not known very well, and it needs to be estimated from the data. For a horizontally layered medium, conventional velocity analysis (see Yilmaz (1987) for a good discussion) can be used to build an accurate velocity model, whereas in the presence of a strong lateral velocity variation, conventional velocity analysis may fail (Yilmaz (1987); Al-Yahya (1989)).

Downward-continuation methods are very sensitive to velocity models (Berkhout, 1982; Yilmaz and Chambers, 1984; Claerbout, 1985; Al-Yahya, 1989; Deregowski, 1990; Liu and Bleistein, 1994; Varela et al., 1998). Using inaccurate velocity models in these methods can generate low quality images. Their sensitivity to velocity errors, however, makes them a good tool for velocity analysis. Using migration methods for estimating velocities is known as migration velocity analysis (MVA)²⁶.

Migration velocity analysis consists of the domain in which it is carried out, and the inversion scheme used to update the velocity model. There are different domains and inversions schemes for MVA. In this chapter some well known domains for migration velocity analysis are reformulated into mathematical hypotheses. These domains include

²⁶ Migration velocity analysis can be done by downward continuation or ray-based methods.

residual curvature analysis (RCA, Al-Yahya, 1989), depth focusing analysis (DFA, Faye and Jeannot, 1986), and the common focus point (CFP, Berkhout, 1997.a) analysis. This reformulation puts them in the same context so that they are easier to understand and compare. Further, restating them mathematically makes it easier to communicate them with other disciplines such as mathematics and physics.

6-1 RCA APPROACH

From section 2-2, the prestack depth migration (PSDM) image at a specific lateral position, x_0 , and depth, z , may be obtained by applying the cross-correlation imaging condition to the upgoing and downgoing wavefields at (x_0, z) , and summing over all the shots (Claerbout, 1985)

$$I(x_0, z = n\Delta z; V_m) = \sum_{x_s} \sum_{\omega} U^-(x_s, x_0, n\Delta z, \omega; V_m) D^+(x_s, x_0, n\Delta z, \omega; V_m)^*, \quad (6.1)$$

where $*$ is the complex conjugate and $V_m(x) \equiv V_m$ is some appropriate average of the background velocity model, $V_m(x, z)$, over

$$z \in [(n-1)\Delta z, n\Delta z], \quad (6.2)$$

where n is a positive integer such that $z = n\Delta z$ gives a particular depth of interest (section 2-2). Note that U^- , D^+ , and I explicitly depend on V_m .

6-1.1 The process of generating the common image gathers

The stack section, $I(x_0, z; V_m)$, does not have any prestack information; it only shows the average reflectivity as seen over the available incidence angles at (x_0, z) (de Bruin et al., 1990). One way to get prestack information is to use a common image gather (G_{ci}) defined as

$$G_{ci}(x_s, x_0, z; V_m) = \sum_{\omega} U^-(x_s, x_0, z, \omega; V_m) D^+(x_s, x_0, z, \omega; V_m)^* \exp(i\omega(\tau = 0)), \quad (6.3)$$

where it is explicitly noted that only the zero-lag of the cross-correlation lag, τ , has been used. Obviously,

$$I(x_0, z; V_m) = \sum_{x_s} G_{ci}(x_s, x_0, z; V_m), \quad (6.4)$$

that is, the PSDM image is the stack over x_s of the common image gathers (Figure 6-1b).

The residual curvature analysis (RCA, Al-Yahya, 1989) approach analyzes the curvatures²⁷ of reflection events on the common image gathers, where the migration velocity is acceptable if the difference between imaged depths from different offsets is minimal (Figure 6-1a) — that is, reflection events in the common image gathers are invariant with offset that can be defined as the lateral distance from the image point, x_0 , to the surface source location, x_s . In RCA, the prestack migrated data volumes contain flat events in the image gathers when the true velocity is used for migration (Yilmaz, 1987), which will be described shortly.

²⁷ Curvature here means either a smile or frown.

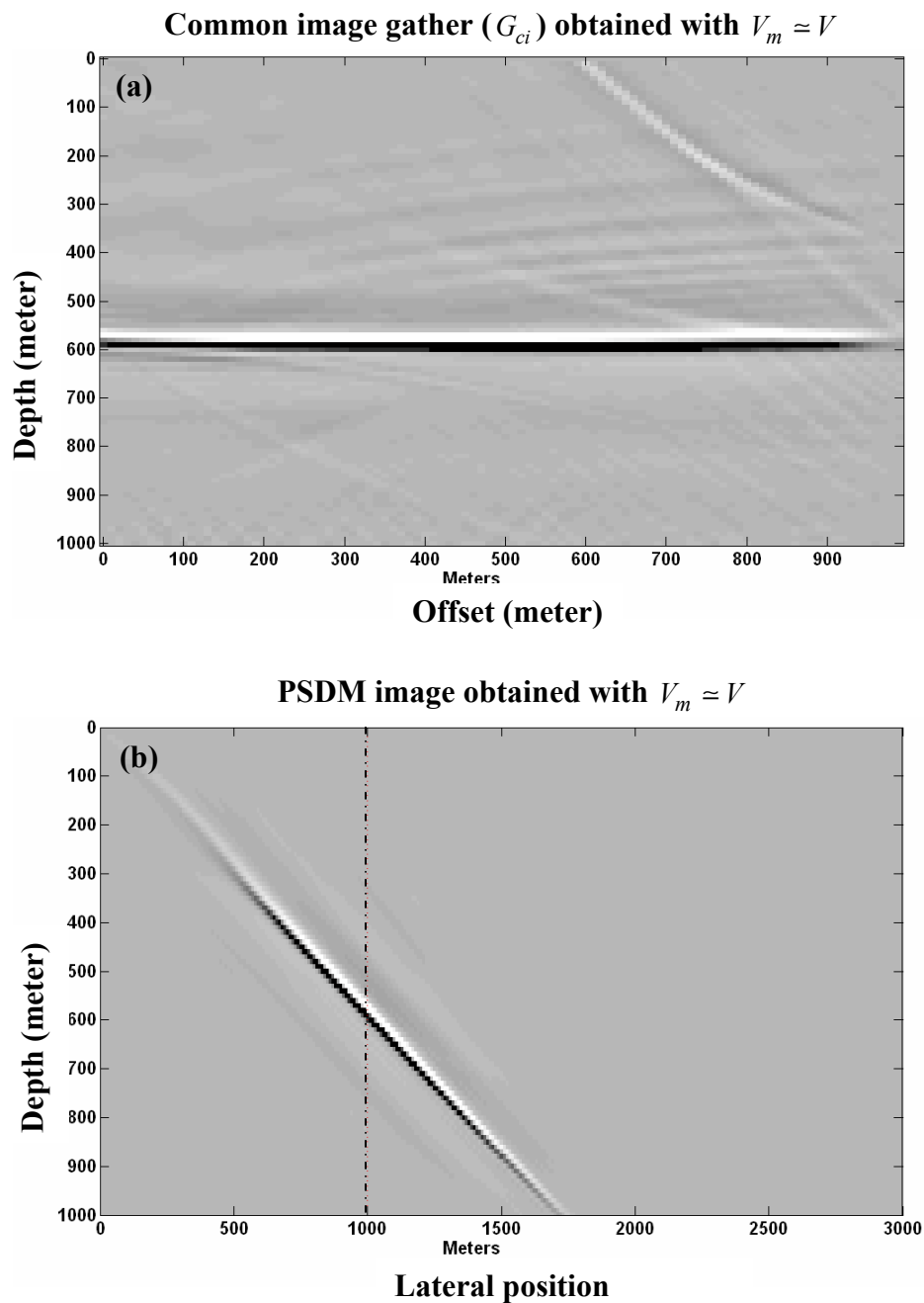


Figure 6-1. Using $V_m \approx V$ for constant velocity migration generates a flat event in (a) the common image gather, where (b) is the PSDM image formed by stacking the common image gathers over offset. In this example, $V = 2000$ m/s and the reflector dip is 30 degrees.

6-2.2 The RCA hypothesis

The following hypothesis describes the basics of residual curvature analysis (RCA) using the common image gathers. The term *background velocity model* is used to describe the velocity field used for the imaging process that creates the common image gathers; and *image depth* is used to refer to the depth at which a reflector appears in the imaging process. Generally, the background velocity model will resemble, but not equal, the true velocity field. The image depth will approach the true reflector depth when the background velocity model approaches the true velocity field.

The RCA imaging hypothesis: *A velocity model is correct when reflection events in the common image gathers are invariant with offset (flat).*

For a 2D dataset of S shots, having a maximum temporal signal frequency of

$f_{\max} = (2\pi)^{-1} \omega_{\max}$, and a prestack depth migration resulting in a set of common image gathers $G_{ci}(x_s, x_0, z; V_m)$, where the shot coordinate x_s is ranging from x_α to x_β , using a background velocity model, V_m , let a reflection event in a specific common image gather at lateral position x_0 be identified with the trajectory $z_e(x_s)$. That is,

$G_{ci}(x_s, x_0, z = z_e(x_s); V_m)$ is identified with the reflection event. Then, V_m is correct to δ wavelengths,

$$\|z_e(x_s) - \bar{z}\|_2 \leq \delta \lambda_{\min}, \quad (6.5)$$

for lateral position x_0 and image depth \bar{z} for the smallest dimensionless number $\delta > 0$ that can be found, and if

$$0 < \delta < 2 \quad (6.6)$$

then $V_m \approx V$ and $\bar{z} \approx z_r$, where z_r is the reflector depth, $\| \cdot \|_2$ denotes the L_2 norm,

$$\bar{z} = \text{mean}(z_e(x_s)), \quad x_s \in [x_\alpha, x_\beta], \quad (6.7)$$

and

$$\lambda_{\min} = \frac{V_m(x_0, \bar{z})}{f_{\max}}. \quad (6.8)$$

■

When using a background velocity model that closely resembles the true velocity field, the event, $z_e(x_s)$, will appear as a flat event (i.e. at nearly constant depth) (Figure 6-1a) on the common image gather, G_{ci} , and a smile or frown otherwise (Figure 6-2a) (Zhu et al., 1998). Note that the near offset information is missing in Figure 6.2b because the wrong velocity model was used for migration.

Inversion schemes are available to analyze the residual moveout on G_{ci} , and to invert for velocity updates (e.g. Lee and Zhang, 1992; Liu and Bleistein, 1994). Some of them are formulas that are derived based on simplifying assumptions, e.g. a smooth lateral velocity variation and small velocity errors²⁸. When these assumptions are violated, these formulas will fail to approximate the true velocity field adequately. Traveltime tomography, referred to in more detail in section 7-3, has been used in conjunction with

²⁸ Velocity error here means the difference between the background velocity and true velocity field.

RCA (Stork, 1992; Liu and Bleistein, 1994). The velocity updates estimated via tomography tend to be more accurate than updates using inversion formulas.

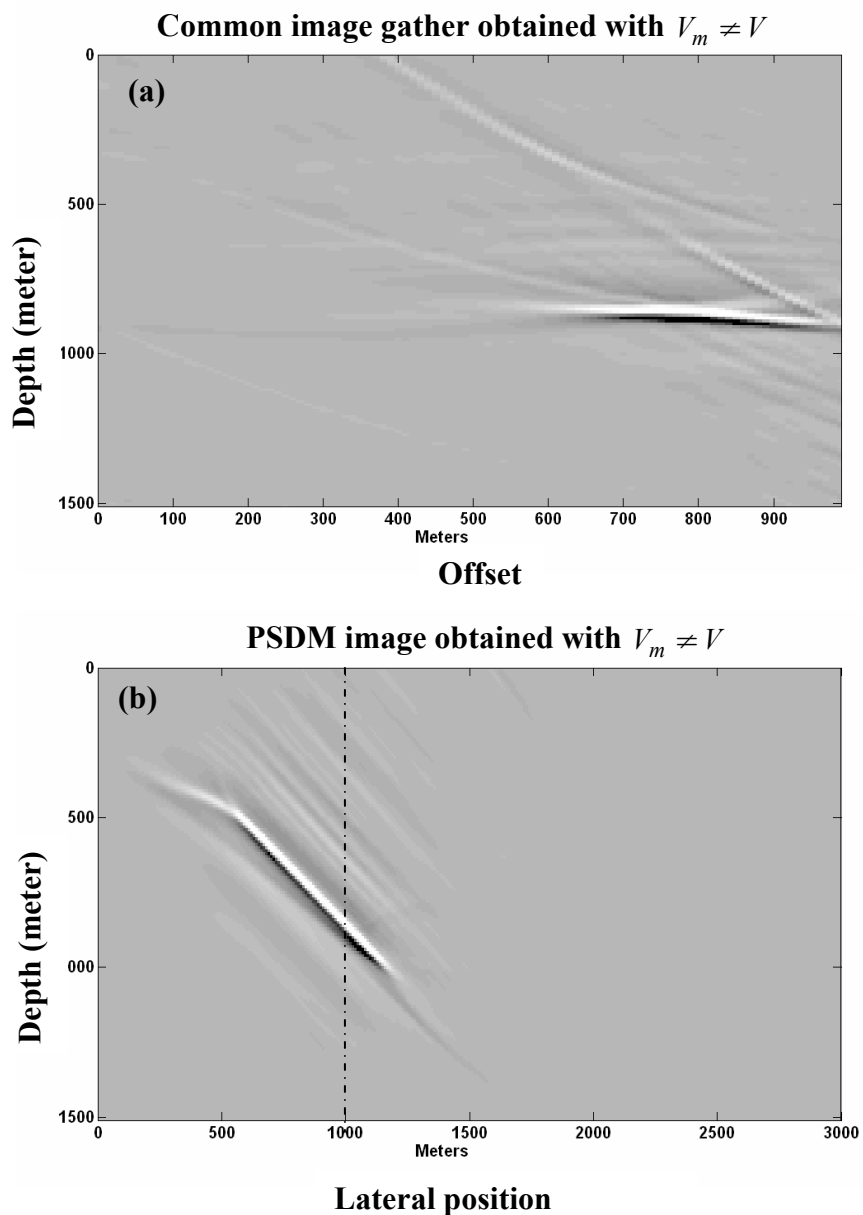


Figure 6-2. Using $V_m \neq V$ for constant velocity migration generates a non-flat event in (a) the common image gather, where (b) is the PSDM image formed by stacking the common image gathers over x_s . In this example, $V = 2000$ m/s and $V_m = 2600$ m/s.

6-2 DFA APPROACH

Depth focusing analysis (DFA, Yilmaz and Chambers, 1984; Faye and Jeannot, 1986) analyzes the energy build-up at the zero offset²⁹ in a depth focusing panel, which will be described shortly. In the literature, the DFA is described and constructed on the basis of source-receiver migration (section 5-2). Here, it is presented from a shot profile migration perspective.

In the depth focusing analysis (DFA), the zero-lag imaging condition is relaxed and the offsets are stacked to give one trace. To facilitate this, the common image gather definition of equation (6.3) is generalized to define depth focusing gathers as

$$G_{df}(x_s, x_o, z, \tau; V_m) = \int_{\mathbb{R}} U^-(x_s, x_o, z, \omega; V_m) D^+(x_s, x_o, z, \omega; V_m)^* \exp(i\omega\tau) d\omega, (6.9)$$

which simply generalizes equation (6.3) to non-zero lag. Thus $G_{df}(\tau = 0) = G_{ci}$.

6-2.1 The DFA imaging hypothesis

The basics of DFA can be described using the following hypothesis.

²⁹ Zero-offset here means source-receiver offset. In source-receiver migration, there are two imaging conditions: zero-time and zero-offset (for more about this refer to section 5-2).

DFA imaging hypothesis: *A velocity model is correct when the maximum stacked power of the depth focusing gathers occurs at zero lag.*

For a 2D dataset of S shots, having a maximum temporal signal frequency of

$f_{\max} = (2\pi)^{-1} \omega_{\max}$, and a prestack depth migration resulting in a set of depth focusing

gathers $G_{df}(x_s, x_o, z, \tau; V_m)$ using a background velocity model, V_m , let the gathers be

stacked over x_s to define the depth focusing panel

$$\sigma(x_0, z, \tau; V_m) = \sum_{x_s} G_{df}(x_s, x_0, z, \tau; V_m)^2. \quad (6.10)$$

Then define the focusing lag, τ_f , of the peak power by

$$\sigma(x_0, z, \tau_f; V_m) = \max[\sigma(x_0, z, \tau; V_m)], \quad (6.11)$$

where the search for the maximum is over τ , where the other variables are held fixed.

The reflector exists at every depth for which a distinct maximum can be found.

Then, for a fixed depth $z = z_f$, called the focusing depth, the velocity model is correct to

ε periods if

$$\tau_f f_{\max} \leq \varepsilon \quad (6.12)$$

for the smallest $\varepsilon > 0$, and if

$$0 < \varepsilon < 2 \quad (6.13)$$

then $V_m \approx V$ and $z_f \approx z_r$, that is, the focusing depth, z_f , is assumed to approach the

reflector depth, z_r .

■

6-2.2 The process of creating a depth focusing panel

The depth focusing panel, $\sigma(x_0, z, \tau; V_m)$, can be assembled using the following steps:

- Downward-continue the upgoing wavefield to a depth level.
- Forward model the downgoing wavefield to the same depth level.
- Sort the extrapolated data for a lateral position, x_0 , which results in two gathers:

$$U^-(x_s, x_0, z, \omega; V_m) \text{ and } D^+(x_s, x_0, z, \omega; V_m).$$

- Cross-correlate the two gathers (Figure 6-3a).
- Stack the result over x_s to give one trace.
- Storing this trace at each depth level creates a focusing panel for a specific lateral position (Figure 6-3b).

The value at zero-lag of all such traces that correspond to all lateral positions and depths forms the PSDM image. This is consistent with the Berkhout (2001) description of DFA as a double focusing method. The first focusing occurs when extrapolating the data to a depth level, and the second occurs when stacking over x_s . Any traveltime information about the upgoing and downgoing wavefields at the subsurface grid point is lost.

When using a background velocity model that approximates the true velocity field for migration, $V_m \approx V$, the maximum of $\sigma(x_0, z, \tau; V_m)$ over τ will occur at approximately the zero-lag, $\tau_f \approx 0$ (Figure 6-3a). When using $V_m \neq V$, however, the maximum will occur at a focusing lag that does not equal the zero-lag, $\tau_f \neq 0$ (Figure 6-4). There are

different inversion schemes that relate the focusing lag and focusing depth to velocity updates (e.g. MacKay and Abma, 1992; Lafond and Levander, 1993; Wang and Pann, 1998), but most of them make simplifying assumptions about the subsurface, and they may fail in the presence of strong lateral velocity variations and steeply dipping events.

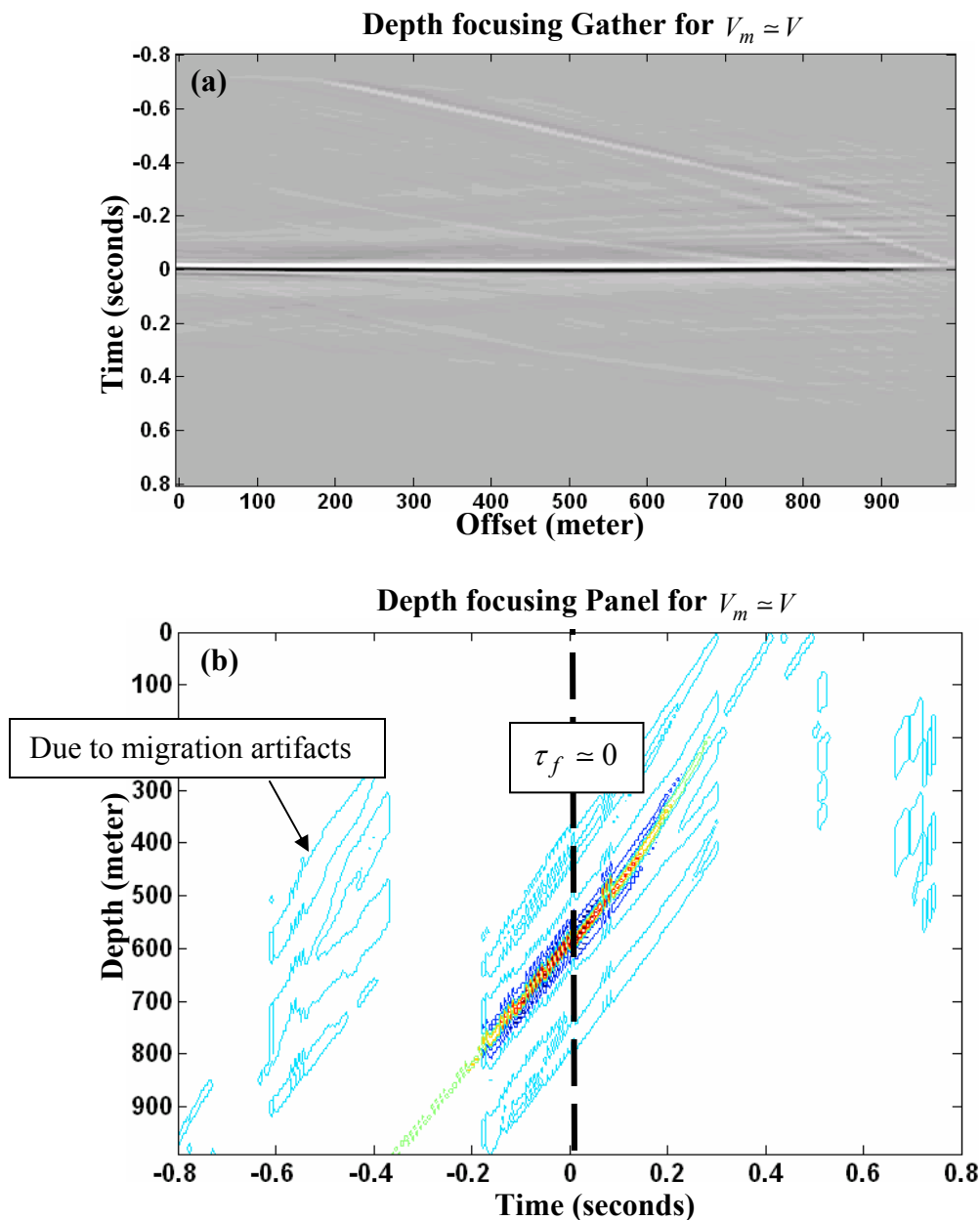


Figure 6-3. At each depth level, (a) the depth focusing gather is formed by cross-correlating the upgoing and downgoing wavefields, and (b) the depth focusing panel is formed by summing over x_s at each depth level. This is the same model that was used in Figure 6-1, where $V_m \approx V$. The dashed line indicates the zero-lag cross-correlation.

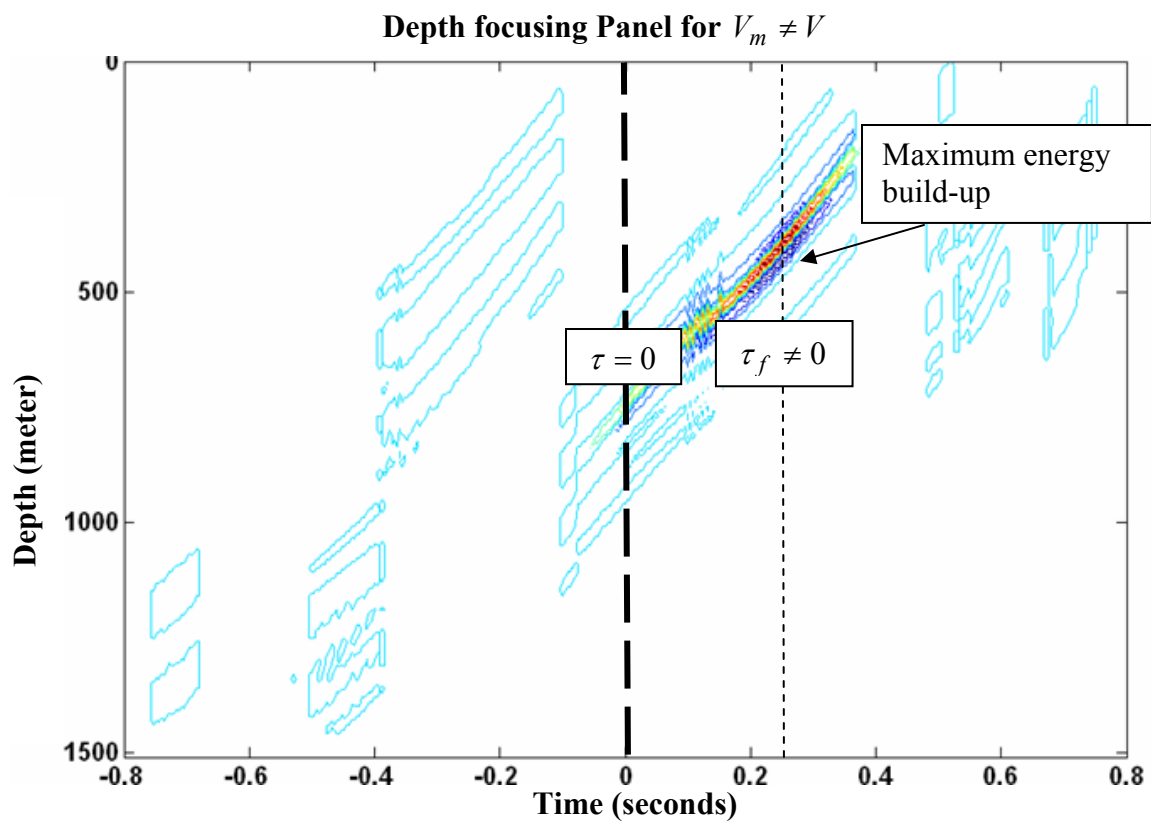


Figure 6-4. The depth focusing panel obtained with $V_m \neq V$. The dashed lines indicate the zero and focusing lags.

6-3 CFP APPROACH

The common focus point (CFP) analysis (Berkhout, 1997.a; Berkhout, 1997.b) is similar to DFA, but only involves a single focusing where the data are extrapolated to an initial guess of the reflector depth. The downward-continued upgoing wavefield and the forward modeled downgoing wavefield are then sorted for a lateral position to form two gathers where each is called a common focus point (CFP) gather.

The CFP approach is based on the principle of equal traveltimes, which states that the background velocity model is acceptable if the traveltimes of two events in these gathers are equal at the initial guess of the reflector depth. The CFP approach uses the differential time shift (DTS) panel as a tool to test the principle of equal traveltimes. The DTS panel is formed by cross-correlating the two gathers, which generates another event in this panel (Berkhout, 1997.b; Berkhout, 2001). Using a correct velocity model will result in a flat event at zero-lag in the DTS panel. Note that the values at the zero-lag of the DTS panel give the same values in the common image gather of the same lateral position at the depth of the initial guess of the reflector. Also, stacking all the traces in the DTS panel over x_s produces the same trace that goes into the DFA panel. In essence, the CFP approach is the limiting form of the RCA and DFA approaches.

6-3.1 Forming the common focus point gathers

Sorting the upgoing and downgoing wavefields, for a lateral position at particular depth level, results into two gathers. These gathers in the time domain can be described as

$$u^-(x_s, x, z, t; V_m) = \frac{1}{2\pi} \int_{\mathbb{R}} U^-(x_s, x, z, \omega; V_m) \exp(i\omega t) d\omega, \quad (6.14)$$

and the forward modeled downgoing wavefield is given by

$$d^+(x_s, x, z, t; V_m) = \frac{1}{2\pi} \int_{\mathbb{R}} D^+(x_s, x, z, \omega; V_m) \exp(i\omega t) d\omega. \quad (6.15)$$

6-3.2 The CFP imaging hypothesis

The following hypothesis describes some basics of the CFP approach.

The CFP imaging hypothesis: *The velocity model is correct when the downgoing wavefield matches an event in the upgoing wavefield in time and offset.*

As in DFA, a 2D dataset of S shots, having a maximum temporal signal frequency of $f_{\max} = (2\pi)^{-1} \omega_{\max}$, is passed into a prestack depth migration, using a background velocity model, V_m , and with a pre-selected set of depth locations,

(x_0, z_i) , $i \in [1, 2, \dots, M]$. At each of these locations, the upgoing time-domain wavefield,

$u^-(x_s, x_0, z_i, t; V_m) \equiv u_i^-(x_s, t; V_m)$, and its downgoing sibling,

$d^+(x_s, x_0, z_i, t; V_m) \equiv d_i^+(x_s, t; V_m)$, are estimated separately. Unlike DFA, the G_{df} are

neither formed explicitly and nor stacked over x_s . At each of the M analysis locations, a

reflection event is picked on the $u_i^-(x_s, t; V_m)$ and the corresponding event on the

downgoing wave is picked on $d_i^+(x_s, t; V_m)$. If the velocity model is exactly correct, these two events will occur on precisely the same time-offset function $t_i(x_s)$; however, in general, we will have a function $t_{ui}(x_s)$ of the upgoing wavefield and a different function of the downgoing wavefield, $t_{di}(x_s)$, that is, $t_{di}(x_s) \neq t_{ui}(x_s)$. The difference between them defines an offset-variant lag function $\tau_i(x_s) = t_{ui}(x_s) - t_{di}(x_s)$, which will be called the depth-specific delay function, which is the fundamental measure of the velocity model mismatch that is provided by CFP. These delay functions can be obtained directly by cross-correlating $u_i^-(x_s, t; V_m)$ with $d_i^+(x_s, t; V_m)$ and picking the location of maximum absolute value of the cross-correlation function on each trace. In fact, the cross-correlation of $u_i^-(x_s, t; V_m)$ with $d_i^+(x_s, t; V_m)$ is called the *differential time shift panel* or DTS panel and is a common tool. Since the G_{df} are just such cross-correlations at all depths, the DTS is simply a constant depth slice of the G_{df} . The analysis of the G_{df} as a cube in (x_s, x_0, z, τ) , is not typically carried out. Then, at (x_0, z_i) V_m is correct to ε periods if

$$|\tau_i(x_s)|_{f_{\max}} < \varepsilon, \quad \forall x_s \in [x_\alpha, x_\beta], \quad (6.16)$$

for the smallest dimensionless number $\varepsilon > 0$, and if

$$0 < \varepsilon < 2 \quad (6.17)$$

then $V_m \approx V$ and $z_i \approx z_r$, where z_r is the reflector depth.

■

The travelttime function, $t_d(x_s, x_0, z_i)$, of the first arrival of the downgoing field will match the travelttime function, $t_u(x_s, x_0, z_i)$, of a particular reflection at the reflector depth when $V_m \approx V$. In this case, the pre-selected depth, z_i , will equal the true reflector depth, z_r , that is, $z_i \approx z_r$.

In essence, this is simply a restatement of Claerbout's imaging principle (Claerbout, 1971), which states that a reflector exists in the subsurface where the upgoing and downgoing wavefields are coincident in time and space. While it is clear that a correct velocity model will have this property for a number of reflection events, it is not necessarily true that a model that satisfies this principle for a finite number of reflection events is close to the correct model. In other words, this condition is, in general, necessary but not sufficient. This concept can be also generalized to the RCA and DFA approaches.

CFP analysis is similar to DFA in that, in principle, both form and analyze the gathers $G_{df}(x_s, x_o, z, \tau; V_m)$ specified by equation (6.9). Although CFP does not explicitly form these gathers, an equivalent process could do so. DFA analyzes these gathers by the simple expedient of stacking over x_s and looking for power maxima. The result is just a single bulk estimate of a travelttime mismatch at each (x_0, z) . In contrast, CFP analyzes the data over x_s without stacking and thereby, with greater effort, obtains estimates of travelttime mismatches as a function of x_s for each analysis location. The CFP

information set is much richer than DFA, and offers more potential for inversion to estimate the appropriate velocity model updates.

By splitting $\tau_i(x_s)$ and applying half of it to t_u in the upgoing wavefield as

$$t_{u_{up}}(x_s, x_0, z_i) = t_u(x_s, x_0, z_i) - \tau_i(x_s)/2, \quad (6.18)$$

and half to t_d in the downgoing field,

$$t_{d_{up}}(x_s, x_0, z_i) = t_d(x_s, x_0, z_i) + \tau_i(x_s)/2, \quad (6.19)$$

the velocity model can be updated from the updated traveltimes, $t_{u_{up}}$ and $t_{d_{up}}$ (Berkhout, 1997b; Berkhout, 2001). Section 7-3 provides some discussion on how the velocity model can be updated using these updated traveltimes. The depth-specific delay functions for a good migration velocity model should all satisfy $|\tau_i(x_s)|f_{\max} < \varepsilon, \forall x_s \in [x_\alpha, x_\beta]$ for some $0 < \varepsilon < 2$. The criteria $\forall x_s \in [x_\alpha, x_\beta]$ and $0 < \varepsilon < 2$ are not mentioned in the original description of the CFP approach by Berkhout (1997.b).

Figure 6-5 shows examples of CFP gathers obtained from the extrapolated upgoing and downgoing wavefields to the reflector depth, that is, $z_i = z_r$, and using $V_m \approx V$ for migration. For simplicity, each gather has only a single event. Figure 6-6 shows the DTS panel, where the depth-specific delay function, $\tau_i(x_s)$, has a very small dependency on x_s . In other words, for $V_m \approx V$, the extrapolated upgoing and downgoing wavefields to

the reflector depth should have the same traveltime, which also means that, $\tau_i(x_s)$ becomes zero.

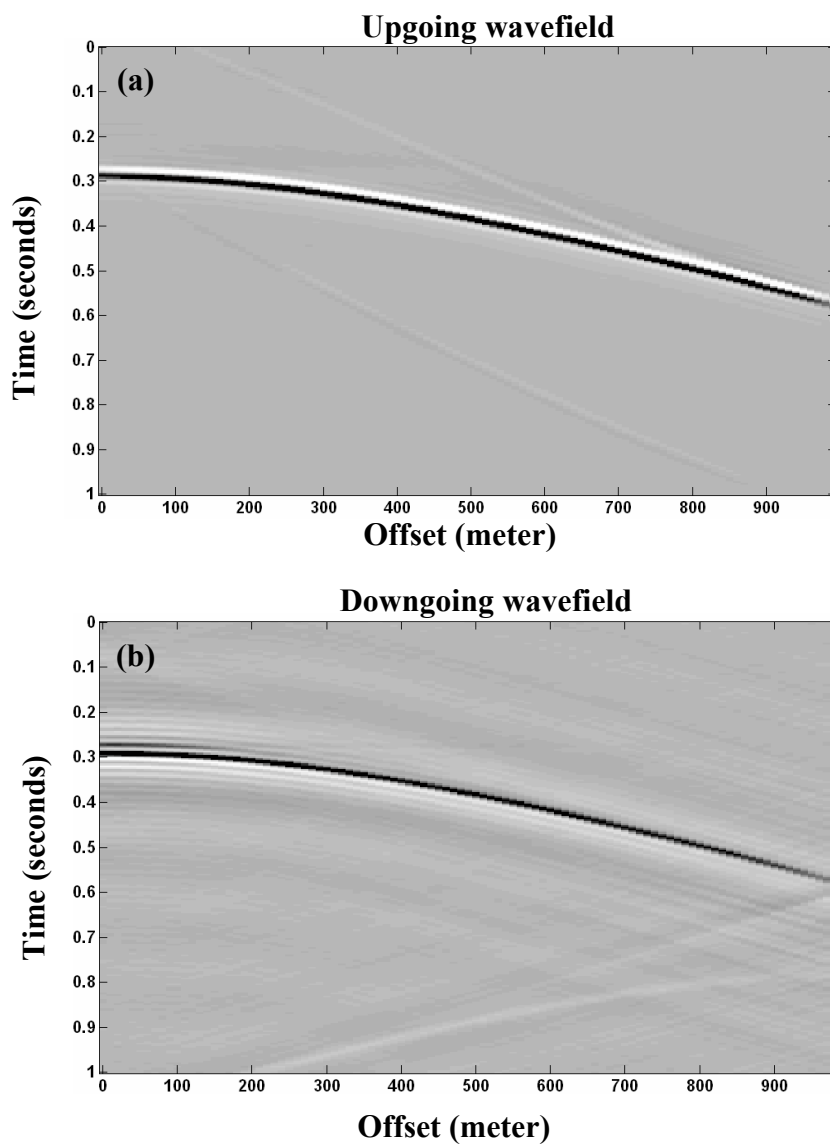


Figure 6-5. Examples of CFP gathers obtained with $V_m \approx V$, where (a) shows a CFP gather from the upgoing wavefield and (b) shows a CFP gather from the downgoing wavefield. The extrapolation depth equals the reflector point at the same lateral position shown in Figure 6-1a.

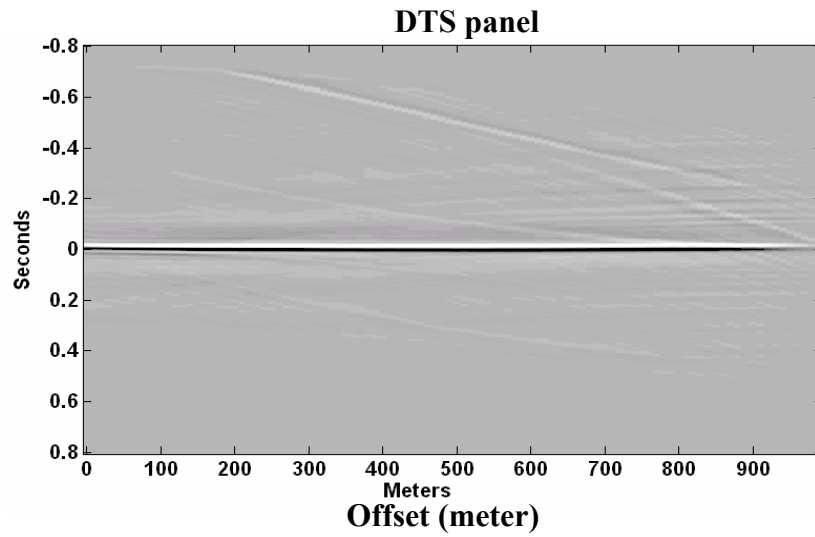


Figure 6-6. A DTS panel, $G_{df}(x_s, x_o, z_i = z_r, \tau; V_m)$, where $z_r = 585$ m, $x_0 = 1000$ m, and $S = 100$ for the same lateral position shown in Figure 6-1a.

6-4 CHAPTER SUMMARY

Currently, there exist very accurate algorithms for imaging complicated geological subsurface structures. These algorithms, however, are sensitive to velocity errors which make them an attractive tool for velocity analysis. This is the basis of migration velocity analysis (MVA) methods.

In this chapter, some well known migration velocity analysis domains were reformulated as mathematical hypotheses. The cases discussed included the residual curvature analysis (RCA), the depth focusing analysis (DFA), and the common focus point (CFP) analysis. This reformulation puts them all in the same context, so it is easier to understand and compare them. Further, restating them mathematically makes it easier to communicate them with other disciplines such as mathematics and physics.

These methods are all related. The common image gathers that are used in residual curvature analysis (RCA) are formed by picking the zero-lag of the cross-correlation between the upgoing and downgoing wavefields at each depth level without stacking over offset. On the other hand, the depth focusing panel that is used in depth focusing analysis (DFA) is formed by storing all the lags after summing over offset at each depth level. The common focus point (CFP) approach does the analysis at discrete depths by forming the differential time-shift (DTS) at these depths.

Depending on the author, one of these assumptions is made about most inversion formulas for the RCA and DFA: smooth lateral velocity variations and small offset. More

recently, tomography has been used with these methods to update the velocity model without the need to use simple formulae that only work for simple geology (section 7-3).

Migration velocity analysis (MVA) requires several iterations to build an acceptable velocity model. The final velocity model is usually imperfect due to multiples, anisotropy, and 3D effects when using 2D migration methods. Other issues that may plague MVA include noise and elastic effects such as converted waves. Although these problems are usually treated during the processing that precedes migration, their complete removal is not always guaranteed.

CHAPTER 7: THE COMMON IMAGE CUBE ANALYSIS (CICA) FOR MIGRATION VELOCITY ANALYSIS

In the previous chapter, different domains for migration velocity analysis (MVA) have been reviewed and reformulated as hypotheses. In this chapter, different aspects of the RCA, DFA, and CFP methods are combined into a unified domain for migration velocity analysis. This approach is called common image cube analysis (CICA).

Instead of just taking the zero-lag cross-correlation at each depth level, all the cross-correlation lags are stored. The result is a cube that contains more prestack information than the other methods. This cube was first mentioned by Faye and Jeannot (1986)³⁰. More recently, different slices of this cube were shown by Wang et al. (2005) to relate focusing errors to velocity updates using tomography. In this chapter, the CICA approach will be described.

7-1 THE COMMON IMAGE CUBE ANALYSIS APPROACH (CICA)

For a precise description of this method, the following hypothesis describes CICA.

³⁰ Although it was mentioned in Faye and Jeannot (1986), it was never displayed nor used.

7-1.1 The CICA imaging hypothesis

The CICA imaging hypothesis: *The velocity model must meet the RCA, DFA, and CFP criteria to be correct. It can be easily assessed and updated by analyzing the entire G_{df} cube at a selected analysis location.*

As in the DFA and CFP approaches, a 2D dataset of S shots, having a maximum temporal signal frequency of $f_{\max} = (2\pi)^{-1} \omega_{\max}$, is passed into a prestack depth migration, using a background velocity model, V_m , and resulting in a set of depth focusing gathers, $G_{df}(x_s, x_0, z, \tau; V_m)$. Unlike in DFA and CFP, now the G_{df} is analyzed without stacking, and at a fixed lateral position, x_0 , and at all depths. Let a reflection event in a specific depth-focusing gather, obtained at some specific τ at lateral position x_0 , be identified with the surface $z_e(x_s, \tau)$. Typically, this event will correspond to a set of local cross-correlation maxima over τ and x_s , while the other variables are held constant, in the sense that

$$\left| G_{df}(x_s, x_0, z_e(x_s, \tau), \tau; V_m) \right| = \max_{loc} \left(\left| G_{df}(x_s, x_0, z, \tau; V_m) \right| \right), \quad (7.1)$$

such that $z_e(x_s, \tau)$ has spatial continuity over (x_s, τ) , where $x_s \in [x_\alpha(\tau), x_\beta(\tau)]$ and $||$ denotes the L_1 norm. At this time, the identification of such reflection event surfaces is fundamentally subjective and interpretive. Let's define ϕ_e such that

$$\phi_e(x_s, \tau) = \left| z_e(x_s, \tau) - \bar{z}_e(\tau) \right| \quad (7.2)$$

where $\bar{z}_e(\tau)$ is the average over x_s for a fixed τ

$$\bar{z}_e(\tau) = \text{mean}(z_e(x_s, \tau)). \quad (7.3)$$

The lag at which this summation,

$$\sum_{x_s} \phi_e(x_s, \tau), \quad (7.4)$$

is a minimum is called the focusing lag, τ_f . Therefore there exists a focusing depth, z_f , such that

$$z_f = \bar{z}_e(\tau_f). \quad (7.5)$$

Thus z_f is the average depth of that part of $z_e(x_s, \tau)$ which is sufficiently flat. At a

position (x_0, z_f) , V_m is correct to ε periods

$$|\tau_f| f_{\max} < \varepsilon, \quad (7.6)$$

for the smallest nonnegative, dimensionless number $\varepsilon > 0$, and if

$$0 < \varepsilon < 2 \quad (7.7)$$

then $V_m \approx V$, $z_f \approx z_r$, and $\tau_f \approx 0$, where z_r is the true reflector depth.

■

7-1.2 The CICA imaging hypothesis in words

For 2D data, an event on the common image gather (section 6-1) can be either flat, frown, or smile depending on the background velocity model used for migration. In CICA, the same event appears as a surface instead of just a 2D event. Slicing this surface at different lags gives the same event at different lags, which correspond to different depths. If the flattest part of this surface occurs close to the zero-lag then the background velocity model is acceptable. Otherwise, the flattest part of that surface occurs at a different lag, a lag that does not approximately equal zero, and also at a depth that is not close to the

reflector depth. The lag and depth at which the flattest part occurs are called the focusing lag, τ_f , and the focusing depth, z_f .

7-1.3 The RCA, DFA, CFP, and CICA approaches

The difference between the CFP and CICA approaches is that, for a particular reflection event, the CFP analysis starts with an initial guess of the reflector depth, z_i ; while in the CICA approach, the analysis is done around the observed focusing depth, z_f , defined as the flattest part of the event surface $z_e(x_s, \tau)$. Prior to migration, the focusing depth, z_f , is not known, whereas in CFP (section 6-3), z_i is prescribed. The CICA approach may converge faster to approximating the true velocity field than the CFP approach because the traveltimes of the analyzed events in the upgoing and downgoing wavefields are separated by τ_f . On the other hand, in CFP, the separation in time between the two events might be more offset-dependent than τ_f . Further, the same updating procedure can be used in CICA as is used in CFP (section 7-3).

Furthermore, slicing $G_{df}(x_s, x_o, z, \tau; V_m)$ at different τ values generates depth focusing gathers which can be assessed for flatness as in RCA (section 6-1)³¹. Also, the focusing of energy at a depth different from the true depth when $V_m \neq V$ is an aspect of the DFA (section 6-2). Thus, CICA is a combination of the three previous methods.

³¹ Recently, this was used by Wang et al. (2005) to find the focusing error. This error is then used in a tomography scheme to find velocity updates.

7-2 CONSTANT VELOCITY EXAMPLES

Figure 7-1 shows a prestack depth migrated (PSDM) image obtained with $V_m = V$, where the dotted line indicates a lateral position or an analysis location. Figures 7-2a and 7-2b show the common image cubes (CICs) of a lateral position (see the dashed line in Figure 7-1) for two cases: $V_m = V$ and $V_m > V$, respectively. Slicing the cubes shown in Figure 7-2 shows that for the $V_m = V$ case (Figure 7-3a), the gather, $G_{df}(x_s, x_o, z, \tau = 0; V_m)$, is the most focused gather, that is, the reflection event appears to be flat. Also, $V_m = V$ means $\tau_f = 0$. On the other hand, for the second case (Figure 7-3b), $V_m > V$, the gather, $G_{df}(x_s, x_o, z, \tau = 0; V_m)$, is not the most focused gather, where the reflection event appears to be a frown. The most focused gather, $G_{df}(x_s, x_o, z, \tau = \tau_f; V_m)$, can be obtained by slicing the cube at $\tau_f \neq 0$.

Each trace of the PSDM image (Figure 7-1) is the stack over x_s of the gather obtained at the zero-lag, $G_{df}(x_s, x_o, z, \tau = 0; V_m)$ (section 6-1). In other words, only a slice of the cube is really used to form the final image. This cube, however, offers prestack information that can be used for MVA. Further, carrying out migration velocity analysis in this domain can be more advantageous to other methods that only retain parts of this cube.

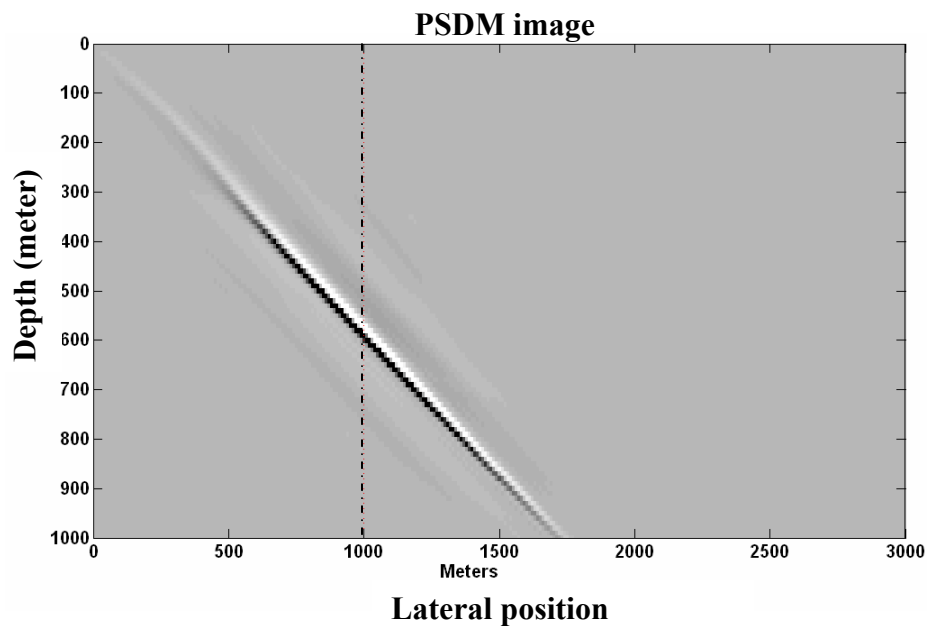


Figure 7-1. A PSDM image obtained using $V_m \approx V$, where $V = 2000$ m/s. The dashed line shows a lateral position or analysis location that will be used in the next figures.

(a) $V_m \approx V$

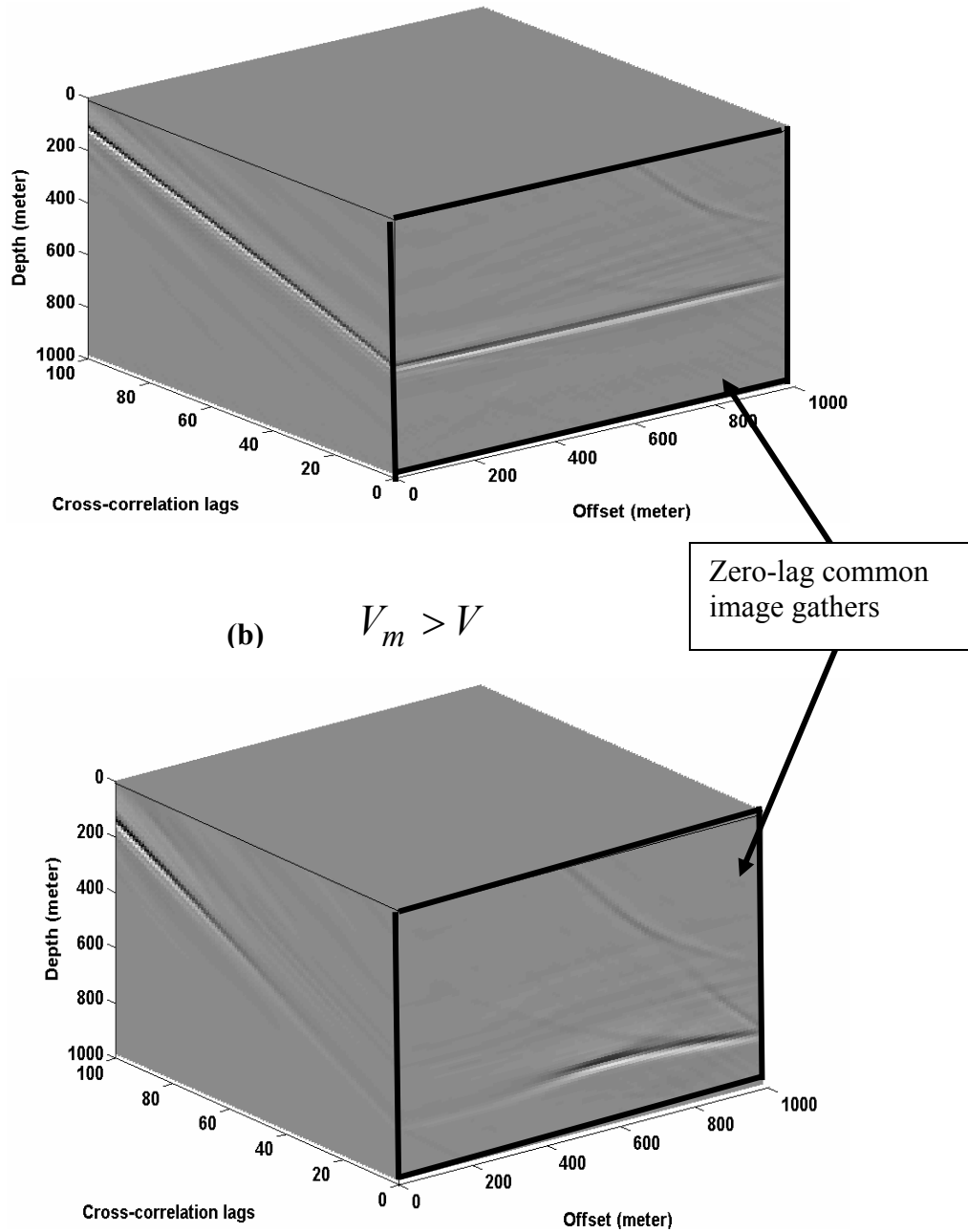


Figure 7-2. The common image cube (CIC), where (a) is obtained with $V_m \approx V$, and (b) is obtained with $V_m > V$. The arrows indicate the zero-lag common image gathers (section 6-1), which are only slices of these cubes. The thick border indicates the location of $G_{df}(x_s, x_o, z, \tau = 0; V_m)$.

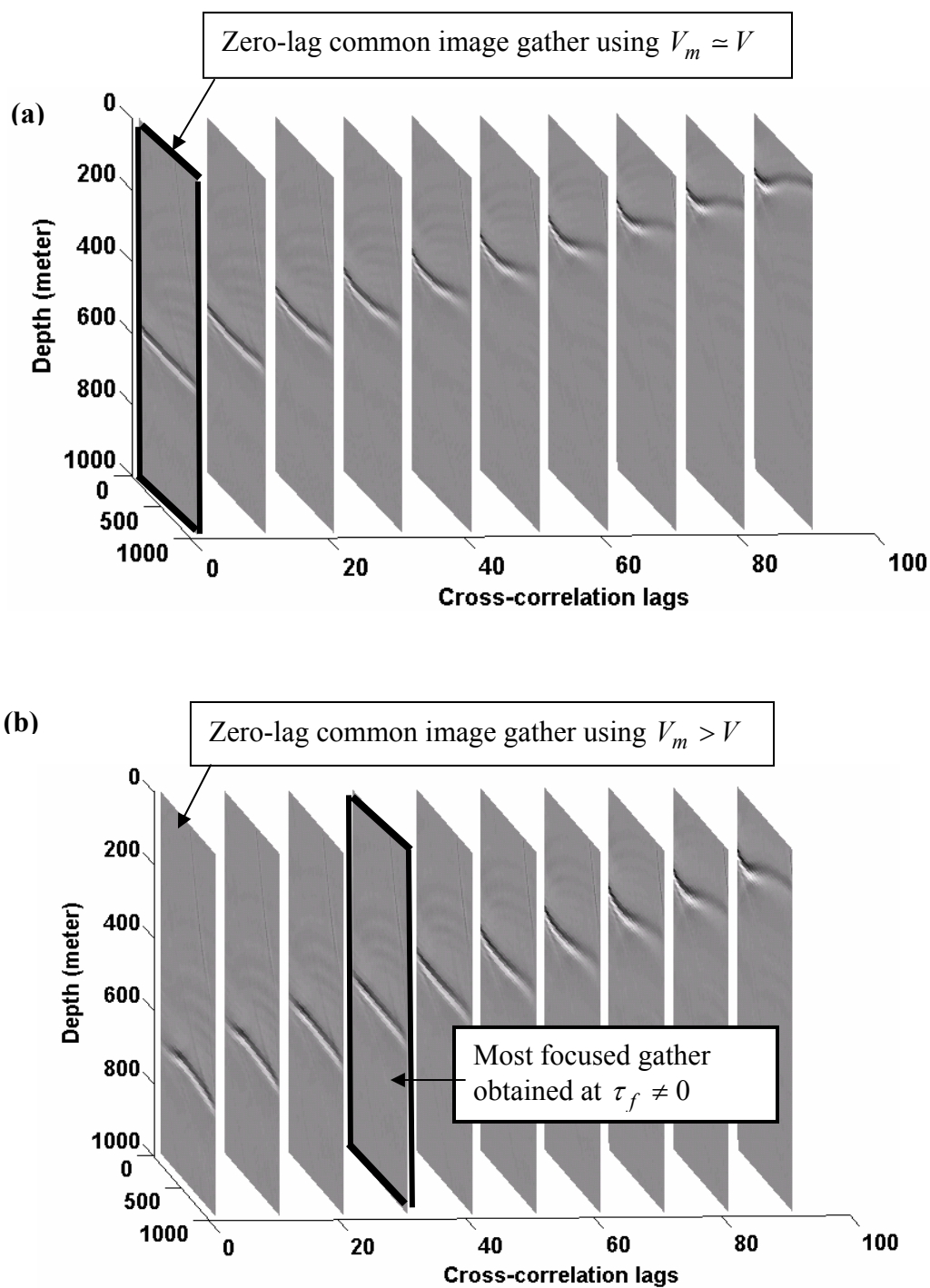


Figure 7-3. Slices of (a) the cube in Figure 7-2a and (b) the cube in Figure 7-2b at different lags. The thick border indicates the location of $G_{df}(x_s, x_o, z, \tau = \tau_f; V_m)$.

Figure 7-4 shows composites of the upgoing and downgoing wavefields, for the same lateral position indicated with a dotted line in Figure 7-1, for three cases:

1. $V/V_m = 0.9091$ (Figure 7-4a).
2. $V/V_m = 0.8083$ (Figure 7-4b).
3. $V/V_m = 0.7692$ (Figure 7-4c).

For each case, the upgoing and downgoing wavefields have been extrapolated to a depth equal to the focusing depth. Finding the focusing depth for each case requires analyzing the cube to find the depth at which the most focusing occurs. Note that for all three cases $V_m \neq V$, and for simplicity, the upgoing wavefield has only one event. Moreover, in each figure, two reflection events can be identified that have traveltimes: $t_u(x_s)$ that corresponds to the traveltimes of the event in the upgoing wavefield, and $t_d(x_s)$ that corresponds to the reflection event in the downgoing wavefield, where the true traveltimes, calculated using the true velocity field, is shown for comparison. The true traveltimes, in a constant velocity medium, can be calculated using

$$t(x_s) = \sqrt{\left(\frac{2z_r}{V}\right)^2 + \left(\frac{x_s}{V}\right)^2}. \quad (7.8)$$

A promising observation can be drawn from this example: in the three cases, the traveltimes difference between of $t_u(x_s)$ and $t_d(x_s)$ has a very weak offset dependency, even for a relatively large velocity error (case 3). From the CICA hypothesis, this traveltimes difference can be approximated with τ_f .

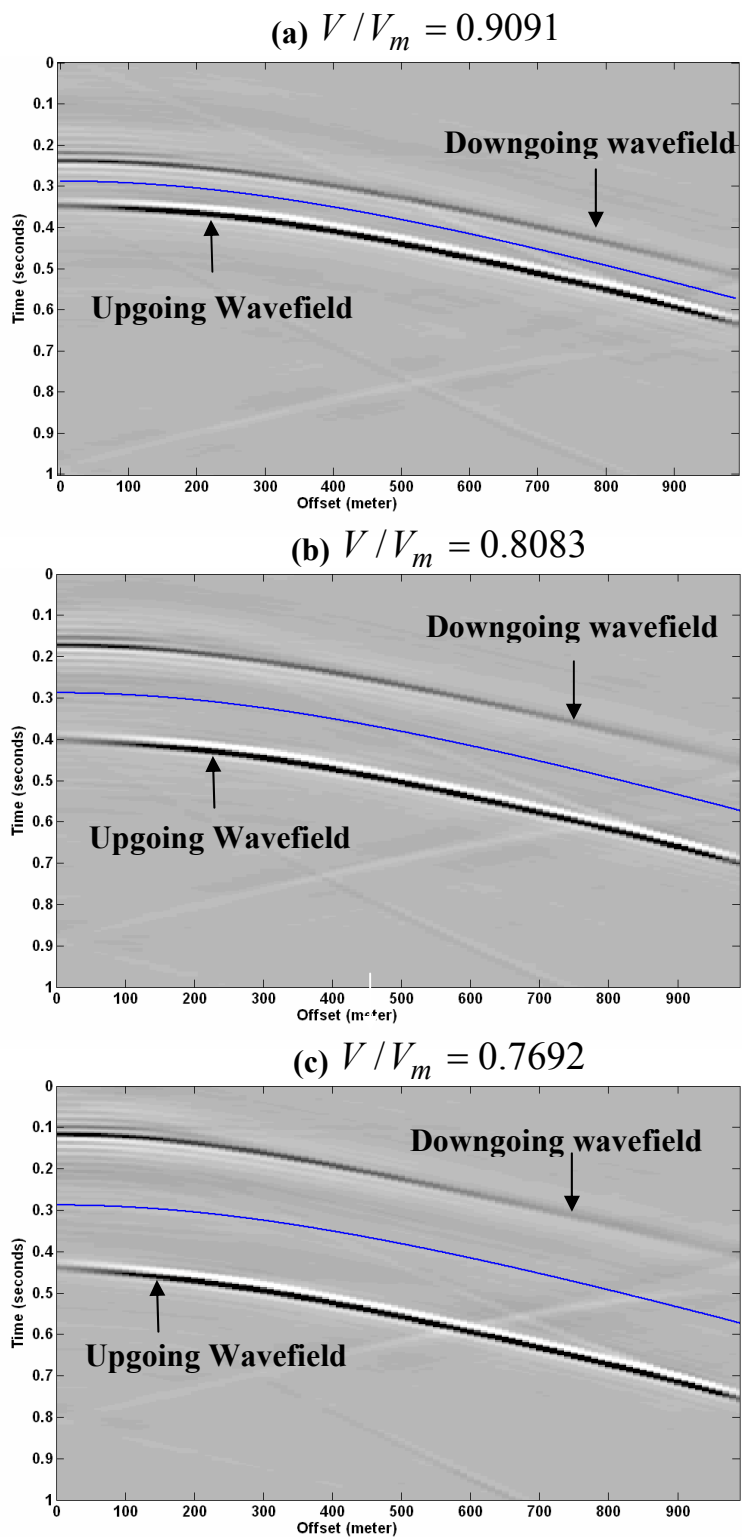


Figure 7-4. Composites of the upgoing and downgoing wavefields for three cases: (a) 10% velocity error, (b) 20% velocity error, and (c) 30% velocity error. The true traveltimes calculated using $V=2000$ m/s is shown for comparison.

7-3 INVERSION AND VELOCITY MODEL UPDATING

According to Claerbout's imaging condition (Claerbout, 1971), a reflector, in an isotropic medium, exists at a point when the upgoing and downgoing wavefields are coincident in time and space. Berkhout (1997b; 2001) uses this imaging condition as a criterion to test the validity of the velocity model. That is, in the CFP approach, the velocity model is acceptable if the traveltimes of two events in the upgoing and downgoing wavefields are approximately equal (section 6-3). This principle is called the principle of equal traveltimes, which is a reformulation of Claerbout's imaging condition.

In Figure 7-4, the traveltimes of the two reflection events in the upgoing and downgoing wavefields, $t_u(x_s)$ and $t_d(x_s)$, at a specific lateral position, are separated by a time-shift that approximately equals the focusing lag, τ_f , that is

$$t_u(x_s) - t_d(x_s) \approx \tau_f. \quad (7.9)$$

One way to satisfy Claerbout's imaging condition and Berkhout's principle of equal traveltimes is to apply a time-shift to $t_u(x_s)$ and $t_d(x_s)$ such that

$$\tilde{t}_d(x_s) = t_d(x_s) + \tau_f \quad (7.10)$$

and

$$\tilde{t}_u(x_s) = t_u(x_s) - \tau_f \quad (7.11)$$

are approximately equal,

$$\tilde{t}_u(x_s) \approx \tilde{t}_d(x_s). \quad (7.12)$$

The traveltimes functions, $\tilde{t}_u(x_s)$ and $\tilde{t}_d(x_s)$, approximate the one-way traveltime from an image point to the receivers. The traveltimes functions, $\tilde{t}_u(x_s)$ and $\tilde{t}_d(x_s)$, cannot be alone used to update the velocity model— that is, updating the velocity model requires the depth of the reflector point and velocity update.

One way to get this information is to use seismic tomography (Bishop et al., 1985).

Seismic tomography can be defined as an imaging technique that transforms the recorded seismic data into a velocity model of the subsurface (Tarantola, 1984; Woodward, 1992).

Seismic tomography can be divided into two major categories (Cox, 2001): wave-equation tomography and traveltimes tomography. In wave-equation tomography, the complete seismic wavefield is used, whereas in traveltimes tomography only the traveltimes of the reflection events are taken into account.

Migration velocity analysis (MVA) tomography is an example of traveltimes tomography.

In this method, the common image gathers are formed from the migrated data using a background velocity model (section 6-1). In these gathers, unaligned events indicate erroneous migration velocities. These events are then picked to reveal velocity errors that can be converted into traveltimes errors. Then these traveltimes errors are tomographically inverted to obtain velocity updates and reflector depths (see e.g. Kosloff et al., 1996).

Note that this type of tomography uses the common image gathers that are formed after invoking the imaging condition.

Traveltime tomography has also been used in the CFP approach (e.g. Cox (2001); Thorbecke (1997)). It estimates the reflector depth and velocity updates from the one-way traveltimes of the events in the CFP gathers; however, it may require several iterations to build an acceptable velocity model. Since traveltime tomography has been used successfully in RCA, DFA, CFP, it is expected to do so in the CICA approach.

7-4 CHAPTER SUMMARY

The CICA method combines various aspects of the RCA, DFA, and CFP methods into a unified approach that offers more prestack information than the other methods. The basis of this method is that instead of retaining only the zero-lag information, all the lags are stored at each depth level. For each lateral position, the result is a cube of data that is available for migration velocity analysis.

The CFP approach offers more prestack information than the RCA and DFA approaches, but less prestack information than the CICA approach. Since the RCA, DFA, and CFP approaches have been shown by numerous authors (see e.g. Al-Yahya, 1989; Faye and Jeannot, 1986; Berkhout, 1997b; Berkhout, 2001) as appropriate domains for MVA, the CICA is also expected to do so, since it is just the integration of different aspects of these methods. In fact, the traveltime tomography that is currently used in CFP (Cox, 2001; Thorbecke, 1997; Berkhout, 1997b; Berkhout, 2001) can be used in CICA to update the velocity model. The CICA is a promising tool for MVA, but requires developing some software in order to compare it with other approaches.

CHAPTER 8: DISCUSSION AND CONCLUSIONS

Seismic migration is used to construct an image of the subsurface by transforming the reflection events, recorded as seismograms, from the data space to the image space (section 1-1). Seismic migration involves two steps: wavefield extrapolation and imaging condition (section 2-2). Wavefield extrapolation methods are often considered to fall into two major categories: (1) Kirchhoff methods and (2) downward-continuation methods.

In complicated geological subsurface structures, images generated using Kirchhoff methods are less accurate than those generated using downward-continuation methods (Gray et al., 2001; section 1-2). Further, downward-continuation methods force multipathing between the surface points and the depth points, while in the case of Kirchhoff migration, only few paths at most are allowed to connect a surface point with a depth point (Gray and May, 1994).

8-1 EXPLICIT WAVEFIELD EXTRAPOLATION METHODS

Explicit wavefield extrapolation methods are a branch of downward-continuation methods that have been widely accepted as a powerful tool for imaging complex subsurface structures. They are the space-frequency equivalent of the generalized phase-shift plus interpolation (GPSPI, Margrave and Ferguson (1999)) algorithm if the nonstationary convolution operators are infinitely long. They are called explicit methods because the wavefield at an output point, at some depth level, can be computed independently from the other output points using a wavefield extrapolator that is

implemented as a filter (Berkhout, 1981). They are also called recursive because the wavefield at each depth level is computed from the wavefield at the previous depth level.

8-2 HALE, SOUBARAS, WLSQ, AND FOCI WAVEFIELD EXTRAPOLATORS

The ideal wavefield extrapolator has infinite spatial extent, and for practical implementation, it has to be approximated with a compactly supported operator. Since these methods are recursive, the approximated operator should be stable, that is, it does not amplify the wavefield each time it is used.

Using simple window functions, such as a boxcar or a Hanning window, to truncate the ideal extrapolator, can either lead to unstable operators or operators that are suboptimal (section 2-5.1). In Chapter 3, some advanced methods for designing wavefield extrapolator were reviewed and compared. These techniques were developed by Hale (1991), Soubaras (1996), Thorbecke et al. (2004), and Margrave et al. (2006).

Hale's method (section 3-1) is based on the expansion of the phase-shift operator in a long Taylor series, and then approximating the series with a special set of basis functions. That is, the spectrum of Hale's extrapolator is just the superposition of some weighted basis functions. Soubaras (1996), on the other hand, uses the Remez exchange algorithm to find the coefficients of the extrapolator such that the maximum weighted error, or the L_∞ norm, of the desired and actual spectra is minimized (section 3-2). Thorbecke et al. (2004) use a weighted least-squares (WLSQ) approach, where the desired spectrum is a model-based function that only approximates the exact spectrum in the wavelike region

(section 3-3). The model-based function is used to avoid the sharp slope discontinuities that are present in the exact spectrum.

The FOCI extrapolator (Margrave et al., 2006) is assembled by convolving an operator with the conjugate of its least-squares band-limited inverse (section 3-4). It may either be used directly or shortened with a Hanning window. Also, the FOCI algorithm assumes that evanescent filtering is not needed at every depth step. As a result, dual operator tables can be used in depth migration, where the first table is used for evanescent filtering applied every j^{th} step, and the other is used for most of the extrapolation steps. Besides the use of dual tables, the FOCI algorithm applies a spatial downsampling of the lower frequencies to increase operator accuracy and decrease run times.

Unlike Hale's extrapolator, the Soubaras, WLSQ, and FOCI extrapolators are not perfectly stable, but have controllable instabilities (section 3-5). However, they can handle higher angles of propagation than Hale's. Calculating tables of extrapolators using the Soubaras, WLSQ, and FOCI methods is computationally more efficient than using Hale's method. Further, while FOCI results are comparable with results obtained with the other methods, it is computationally less expensive than the other methods due to spatial resampling.

8-3 THE WLSTB APPROACH AND THE OPTIMIZED FOCI ALGORITHM

In Chapter 4, the weighted least-squares with a transition band (WLSTB) approach was developed to design practically stable wavefield extrapolators. In this approach, the band

of wavenumbers for the transition region, that contains the slope discontinuities, are simply removed from the error definition. The differences between the WLSQ and WLSTB approaches are two fold: (1) In WLSQ, a model-based function is used as the desired spectrum, whereas in WLSTB, the exact spectrum is used, and (2) they use two different weight functions. That is, in WLSTB, the weight function is used to put more weight on the wavelike region than the evanescent region and to exclude the transition band from the error measure (section 4-1.3). Results obtained with this approach are comparable to the WLSQ (section 4-2).

Then, the WLSTB approach was used to optimize the FOCI algorithm. It is used in FOCI to replace the use of a Hanning window in obtaining the forward and post-design operators (section 4-3). In general, using a window function to design an operator is suboptimal because it does not minimize the error between the actual and desired spectra (Parks and Burrus, 1987). The FOCI images were comparable with images obtained with other methods (section 3-5); however, it could not design short operators that could handle high angles of propagation. Combining the FOCI algorithm with the WLSTB approach makes it more efficient, since the forward and post-design operators are now obtained in an optimal way. With the optimized algorithm it is now possible to design short operators that remain practically stable in a recursive scheme. Images obtained with optimized algorithms are superior to images obtained with the old design (section 4-3.3).

8-4 DOWNWARD-CONTINUATION FROM TOPOGRAPHY

Although explicit wavefield extrapolation methods can better handle lateral velocity variations than ray-based methods, they assume that the data to be extrapolated are recorded from a flat surface. There are different approaches that can be used to avoid this problem such as wave-equation datuming (Berryhill, 1979) and the zero-velocity approach (Beasley and Lynn, 1992; Gray, 1997). In section 5-1, the zero-velocity approach was extended to the prestack case by time-shifting the upgoing and downgoing wavefields in opposite directions with respect to a flat datum. Then, a special wavefield extrapolator was used to carry out the extrapolation between the datum and the recording surface.

Wavefield extrapolation can be also carried out directly from topography by designing wavefield extrapolators that can handle lateral velocity and topographic variations. This approach was first implemented using a source-receiver migration scheme (section 5-2). Then, it was implemented using a shot profile migration scheme by manipulating the Green function that is used to simulate the downgoing wavefield (section 5-3).

8-5 THE RCA, DFA, AND CFP DOMAINS FOR MVA

Wavefield extrapolation methods are very sensitive to velocity models, which makes them a good tool for migration velocity analysis (MVA). Three domains for MVA were derived in the same context, from a shot profile migration perspective, and then reformulated as hypotheses in mathematical terms. These domains were the residual curvature analysis (RCA, Al-Yahya, 1989) (section 6-1), depth focusing analysis (DFA,

Faye and Jeannot, 1986) (section 6-2), and the common focus point (CFP, Berkhout, 1997.a) analysis (section 6-3). This reformulation is an important step towards a precise description of these methods. Also, it helps us to communicate them to other disciplines such as physics and mathematics to find solutions to our geophysical problems from other fields.

For each domain, a different inversion scheme can be used to relate velocity errors to velocity updates. The inversion scheme can be based on formulas, derived based on assumptions of small offset and smooth lateral velocity variations, or based on traveltimes tomography (section 7-3).

8-6 THE CICA APPROACH

In Chapter 7, different aspects of existing domains were combined into a unified domain for migration velocity analysis, called the common image cube analysis (CICA). It offers more prestack information than the other domains. The basis of this method is that instead of only retaining the zero-lag information, all the lags are stored at each depth level. For each lateral position, the result is a cube of data that is available for migration velocity analysis.

Further, since the RCA, DFA, and CFP have been shown by numerous authors (see e.g. Al-Yahya, 1989; Faye and Jeannot, 1986; Berkhout, 1997b) to be appropriate domains for MVA, the CICA is also expected to be one, since it is the limiting form of these domains. In fact, the traveltimes tomography that is currently used in CFP (Cox, 1996;

Thorbecke et al., 1997; Berkhout, 1997b; Berkhout, 2001) can be used in CICA as a potential inversion scheme to update the velocity model. This approach, however, requires the development of software to prove the CICA hypothesis.

**APPENDIX A: THE FOURIER TRANSFORM OF THE WAVEFIELD
EXTRAPOLATOR**

Let $\tilde{W}(x)$ denotes an even compactly supported operator, with an odd number of coefficients, N , then the discrete Fourier transformation over the spatial coordinate, x , of $\tilde{W}(x)$ can be expressed as

$$\hat{\tilde{W}}(k_x) = \sum_{m=0}^M (2 - \delta_{m0}) \tilde{W}(m\Delta x) \cos(m\Delta x k_x), \quad (\text{A.1})$$

where

$$\delta_{m0} = \begin{cases} 1; & m = 0 \\ 0; & m \neq 0 \end{cases}, \quad (\text{A.2})$$

$$M = \frac{N-1}{2}, \quad (\text{A.3})$$

and k_x is the transverse wavenumber.

Proof:

The discrete Fourier transformation of $\tilde{W}(x)$ over the spatial coordinate, x , or the spectrum of $\tilde{W}(x)$, can be written as

$$\hat{\tilde{W}}(k_x) = \sum_{-M}^M \tilde{W}(m\Delta x) \exp(im\Delta x k_x). \quad (\text{A.4})$$

Equation (A.4) can be rewritten as

$$\hat{\tilde{W}}(k_x) = \sum_{-M}^M \tilde{W}(m\Delta x) \cos(m\Delta x k_x) + i \sum_{-M}^M \tilde{W}(m\Delta x) \sin(m\Delta x k_x). \quad (\text{A.5})$$

Since \tilde{W} is even in x and the sine function is an odd function,

$$\sin(-x) = -\sin(x), \quad (\text{A.6})$$

the second term in equation (A.5) goes to zero. So equation (A.5) reduces to

$$\hat{W}(k_x) = \sum_{-M}^M \tilde{W}(m\Delta x) \cos(m\Delta x k_x). \quad (\text{A.7})$$

The above equation can be decomposed into

$$\hat{W}(k_x) = \sum_{m=-M}^{-1} \tilde{W}(m\Delta x) \cos(m\Delta x k_x) + \tilde{W}(0) + \sum_{m=1}^M \tilde{W}(m\Delta x) \cos(m\Delta x k_x). \quad (\text{A.8})$$

The cosine function is an even function, that is

$$\cos(x) = \cos(-x), \quad (\text{A.9})$$

which also means that

$$\sum_{m=-M}^{-1} \tilde{W}(m\Delta x) \cos(m\Delta x k_x) = \sum_{m=1}^M \tilde{W}(m\Delta x) \cos(m\Delta x k_x). \quad (\text{A.10})$$

As a result, equation (A.8) can be rewritten as

$$\hat{W}(k_x) = \tilde{W}(0) + 2 \sum_{m=1}^M \tilde{W}(m\Delta x) \cos(m\Delta x k_x), \quad (\text{A.11})$$

or

$$\hat{W}(k_x) = \sum_{m=0}^M (2 - \delta_{m0}) \tilde{W}(m\Delta x) \cos(m\Delta x k_x), \quad (\text{A.12})$$

where δ_{m0} was defined in equation (A.2).

APPENDIX B: REAL AND IMAGINARY PARTS OF THE WAVEFIELD

EXTRAPOLATOR

The real and imaginary parts of a spectrum, $\hat{W}(k_x)$ of an even operator, $\tilde{W}(x)$, that has N odd complex coefficients, can be written as

$$\hat{W}_r(k_x) = \sum_{m=0}^M (2 - \delta_{m0}) \tilde{W}_r(m\Delta x) \cos(m\Delta x k_x) \quad (\text{B.1})$$

and

$$\hat{W}_i(k_x) = \sum_{m=0}^M (2 - \delta_{m0}) \tilde{W}_i(m\Delta x) \cos(m\Delta x k_x), \quad (\text{B.2})$$

respectively, where

$$\tilde{W}_r(x) = \text{real}(\tilde{W}(x)), \quad (\text{B.3})$$

$$\tilde{W}_i(x) = \text{imag}(\tilde{W}(x)), \quad (\text{B.4})$$

$$M = \frac{N-1}{2}, \quad (\text{B.5})$$

and

$$\delta_{m0} = \begin{cases} 1; & m = 0 \\ 0; & m \neq 0 \end{cases}. \quad (\text{B.6})$$

Also, x is the transverse coordinate and k_x is the transverse wavenumber.

Proof: The discrete Fourier transformation of an even function, $\tilde{W}(x)$, over x can be written as (see Appendix A)

$$\hat{W}(k_x) = \sum_{m=0}^M (2 - \delta_{m0}) \tilde{W}(m\Delta x) \cos(m\Delta x k_x). \quad (\text{B.7})$$

Rewriting equation (B.7) using equations (B.3) and (B.4) gives

$$\hat{W}(k_x) = \sum_{m=0}^M (2 - \delta_{m0}) (\tilde{W}_r(m\Delta x) + i\tilde{W}_i(m\Delta x)) \cos(m\Delta x k_x). \quad (\text{B.8})$$

Equation (B.8) can be rewritten as

$$\hat{W}(k_x) = \hat{W}_r(k_x) + i\hat{W}_i(k_x), \quad (\text{B.9})$$

where

$$\hat{W}_r(k_x) = \sum_{m=0}^M (2 - \delta_{m0}) \tilde{W}_r(m\Delta x) \cos(m\Delta x k_x) \quad (\text{B.10})$$

and

$$\hat{W}_i(k_x) = \sum_{m=0}^M (2 - \delta_{m0}) \tilde{W}_i(m\Delta x) \cos(m\Delta x k_x). \quad (\text{B.11})$$

APPENDIX C: SOUBARAS'S EXTRAPOLATOR

Let's start with a compactly supported operator, $\tilde{W}(x, k, \Delta z)$, that is an even complex function

$$\tilde{W}(x, k, \Delta z) = \tilde{W}_r(x, k, \Delta z) + i\tilde{W}_i(x, k, \Delta z), \quad (\text{C.1})$$

where

$$\tilde{W}_r(x, k, \Delta z) = \text{real}(\tilde{W}(x, k, \Delta z)), \quad (\text{C.2})$$

$$\tilde{W}_i(x, k, \Delta z) = \text{imag}(\tilde{W}(x, k, \Delta z)), \quad (\text{C.3})$$

and

$$k = \frac{\omega}{V}. \quad (\text{C.4})$$

x is the transverse coordinate, ω is the angular frequency, V is the constant velocity, and Δz is the depth step. Also, \tilde{W}_r and \tilde{W}_i are compactly supported real even functions. Then, the coefficients of $\tilde{W}_r(x, k, \Delta z)$ and $\tilde{W}_i(x, k, \Delta z)$, in Soubaras (1996) method, can be found separately and iteratively using the Remez exchange algorithm, so that the Alternation theorem is satisfied, which states that the function $\tilde{W}_r(x, k, \Delta z)$ and $\tilde{W}_i(x, k, \Delta z)$ are minimax approximations of the real and imaginary parts of exact spectrum, $\hat{W}_r(k_x, k, \Delta z)$ and $\hat{W}_i(k_x, k, \Delta z)$, with weight function $\Upsilon(k_x)$ if and only if there exist $M + 2$ wavenumbers in K such that

$$E_r(k_{x_1}) = -E_r(k_{x_2}) = E_r(k_{x_3}) = -E_r(k_{x_4}) = \dots \quad (\text{C.5})$$

and

$$E_i(k_{x_1}) = -E_i(k_{x_2}) = E_i(k_{x_3}) = -E_i(k_{x_4}) = \dots, \quad (\text{C.6})$$

where

$$\max |E_r(k_x)| = |E_r(k_{x_m})| \quad \text{for } m = 0, 1, 2, \dots, M + 2, \quad (\text{C.7})$$

and

$$\max |E_i(k_x)| = |E_i(k_{x_m})| \quad \text{for } m = 0, 1, 2, \dots, M + 2, \quad (\text{C.8})$$

where K is the union of all bands of interest and $M = (N - 1) / 2$. N is the number of complex coefficients of \tilde{W} .

The steps of finding the coefficients of $\tilde{W}_r(x, k, \Delta z)$, for example, can be summarized as follows:

1. Given a set of trial extrema $k_{x_1}, k_{x_2}, k_{x_2}, \dots, k_{x_{M+2}}$, find the $M + 2$ quantities

$\{\tilde{W}_r(n\Delta x, k, \Delta z)\}$ and ρ by solving

$$Y(k_{x_m}) \left(\hat{W}_r(k_{x_m}, k, \Delta z) - \sum_{m=0}^M (2 - \delta_{m0}) \tilde{W}_r(m\Delta x, k, \Delta z) \cos(k_{x_m} m\Delta x) \right) = (-1)^m \rho \quad (\text{C.9})$$

for $m = 0, 1, 2, \dots, M + 2$

which gives a system of $M + 2$ linear equations, where

$$\delta_{m0} = \begin{cases} 1; & m = 0 \\ 0; & m \neq 0 \end{cases}. \quad (\text{C.10})$$

2. Given $\{\tilde{W}_r(n\Delta x, k, \Delta z)\}$, compute the weighted error

$$E_r(k_x) = \Upsilon(k_x) \left(\hat{W}_r(k_x, k, \Delta z) - \sum_{m=0}^M (2 - \delta_{m0}) \tilde{W}_r(m\Delta x, k, \Delta z) \cos(k_x m\Delta x) \right), \quad (\text{C.11})$$

and from this identify the actual extremal wavenumbers $k_{x_1}, k_{x_2}, k_{x_2}, \dots, k_{x_{M+2}}$ at which $|E_r|$ is maximum.

3. If the new set $k_{x_1}, k_{x_2}, k_{x_2}, \dots, k_{x_{M+2}}$ differs from the trial extrema, go back to step 1. Otherwise stop.

The coefficients of $\tilde{W}_i(x, k, \Delta z)$, the minimax approximation of $\hat{W}_i(k_x, k, \Delta z)$, can be obtained in a similar way.

This is the theoretical connection between minimax and equiripple criteria. The weighted error has to alternate with equal amplitude at $M + 2$ wavenumbers. The Soubaras extrapolator can be then assembled according to

$$\tilde{W}(x, k, \Delta z) = \tilde{W}_r(x, k, \Delta z) + i\tilde{W}_i(x, k, \Delta z). \quad (\text{C.12})$$

REFERENCES

- Al-Yahya, K., 1989, Velocity analysis by iterative profile migration: *Geophysics*, **54**, 718–729.
- Bancroft, J. C., 2004, A practical understanding of pre- and poststack migrations 6th edition, *Geophysics 659 Course notes*, University of Calgary.
- Beasley, C., and W. Lynn, 1992, The zero-velocity layer: migration from irregular surfaces: *Geophysics*, **57**, 1435-1443.
- Berkhout, A. J., 1981, Wave field extrapolation techniques, *Geophysics*, **46**, 1638-1656.
- Berkhout, A. J., 1982, *Seismic migration: Imaging of acoustic energy by wavefield extrapolation*, A. Theoretical aspects, 2nd Ed.: Elsevier Science Publ. BV.
- Berkhout, A. J., 1997a, Pushing the limits of seismic imaging, part I: Prestack migration in terms of double dynamic focusing: *Geophysics*, **62**, 937–953.
- Berkhout, A. J., 1997b, Pushing the limits of seismic imaging, part II: Integration of prestack migration, velocity estimation, and AVO analysis: *Geophysics*, **62**, 954–969.
- Berkhout, A. J., 2001, Seismic imaging beyond depth migration: *Geophysics*, **66**, 1895–1912.
- Bevc, D., 1997, Flooding the topography: Wave-equation datuming of land data with rugged acquisition topography: *Geophysics*, **62**, 1558–1569.
- Biondi, B., 2004, *3D Seismic Imaging*, SEG publication.
- Bishop, T., K. Bube, R. Cutler, R. Langan, P. Love, J. Resnick, R. Shuey, D. Spindler, and H. Wyld, 1985, Tomographic determination of velocity and depth in laterally varying media: *Geophysics*, **50**, 903-923.

- Berryhill, J. R., 1979, Wave-equation datuming: *Geophysics*, **44**, 1329–1344.
- Bleistein, N., Cohen, J. K., and Stockwell, J. W. J., 2001, *Mathematics of multidimensional seismic inversion*: Springer-Verlag New York, Inc., *Interdisciplinary Applied Mathematics*, **6**.
- Bourgeois, A., M. Bourget, P. Lailly, M. Poulet, P. Ricarte, and R. Versteeg, 1991, Marmousi, model and data: in *The Marmousi experience*, EAGE, 5 - 9.
- Claerbout, J. F., 1971, Toward a unified theory of reflector imaging: *Geophysics*, **36**, 3, 467-481.
- Claerbout, J. F., 1985, *Imaging the Earth's Interior*: Blackwell Scientific Publications, Inc.
- Cox, B. E., and D. J. Verschuur, 2001, Tomographic inversion of focusing operators: 63rd Ann. Internat. Mtg., Eur. Assn. Geosci. Eng., Extended Abstracts, M-35.
- de Bruin, C.G. M., C. P. A. Wapenaar, and A. J. Berkhout, 1990, Angle dependent reflectivity by means of prestack migration: *Geophysics*, **55**, 1223–1234.
- Deregowski, S. M., 1990, Common offset migration and velocity analysis: *First Break*, **8**, 225–234.
- Docherty, P., 1991, A brief comparison of some Kirchhoff integral formulas for migration and inversion: *Geophysics*, **56**, 1164-1169.
- Etgen, J. T., 1994, Stability analysis of explicit depth extrapolation through laterally varying media: 64th Annual International Meeting, SEG, Expanded Abstracts, 1266–1269.

- Faye, J.P., and J.P. Jeannot, Prestack migration velocities from focusing depth analysis: 56th Annual International Meeting, SEG, Expanded Abstracts, 438-440.
- Fishman, L., J. McCoy, 1985, A new class of propagation models based on a factorization of the Helmholtz equation, *Geophys. J. R. Astr. Soc.*, **80**, 439–461.
- Fishman, L., 2005, Phase Space and Path Integral Methods in Seismic Wave Propagation and Imaging, Distinguished Chair Lecture Notes, PIMS, University of Calgary.
- Ferguson, R., 1999, Seismic Imaging in Heterogeneous Anisotropic Media by Nonstationary Phase Shift, PhD thesis, University of Calgary, Canada.
- Ferguson, R., G. Margrave, 2002, Prestack depth migration by symmetric nonstationary phase shift: *Geophysics*, **67**, 594–603.
- Gazdag, J., 1978, Wave equation migration with the phase shift method: *Geophysics*: **43**, 1342 – 1351.
- Gazdag, J., and P. Squazzerro, 1984, Migration of seismic data by phase shift plus interpolation, *Geophysics*, **49**, 124-131.
- Geiger, H., 2001, Relative-Amplitude-Preserving Prestack Time Migration by the Equivalent Offset Method, PhD thesis, University of Calgary.
- Gray, S. H., and W. May, 1994, Kirchhoff migration using eikonal equation traveltimes: *Geophysics*, **59**, 810-817.
- Gray, S. H., 1997, Where is the zero-velocity layer?: *Geophysics*, **62**, 266–269.
- Gray, S., 2001, Seismic Imaging: *Geophysics*, **66**, 15–17.
- Gray, S., H., J. Etgen, J. Dellinger, and D. Whitmore, 2001, Seismic migration problems and solutions, *Geophysics*, **66**, 1622–1640.

- Hale, D., 1991, Stable explicit depth extrapolation of seismic wavefields: *Geophysics*, **56**, 1770-1777.
- Holberg, O., 1988, Towards optimum one-way wave propagation, *Geophys. Prosp.*, **36**, 99-114.
- Huang, L. Y., M. C. Fehler, and R. S. Wu, 1999, Extended local Born Fourier migration method: *Geophysics*, **64**, 1524–1534.
- Kessinger, W., 1992, Extended split-step Fourier migration: 62th Annual International Meeting, SEG, Expanded Abstracts, 917–920.
- Kosloff, D., J. Sherwood, Z. Koren, E. Machet, and Y. Falkovitz, 1996, Velocity and interface determination by tomography of depth migration gathers: *Geophysics*, **61**, 1511-1523.
- Lafond, C., and A. Levander, 1993, Migration moveout analysis and depth focusing: *Geophysics*, **58**, 91-100.
- Liu, Z., and N. Bleistein, 1994, Velocity analysis by perturbation: 64th Annual International Meeting, SEG, Expanded Abstracts, 1191–1194.
- Le Rousseau, J. H., and M. V. de Hoop, 2001, Modeling and imaging with the scalar generalized-screen algorithms in isotropic media: *Geophysics*, **66**, 1551–1568.
- Lee, W. B., and L. Zhang, 1992, Residual shot profile migration: *Geophysics*, **57**, 812-822.
- MacKay, S., and R. Abma, 1992, Imaging and velocity estimation with depth-focusing analysis: *Geophysics*, **57**, 1601-1622,.
- MacKay, S., and R. Abma, 1993, Depth-focusing analysis using a wavefront-curvature criterion: *Geophysics*, **58**, 1148-1156.

- MacKay, S., 1994, Efficient wavefield extrapolation to irregular surfaces using finite differences: zero-velocity datuming: 64th Annual International Meeting, SEG, Expanded Abstracts, 1564–1567.
- Margrave, G. F., 1998, Direct Fourier migration for vertical velocity variations: CREWES Research Report, **10**.
- Margrave, G. F., and R. J. Ferguson, 1999, Wavefield extrapolation by nonstationary phase shift: *Geophysics*, **64**, 1067-1078.
- Margrave, G. F., and Z. Yao, 2000, Downward continuation from topography with a laterally variable depth step, 70th Annual International Meeting, SEG, Expanded Abstracts, 481-484.
- Margrave, G., F. Lamoureux, P. Gibson, R. Bale, and J. Grossman, 2002, Exact wavefield extrapolation in 2D for $v(x)$: CREWES Research Report, **14**.
- Margrave, G. F., 2003, Methods of Seismic Data Processing, Geophysics 657 Course lecture notes, University of Calgary.
- Margrave, G. F., H. D. Geiger, S. M. Al-Saleh, and M. P. Lamoureux, 2006, Improving explicit depth migration with a stabilizing Wiener filter and spatial resampling: *Geophysics*, **71**, 111-120.
- McClellan, J. H., and T. W. Parks, 1972, Equiripple approximation of fan filters: *Geophysics*, **37**, S73-583.
- Parks, T.W., and C. S. Burrus, 1987, Digital Filter Design, John Wiley & Sons, 54-83.
- Ren, J., C. Gerrard, J. McClean, M. Orlovich, and A. Long, 2005, An efficient 3D explicit finite-difference prestack depth migration: *CSEG Recorder*, 44-46.

- Ristow, D., and T. Rühl, 1994, Fourier finite-difference migration: *Geophysics*, **59**, 12, 1882–1893.
- Schneider, W. A., 1978, Integral formulation for migration in two and three dimensions: *Geophysics*, **43**, 49-76.
- Selesnick, I.W., M. Lang, and C. S. Burrus, 1996, Constrained Least Squares Design of FIR Filters with Specified Transition Bands, *IEEE*, **44**, 1879-1892.
- Soubaras, R., 1996, Explicit 3-D migration using equiripple polynomial expansion and Laplacian synthesis, *Geophysics*, **61**, 1386-1393.
- Stoffa, P. L., J. T. Fokkema, R. M. de Luna Freire, and W. P. Kessinger, 1990, Split-step Fourier migration: *Geophysics*, **55**, 410-421.
- Stolk, C., and W. Symes, 2004, Kinematic artifacts in prestack depth migration: *Geophysics*, **69**, 562–575.
- Stork, C., 1992, Reflection tomography in the post migrated domain: *Geophysics*, **57**, 680-692.
- Tarantola, A., 1984, Inversion of seismic reflection data in the acoustic approximation: *Geophysics*, **49**, 1259-1266.
- Thorbecke, J. W., and Rietveld, W. E. A., 1994, Optimum extrapolation operators—A comparison: 56th Annual International Meeting, EAEG, Extended Abstracts, 105.
- Thorbecke, J.W., 1997, Common Focus Point Technology: Ph.D. thesis, Delft University of Technology.
- Thorbecke, J., K. Wapenaar, and G. Swinnen, 2004, Design of one-way wavefield extrapolation operators, using smooth functions in WLSQ optimization, *Geophysics*, **69**, 1037-1045.

- Valenciano, A., and B. Biondi, 2003, 2-D deconvolution imaging condition for shot-profile migration, 73rd Annual International Meeting, SEG, Expanded Abstracts, 1059-1062.
- Varela, C. L., P. L. Stoffa, and M. K. Sen, 1998, Background velocity estimation using non-linear optimization for reflection tomography and migration misfit: *Geophys. Prosp.*, **46**, 51–78.
- Wang, B., and K. Pann, 1998, Model-based Interpretation of Focusing Panels for Depth Focusing Analysis, 68th Annual International Meeting, SEG, Expanded Abstracts, 1596-1599.
- Wang B., F. Qin, V. Dirks, P. Guillaume, F. Audebert, and D. Epili, 2005, 3D finite angle tomography based on focusing analysis, 75th Annual International Meeting, SEG, Expanded Abstracts, 2546-2549.
- Woodward, M., 1992, Wave-equation tomography: *Geophysics*, **57**, 15-26.
- Yilmaz, O., and R. Chambers, 1984, Migration velocity analysis by wavefield extrapolation: *Geophysics*, **49**, 1664–1674.
- Yilmaz, O., *Seismic Data Processing*, 1987, Society of Exploration Geophysicists.
- Zhu, J., L. Lines, and S. Gray, 1998, Smiles and frowns in migration/velocity analysis: *Geophysics*, **63**, 1200-1209.